Synthesis, analysis and processing of novel materials in the Y_2O_3-Al_2O_3 system

by

Julien Claudius Marchal

A dissertation submitted in partial fulfillment
of the requirements for the degree of
Doctor of Philosophy
(Materials Science and Engineering)
in The University of Michigan
2008

Doctoral Committee:

Professor Richard M. Laine, Chair
Professor Stephen C. Rand
Professor John W. Halloran
Professor Frank E. Filisko

Dedicated to my family and all the friends that helped me through this.

ACKNOWLEDGMENTS

First I must thank the (too numerous to list) funding sources that have allowed me to pursue this degree. I would like to thank Richard Laine for his patience and guidance during my graduate studies. My committee members; John Halloran, Xiaoqing Pan, and Stephen Rand deserve special thanks for taking on the task of serving for this thesis committee.

I could not have done this work without the support of my family, friends and fellow graduate students. In particular I would like to thanks the members of the fafnir team that worked with me on these experiments, Min Kim and Jose Azurdia. I would like to also thank Nancy Polashak who worked hard to ensure we had the materials we needed.

TABLE OF CONTENTS

CHAPTER 1

CHAPTER 2

CHAPTER 3

CHAPTER 4

CHAPTER 5

CHAPTER 6

LIST OF TABLES

LIST OF FIGURES

ABSTRACT

In the current work, liquid feed flame spray pyrolysis (LF-FSP) was used to create three novel nanopowders in the Y_2O_3-Al_2O_3 system: α-Al_2O_3, YAG (garnet $Y_3Al_5O_{12}$) and hexagonal $Y_3Al_5O_{12}$.

For example, LF-FSP combustion of metalloorganic yttrium and aluminum precursors in a 3/5 ratio forms hexagonal $Y_3Al_5O_{12}$, a newly discovered crystalline phase detailed in this work. The resulting 15-35 nm average particle size, single crystal nanopowders were characterized by TGA-DTA, XRD, HR-TEM, electron diffraction and FTIR. The data was used to establish a model for the crystal structure of this new phase (hexagonal, with crystal parameter of $a = 0.736$ nm, $c = 1.052$) consisting of a superlattice of substituted hexagonal $YAlO_3$.

YAG has been extensively investigated for its applications as scintillators, phosphors and as a laser host. Fully dispersible, unaggregated single crystal YAG nanopowders with average particle sizes of 35-50 nm were obtained from hexagonal $Y_3Al_5O_{12}$ after annealing at 850°C-1200°C (for 2h-8d). The resulting YAG nanopowder was processed into green bodies using cold isostatic pressing after adding binders. $99\%^+$ dense monoliths were obtained after sintering at 1400°C in vacuum (6-8 h), while maintaining grain sizes < 500 nm. The ability to sinter while keeping sub-micron grains differs from present techniques (where translucency is obtained through exaggerated grain growth to 5-10 microns) reported in the literature for sintering polycrystalline YAG. and is the first step for improving polycrystalline YAG laser host optical properties.

LF-FSP processing of transition Al_2O_3 nanopowders converts them to single crystal α-Al_2O_3 nanopowders, previously thought impossible to obtain. The α-Al_2O_3

nanopowders thus obtained, consist of unaggregated 30-40 nm single particles These nanopowders were characterized by XRD, HR-TEM, SEM, DLS, FTIR. Green bodies of α-Al_2O_3 nanopowders were sintered to 99% density without sintering aids at 1400°C (6-8 h). After HIPing at 1400°C and 138 MPa, the pellets exhibited some transparency. LF-FSP thus allows synthesis of large quantities of previously unavailable α-Al_2O_3 nanopowders necessary for developing nanograined α-Al_2O_3 ceramic monoliths for transparent armors, polycrystalline laser hosts and prosthetic implants. Most importantly, it demonstrates the use of LF-FSP to modify the crystalline phase of nanopowders, without causing aggregation.

Chapter 1: Introduction

The fields of ceramic science and engineering are too vast to define easily as a whole. New ceramic materials both natural and man-made are synthesized, engineered or discovered, each year for numerous applications. These materials encompass ceramics used for cookware, whiteware or construction materials, as well as for advanced applications such as super conducting ceramics, transparent conductors or laser hosts among others.

A better understanding of chemical composition, micro-structure as well as processing methods will always allow one to tailor ceramics for a wider range of properties. For example tailoring of indium tin oxide ($Sn:In_2O_3$, transparent conductor),[1] barium iron oxide ($BaFe_{12}O_{19}$, hard magnets),[2] boron carbide (B_4C, radiation shielding),[3] α-alumina (Al_2O_3, translucent envelope, structural prostheses),[4-6] silicon nitride (Si_3N_4, cutting tools),[7] mullite ($Al_6Si_2O_{13}$ thermal insulation),[8] zinc oxide (ZnO, gas sensors),[9] has led to better properties for applications with more demanding performance requirements.[10-11]

Ceramics used primarily for electrical and electronics purposes are also varied in composition and versatile in applications. Historically, ceramics were used as insulators but now encompass the whole range of properties from insulators to semi-conductors to conducting ceramics,[12] to low and high k dielectrics,[13-14] piezoelectrics,[15] ferroelectrics and superconductors.[16-17] The design and properties optimization of these advanced ceramics requires control over their chemical and phase composition, microstructure and processing conditions. For electronic, structural and photonic applications, control mandates starting with highly homogeneous powders and sub-micron particle sizes.

In the following, we first discuss the development of nano-grained ceramics and their potential for better mechanical and photonic properties. We then detail liquid-feed flame spray pyrolysis (LF-FSP) as a means of synthesizing the oxide nanopowders needed for manufacturing nano-grained ceramics. Finally we use the Y_2O_3-Al_2O_3 system to demonstrate how LF-FSP can be used to solve the difficulties inherent to synthesizing and processing nanopowders. Chapter 2 describes the general experimental methods. Thereafter Chapters 3 to 5 discuss the formation of YAG composition nanopowders by LF-FSP, the identification of a new $Y_3Al_5O_{12}$ crystalline phase and its sintering behavior, and finish with the conversion of transition aluminas into $\alpha-Al_2O_3$ nanopowder, as well as its sintering properties.

1.1 Nano-grained ceramics

Grain size control in dense ceramic monoliths has been investigated extensively as a means to tailor properties.[19-20] The resulting development of sub-micron grain size ceramic monoliths has paved the way for theoretical prediction of the properties of nano-grained dense ceramic monoliths.[21] In this section, we focus on pore formation and evolution and the influence of grain size. Coincidentally small grain sizes improve their in-line transmission of light (potential for optical/photonic applications). We then discuss the difficulties generally encountered in synthesizing and processing ceramic nanopowders with the requisite characteristics to sinter into fully dense, nano-grained monoliths.

1.1.1 Pore formation and evolution

Sub-micron grained polycrystalline ceramics have been investigated extensively for structural applications,[22-28] including their use in prosthetics, bone implants, ceramic blades or armor due to their high hardness and high toughness.[22-27] Lack of control, during processing of ceramic powders into green bodies or during sintering of these green bodies to polycrystalline ceramics monoliths, results in defects that severely decrease their hardness and toughness.[21] In particular, understanding pore formation and evolution is essential to designing high toughness and/or transparent polycrystalline ceramics.

Several kinds of pores occur during the processing of ceramic powders into the initial green bodies.[29-32] First (comprising most of the initial pore volume) are the interstitial spaces between particles resulting from packing. Interstitial pore sizes range from 20 to 50% of the particle sizes in the case of perfect packing of spherical particles and are larger when packing defects are present.[29]

Additional porosity is introduced by aggregation of particles in the powders forming the green body. These aggregates generally form porous fractal shapes that also pack unevenly in the green bodies. These pores are either inside the fractal aggregates or interstitials between aggregates and in both case are significantly larger than the average particle size.[30]

Several kinds of pores are also specific to the processing techniques used to form the green bodies. Uniaxial pressing results in density gradients leading to inhomogeneous distribution of type and amount of porosity in a green body.[31] The use of slurries can result in air bubbles up to 0.5 mm in size.[32]

Sintering green bodies to final dense polycrystalline monolith occurs in three stages[33]

(1) *Initial stage.* Particles merge forming necks at inter-particle contacts.

(2) *Intermediate stage.* Continuous pore networks form as most of the densification occurs. The surface energy of small particles is higher than that of larger ones, resulting in the disappearance of the finest grains and growth of larger grains.[34] This generally results in homogenization of grain sizes

(3) *Final stage.* Pore networks close followed by pore diffusion.

During each of these three stages, the different pores discussed above evolve as new kinds of porosity emerge. A full nomenclature of porosity changes is beyond the scope of this study, but the most relevant examples are discussed below.

Differences in local sintering rate result in uneven densification. There are several reasons for this phenomenon. Diffusion rates during the first two stages of sintering can be affected by density gradients resulting from initial processing. An uneven distribution of dopants within green bodies can also change diffusion rates locally.[35] Secondary phases might also alter the local sintering mechanisms involved.[35] Also, aggregates with already formed necks between particles have higher local sintering rates than their unaggregated surrounding.[36,37] These differences in local sintering rates lead to uneven densification, resulting in pores forming at the interface between zones with high and low sintering rates.

The driving forces for all pores removal depend on the ratio of pore size to particle size, causing all pores above a critical size d_c to initially grow as the smaller pores disappear or coalesce)[34, 38, 39] Equation (1) details the dependence of this critical pore size on the coordination number of the pore described as the number of grains in contact with the pore (n=1 for intra-granular pores, 2 for pores located at the grain boundary between two grains…) as well as the surface and interface tension: pores with lower coordination numbers can have slightly larger size and still disappear

$$d_c = D \times \frac{(\frac{\pi}{n_s})^{1/2}}{\sin(\frac{\pi}{n_s})^{1/2}} \times \left(\frac{2\gamma_s}{\gamma_i} - 1 \right) \qquad (1)$$

D is the average grain size, d_c is the critical pore size. n_s is the coordination number of the pore (number of grains in contact with pore). γ_i and γ_s are the interface and surface tension at the surface of the pore.

The coordination number of a pore is dependant on the packing of the particles in the green body and in particularly dependent on the kind of defect causing the pore. Average pore sizes in the various stages of sintering will thus be vastly different than those of the pores initially present in the green bodies.

Initial porosity, as well as the evolution of porosity during the first two steps of sintering, determines most of the residual porosity in the polycrystalline monoliths after the third stage of sintering. Control of this residual porosity is essential to optimizing mechanical properties and requires rigid control of the initial green body porosity and of the pore evolution during sintering. Control of pore evolution can be achieved by controlling the sintering rates and mechanisms during each of the sintering stages. Both are heavily influenced by the grain size, whose growth can be limited during sintering.

Recent experiments show that densification can occur with limited grain growth.[40,41,21] Dense polycrystalline monolith can therefore be obtained while controlling the grain size (and size distribution) resulting in better control of the porosity. This control requires smaller initial particles.[21]

Controlling grain sizes thus offers the potential to control the residual porosity as described above. Decreasing grain size can also increase the in-line transmission of polycrystalline ceramics by reducing the effects of grain boundaries on refraction and light scattering as discussed below.

1.1.2 Optical properties and optical/photonic applications

In photonic applications, one encounters single crystal or glass lasers most commonly. For example, Yttrium aluminum garnet (Nd:$Y_3Al_5O_{12}$) is one of the most widely used laser materials in medicine for surgery as well as for industrial cutting,[42-43] exemplifying traditional single crystal solid-state lasers.[44] However, recent studies have shown that polycrystalline Nd:$Y_3Al_5O_{12}$ transparent ceramic lasers can be made that offer properties superior to single crystal lasers. In particular they offer higher concentrations and controllable distributions of dopants, as well as better performance in ultra-short pulse mode.[45-46] Other potential applications for transparent polycrystalline ceramics include radomes and transparent armor.[47-48]

Reducing grain size in translucent ceramics potentially offers benefits in regards to their photonic properties. Current translucent ceramics, commonly used for high pressure metal vapor lamp envelopes, generally have 10-20 μm average grain sizes to minimize interactions between light and the grains or residual pores (the effect of grain boundary reflection in particular decrease with extraordinary grain growth).[49] This increases their sensitivity to fatigue (due to anisotropy of α-Al_2O_3 coefficient of thermal expansion).

Several photonic properties also depend on grain size, in-line transmission of light being the main example.[50] In ceramics, light transmission can be hindered by birefringence, light scattering caused by residual porosity, grain boundary refraction and reflection.[51] Grain boundary refraction is caused by anisotropy of the refractive index in non-cubic crystal structures, (different crystallographic orientations have different refractive indexes), resulting in index mismatches at grain boundaries.[52] The resulting loss of in-line transmission depends on grain sizes, as well as the maximum refractive index mismatch as described in Equation (2). The in-line transmission gets closer to single crystal light transmission when the average grain size decreases, but decreases when the average grain size increases.[51]

$$Transmission = (1-R)e^{-\frac{3\pi^2 t\Delta n^2 d}{\lambda^2}} \qquad (2)$$

R is the reflectance of the material, t is the sample thickness, Δn the maximum mismatch in refractive index between the crystallographic directions, d the average grain size, λ is the wavelength of light transmitted.

Residual porosity and secondary phases in the ceramic also limit in-line transmission by scattering light. Equation (3) describes the general influence of defects on the in-line transmission as a function of the defect size. The in-line transmission decreases as the average defect size increases. The size of most of these defects, resulting from residual porosity, is on the order of the average grain size as discussed above.

$$Transmission = (1-R)e^{\left(-\frac{3\pi\times t(2\sum k_{defect}\cdot d_{defect}\Delta n_{defect}^{2})}{\lambda^{2}}\right)} \qquad (3)$$

R is the reflectance of the material, t is the sample thickness, k_{defect} a form factor of the defect, Δn_{defect} the difference in refractive index between the material (average index) and the defect considered (pores or secondary phases), d_{defect} the average defect size, λ is the wavelength of light transmitted.

Development of transparent ceramics with higher in-line transmission (closer to theory), and structural ceramics with higher mechanical properties could thus be achieved by sintering to full density while limiting grain and pore growth.

1.1.3 Difficulties in synthesizing nano-grained ceramics.

Nano-grained ceramics thus present considerable potential for improved photonic properties, according to equations (2)-(3). Two technological difficulties hinder the processing of nano-grained ceramics (optimally with average grain size < 200 nm). First, as explained above, large quantities of high purity, unaggregated, sub 100 nm powders with uniform dispersity are essential for controlling final grain size in nano-grained ceramics. There are many methods of synthesizing metal oxide nanopowders, from classical methods such as gas-feed combustion of metal chlorides[53] and chemical precipitation techniques[54,55] to thermal decomposition of metal alkoxides.[56] Each of these techniques has been reviewed in detail in the litterature.[57,58] They do not produce the required quality and/or quantity of nanopowders, mostly due to high degrees of aggregation in the resulting nanopowders. Mixed-metal oxide nanopowders are even more difficult to obtain with most of these techniques further limiting development of doped or mixed-metal oxide nano-grained ceramics.

The second difficulty in developing nano-grained ceramics is in their processing to green bodies.[59] Van der Waals interactions between nanoparticles increase greatly because of their high surface to volume ratios, increasing the viscosities of nanopowder slurries compared to slurries of micron-sized powders of the same material. Furthermore, differences in surface chemistry between micron and nanoparticles of the same composition can also result in difficulties in wet-processing of these nanopowders.

This thesis discusses liquid-feed flame spray pyrolysis (LF-FSP) as a means to produce large quantities of high purity, unaggregated, single or mixed-metal oxide nanopowders with uniform dispersity. It will also discuss LF-FSP for phase conversion in nanopowders, processing of these nanopowders into green compacts, and the process of sintering to fully dense polycrystalline monoliths.

1.2 Liquid-Feed Flame Spray pyrolysis.

Liquid-feed flame spray pyrolysis has emerged as a promising technique for producing both single and mixed-metal oxide nanopowders with the required properties for processing nano-grained ceramics: (1) nanoparticles in the 10-50 nm range; (2) complete control over purity and stoichiometry; (3) narrow particle size distributions and; (4) limited aggregation.[34,60]

In LF-FSP processing, detailed in Chapter 2, the fuel/chemical precursor is transformed in an oxygen-rich aerosol by a Bernoulli mist nozzle and ignited using pilot torches. Despite the fact that the LF-FSP flame temperatures range from 1500° to 2000°C, the choice of precursor seems to make a considerable difference in the quality of the powder produced both in terms of phase and particle morphology as discussed in Chapter 3.[61,62] Differences in nanopowder morphologies can be explained by combustion/decomposition mechanisms that occur at the beginning of the combustion process as briefly discussed below.

In LF-FSP, the initial spray generally consists of a solution of metal propionates and/or acetylacetonates in ethanol (0.5-5 wt% ceramic loading). This precursor is mixed with oxygen in a Bernoulli mist nozzle and ignited using pilot torches The resulting micron-sized droplets in the aerosol start to vaporize and ignite on their exterior surface until boiling occurs inside the droplet, causing it to fragment.[63] These fragmented droplets themselves vaporize and ignite, possibly undergoing further fragmentation. Combustion of the metalloorganic precursor in the droplets forms oxo or hydroxyl species. Organic ligands are expected to combust simultaneously with the fuel, resulting in high flame temperatures. The resulting oxo or hydroxyl product species condense in the gas phase forming nanoparticles that grow until they are quickly quenched. This rapid quenching limits their sizes.

Combustion mechanisms are quite different for metal nitrate precursors. Particle formation starts before the fragmentation of the droplets described above. The nitrates partially decompose and/or the particles form melted droplets,[61,63,64] resulting in the formation of networked particles that act as seeds for the formation of micron-sized particles in the gas phase as hypothesized from the work of Zacharia[63] and Madler,[64] as well as earlier studies in our group.[61] This also causes a bimodal distribution of particle sizes as not all the nitrate molecules decompose at the same time. Smaller particles could thus be the result of melting/decomposition occurring after droplet fragmentation. The exact mechanism by which this residual metal nitrate results in some smaller nanoparticles as seen in Chapter 3 is as yet not fully understood. Changes in the flame temperature, as well as dwell time, also result in changes in both the morphology, average particle size, particle size distribution and crystalline phase of the nanopowder formed as will be discussed in Chapters 3 and 4.

Thus even though widely available and relatively inexpensive, metal nitrates are of limited use for LF-FSP. Development of new metalloorganic precursors for LF-FSP can provide high metal purity (six nines) nanopowders with the required properties for processing nanograined ceramics. There are also several benefits to developing metalloorganic precursors for LF-FSP. First they can be purified to metal purities exceeding six nines. In addition, through sufficient development, compatible chemistries can be found to produce mutually soluble precursors containing several metal species, in turn allowing for production of homogeneous mixed-metal oxide ceramic nanopowders.[65-69] Additional impurities found in LF-FSP powders derived from metalloorganic precursor includes carbonates and hydroxyl groups (generally 1-5 wt%).

Particles produced in the flame are rapidly quenched as described in Chapter 2, resulting in nanoparticles with limited interparticle contacts at high temperature as described below, inhibiting aggregation in the final nanopowders. This inhibition of aggregation inspired a further development of the LF-FSP technique called suspension-feed flame spray pyrolysis (SF-FSP), in which the precursors consist of various suspensions of nanopowder in alcohols with or without metalloorganic precursors. An aerosol is then formed and ignited using techniques similar to LF-FSP. As the droplets ignite, the nanoparticles in suspension are exposed to high flame temperature (1200-2200°C) for a brief instant and quenched extremely fast to 300-500°C. This brief exposure to the flame does not permit aggregation, due to the combination of the high flow rates and rapid quenching, but is enough to cause phase changes. For the same reasons, particle growth is limited during the process with the resulting nanopowders having relatively similar sizes to the nanopowders used as precursor. Chapter 5 describes the use of SF-FSP to produce nano α-Al_2O_3 as well as the influence of the initial nanopowders in the precursor suspension.

The use of metalloorganic precursors with dispersed nanopowders in SF-FSP results in oxo or hydroxyl species produced by combustion of the metalloorganic precursor condensing on the precursor nanopowder. With the right flame temperatures and choice of precursors, this can result in core-shell nanopowders.[68-69] These oxo or hydroxyl species can also react with the nanopowder precursor forming doped or mixed-metal nanopowder (such as in our study of neodymium or chromium propionate precursor on δ-Al_2O_3 nanopowder, discussed in the appendixes). [70]

The nanopowder phases can also differ from the stable crystalline phases expected thermodynamically, due to rapid quenching coupled with high initial temperatures in the flame. For single metal nano-oxides, this often results in kinetic phases being formed, as the dwell time at high temperatures (maximum of 0.05 sec) can be insufficient for thermodynamic phases to form. The formation of kinetic phases can also extend the composition range in a phase field for some mixed-metal nano-oxides, as our studies on spinel-type materials has shown.[67, 71]

1.3 Y_2O_3-Al_2O_3 System

These developments in the LF-FSP technique allow better control of the particle morphology and phases of the as-produced nanopowders. To demonstrate the utility of these new LF-FSP techniques, we investigated production of nanoparticles in the Y_2O_3-Al_2O_3 system. This system was chosen for two reasons: first the extensive polymorphism of all but one of the line compounds in the system is ideal for demonstrating phase control. Several phases in this system are hard to obtain as nanopowders, especially yttrium aluminum garnet, YAG ($Y_3Al_5O_{12}$) and α-Al_2O_3, as earlier work in this group showed.[61] Secondly the Y_2O_3-Al_2O_3 system has been studied extensively over the past decades due to the many varied applications of its three main compositions: Al_2O_3 (electrical insulation, transparent envelopes for metal vapor lamps, refractory, abrasive, prostheses…),[72-77] $Y_3Al_5O_{12}$ (laser hosts, scintillators, phospors, creep resistant structural materials)[78-82] and Y_2O_3 (phosphors, up-converters).[83-84]

Al_2O_3 can exist as eight main polymorphs, with α-Al_2O_3 being the thermodynamically most stable phase. The other polymorphs, called transition aluminas, are products resulting from the dehydration of the various aluminum hydroxides and convert to α-Al_2O_3 after 1-3 phase changes. Among these polymorphs, $\delta-Al_2O_3$ is also produced as nano-alumina (< 100 nm) in ton/year quantities for fluorescent light coatings, chemical mechanical polishing, transparent reinforcing fillers for polymers. These polymorphs have properties very different from α-Al_2O_3: in particular they have lower densities and a face centered cubic (FCC) arrangement of oxygen atoms in their crystal structure as opposed to the HCP arrangement in α-Al_2O_3. Rapid changes of density during conversion to α-Al_2O_3 cause the formation of a highly aggregated vermicular structure, which limit the use of transition alumina nanopowders to obtain high quality unaggregated α-Al_2O_3 nanopowders.

α-Al_2O_3 nanopowders could in theory be sintered into high strength transparent ceramic monoliths as described earlier for such applications as transparent polycrystalline armor, radome or sodium vapor lamp envelopes.[73] There are no industrial techniques to obtain $\alpha-Al_2O_3$ powders with average particle sizes below 100 nm, despite the wide availability of micron size powders.

The second composition we studied, namely $Y_3Al_5O_{12}$, has only two polymorphs, yttrium aluminum garnet (YAG) and yttroalumnite. Both have a complex cubic crystal structure with yttroalumnite being the high temperature, distorted structure of YAG, as described in Chapter 4. YAG materials have been studied extensively over many decades because of their exceptional high temperature mechanical strength coupled with low creep and their photonic properties.[80-82] The recent development of polycrystalline doped YAG monoliths allows easy access to laser hosts having properties comparable to single YAG crystal.[45-46]

Several methods produce $Y_3Al_5O_{12}$ composition nanopowders,[54,55] but they result in precursor nanopowders that require annealing at 1000-1400°C to form YAG. Uniform YAG formation is also difficult due to the formation of secondary phases in YAG composition material caused by minor variations in the yttrium/aluminum stoichiometry between particles: $\alpha-Al_2O_3$, three $YAlO_3$ polymorphs (hexagonal, orthorhombic and cubic) or $Y_4Al_2O_9$ can thus form in YAG powders.[56] The $YAlO_3$ polymorphs are also the kinetically favored phase during the formation of YAG, especially if using gas-phase synthesis.[58] Hence, these secondary phases often reside at the grain boundaries of YAG polycrystalline ceramics, thereby reducing its optical properties.

1.4 References

[1]C.G. Granqvist, "Transparent conductors as solar energy materials: A panoramic review", *Sol. En. Mater. and Sol. Cells,* **2007** 91 (17) 1529.

[2]L. Affleck, M.D. Aguas, I.P. Parkin, Q.A. Pankhurst and M.V. Kuznetsov, "Microstructural aspects of the self-propagating high temperature synthesis of hexagonal barium ferrites in an external magnetic field", *J. Mater. Chem.*, **2000** 10 (8) 1925.

[3]D. Emin, T.L. Aselage, "A proposed boron-carbide-based solid-state neutron detector", *J. Appl. Phys.* **2005** 97 (1) 013529.

[4]V. Saikko, J. Keränen, "Wear simulation of alumina-on-alumina prosthetic hip joints using a multidirectional motion pin-on-disk device", *J. Am. Ceram. Soc.*, **2002** 85 2785.

[5]J. D'Antonio, W. Capello, M. Manley, B. Bierbaum, "New experience with alumina-on-alumina ceramic bearings for total hip arthroplasty", *J. Arthroplasty*, **2002** 17 390.

[6]A. Krell, P. Blank, H. Ma, T. Hutzler, M. Nebelung, "Processing of high-density submicrometer Al_2O_3 for new applications", *J. Am. Ceram. Soc.*, **2003** 86 12.

[7]X.Y. Wang, S Luao, D. Liu, X. Zhu, "Study on mechanical properties of hot-press sintering silicon nitride ceramics", *Rare Met. Mater. and Eng.*, **2007** 36 302.

[8]D.N. Boccaccini,, C. Leonelli, I. Dlouhy, P. Veronesi, "Thermal shock behaviour of mullite-cordierite refractory materials", *Adv. in Appl. Ceram..* **2007** 106 142.

[9] T. Wagner, T. Waitz, J. Roggenbuck, M. Fröba, C.D. Kohl, M. Tiemann "Ordered mesoporous ZnO for gas sensing", *Thin Sol. Films,* **2007** 515 (23) 8360.

[10]R.S. Lima, B.R. Marple," Thermal spray coatings engineered from nanostructured ceramic agglomerated powders for structural, thermal barrier and biomedical applications: A review", *J. Therm. Spray Tech.*, **2007** 16 (1) 40.

[11]A. Mukhopadhyay, B. Basu," Pressureless sintering of ZrO2-ZrB2 composites: Microstructure and properties", *Int. Mater. Rev.,* **2007** 52 (5) 257.

[12]X.L. Zhou, M Zhu, F Deng, G Meng, X Liu "Electrical properties, sintering and thermal expansion behavior of composite ceramic interconnecting materials, $La_{0.7}Ca_{0.3}CrO_{3-\delta}/Y_{0.2}Ce_{0.8}O_{1.9}$ for SOFCs", *Acta Materiala,* **2007** 55 (6) 2113.

[13]R.A. Farrell, K. Cherkaoui, N. Petkov, H. Amenitsch, J.D. Holmes, P.K. Hurley, M.A. Morris, "Physical and electrical properties of low dielectric constant self-assembled

mesoporous silica thin films", *Microelectronics Reliability,* **2007** 47 (4-5) 759.

[14]N. Umezawa, K. Shiraishi, S. Sugino, A. Tachibana, "Suppression of oxygen vacancy formation in Hf-based high-*k* dielectrics by lanthanum incorporation", *Appl. Phys. Let.*, **2007** 91 (13) 132904.

[15]P. Zubko, G. Catalan, A. Buckley, P.R.L. Welche, J.F. Scott, "Strain-gradient-induced polarization in $SrTiO_3$ single crystals", *Phys.Rev. Let.*, **2007** 99 (16) 167601.

[16]K.A. Rabe, M. Dawber, C. Lichtensteiger, C.H. Ahn, J. M. Triscone, "Modern physics of ferroelectrics: Essential background", *Phys. Ferroelectrics*, **2007** 105 1.

[17]G. Aldica, P. Badica, J.R. Groza, "Field-assisted-sintering of MgB_2 superconductor doped with SiC and B_4C", *J. Opt and Adv Mater.,* **2007** 9 (6) 1742.

[18]G.Y. Akimov, G.A. Marinin, E.V. Chaika, V.N. Varyukhin, "Effect of the grain size on the formation of a nanophase structure and tribological properties of the friction surface of a ceramic made of partly stabilized zirconia", *Tech. Phys*., **2007** 52 (10) 1362.

[19]W. Jo, T.H. Kim, D.Y. Kim, "Effects of grain size on the dielectric properties of $Pb(Mg_{1/3}Nb_{2/3})O_3$-30 mol % $PbTiO_3$ ceramics", *J. Appl. Phys.*, **2007** 102 (7) 074116.

[20]R.W. Rice, "Grain size and porosity dependence of ceramic fracture energy and toughness at 22°C", *J. Mater. Sci*., **1996** 31 (8) 1969.

[21] P. Bowen, C. Carry, "From powders to sintered pieces: forming, transformations and sintering of nanostructured ceramic oxides", *Powder. Tech.*, **2002** 128 (2-3) 248.

[22]W.A. Yarbrough, R. Roy, "Microstructural evolution in sintering of ALOOH gels", *J. Mater. Res.*, **1987** 2 (4) 494.

[23]J.P. Parimal, G. Gilde, P. Dehmer, J. McCauley, "Fracture properties and behavior of transparent ceramics", *SPIE Proc.*, **2000** 4102 15.

[24]G. Fischman, "Validated Microstructural Assessment of Femoral Heads", *J. ASTM Int.*, **2004** 1 1.

[25]V. Saikko, J. Keränen, "Wear simulation of alumina-on-alumina prosthetic hip joints using a multidirectional motion pin-on-disk device", *J. Am. Ceram. Soc.*, **2002** 85 2785.

[26]S. Eliot, "Silicon carbide ceramic armor", *Adv. Mater. Proc.*, **2007** 165 (10) 29.

[27]K.E. Kuehn, "Developments in ceramic armor patenting", *Am. Ceram. Soc. Bul.*, **2006** 85 (3) 29.

[28] J. Zhou, Y. Li, R. Zhu, Z. Zhang, "The grain size and porosity dependent elastic

moduli and yield strength of nanocrystalline ceramics", *Mater. Sci. and Eng*., **2007** 445 717.

[29]N. Chantaramee, S. Tanaka, "The effect of packing structure of powder particles on warping during sintering", *J. Eur. Ceram*. Soc., **2008** 28 (1) 21.

[30]M. Kitayama, J. Pask , "Formation and Control of Agglomerates in Alumina Powder", *J. Am.Ceram. Soc*., **1996** 79 (8) 2003.

[31]T.J. Vogler, M.Y. Lee, D.E. Grady, "Static and dynamic compaction of ceramic powders", *Int. J. Sol. and Structures,* **2007** 44 (2) 636.

[32]S.W. Sofie, F. Dogan, "Freeze Casting of Aqueous Alumina Slurries with Glycerol", *J. Am. Ceram. Soc.,* **2001** 7 1459.

[33]R.L. Coble, "Sintering Crystalline Solids. I. Intermediate and Final State Diffusion Models", *J. Appl. Phys.,* **1961** 32 (5) 787.

[34]J.L. Shi, "Solid state sintering of ceramics: pore microstructure models, densification equations and applications", *J. Mater. Sci*., **1999** 34 (15) 3801.

[35]W.C. Johnson, R.L. Coble, "A Test of the Second-Phase and Impurity-Segregation Models for MgO-Enhanced Densification of Sintered Alumina", *J. Am. Cer. Soc.,* **1978** 61 (3-4) 110.

[36]J.L. Shi, X. Lint, S. Yen, "Effect of agglomerates in ZrO_2 powder compacts on microstructural development", *J. Mater. Sci.,* **1993** 28 (2) 342.

[37]M.A. Spears, A.G. Evans, "Microstructure Development during Final Intermediate Stage Sintering", *Acta Materiala,* **1982** 65 (10) 498.

[38]F.F. Lange, "Sinterability of Agglomerated Powders" J. *Am. Ceram. Soc*., **1984** 67(1) 83.

[39]W.D. Kingery, M. Berg, "Study of the initial stages of sintering solids by viscous flow, evaporation-condensation, and self-diffusion" *J. Appl. Phys*., **1955** 26 (10) 1205.

[40]R. Chaim, "Superfast densification of nanocrystalline oxide powders by spark plasma sintering"*J. Mater Sci*., **2006** 41 (23) 7862.

[41]M.B. Park, N.H. Cho, C.D. Kim, S.K. Lee, "Phase Transition and Physical Characteristics of Nanograined $BaTiO_3$ Ceramics .Synthesized from Surface-Coated Nanopowders", *J. Am. Ceram. Soc*., **2004** 87 (3) 510.

[42]B. Gaspirc, U. Skaleric, “Clinical evaluation of periodontal surgical treatment with an Er : YAG laser: 5-year results“, *J. Periodontology*, **2007** 78 (10) 1864.

[43]F. Quintero, J. Pou, F. Lusquiños, A. Riveiro, M. Pérez-Amo, “Single-pass and multi-pass laser cutting of Si-SiC: Assessment of the cut quality and microstructure in the heat affected zone” *J. Las. Appl*., **2007** 19 (3) 170.

[44]A.L. Schawlow, C.H. Townes, “Infrared and optical masers”, *Phys. Rev.,* **1958** 112 1940.

[45]J. Lu, M. Prabhu, J. Song, C. Li, J. Xu, K. Ueda, H. Yagi**,** “Highly efficient Nd : $Y_3Al_5O_{12}$ ceramic laser”, *Jpn. J. Appl. Phys.* **2001** 40 552.

[46]A. Ikesue, T. Kinoshita, K. Kamata, K. Yoshida, “Fabrication and Optical Properties of High-Performance Polycrystalline Nd:YAG Ceramics for Solid-State Lasers”, *J. Am. Ceram. Soc*., **1995** 78 (4) 1033.

[47]J.P. Parimal, G. Gilde, P. Dehmer, J. McCauley, “Transparent ceramics for armor and EM window applications”, *SPIE Proc*., **2000** 4102 1.

[48]Z. Zalevsky, A. Rudnitsky, M. Nathan,”Nano photonic and ultra fast all-optical processing modules”, *Opt. Express*, **2005** 13 (25) 10272.

[49]O. Katsutoshi; T. Kusunoki, “The effect of ultrafine pigment color filters on cathode ray tube brightness, contrast, and color purity”, *J. Electrochem. Soc.,* **1996** 143 1063.

[50]R. Apetz, M.B.P. van Bruggen, “Transparent Alumina: A Light-Scattering Model”, *J. Am. Ceram. Soc*. **2003** 86 (3) 480.

[51]V.V. Shvartsman, A.L. Kholkin, C. Verdier, Z. Yong, D.C. Lupascu, “Investigation of fatigue mechanism in ferroelectric ceramic via piezoresponse force microscopy”, *J. Eur. Ceram. Soc*, **2005** 25 (12) 2559.

[52]Y.C. Kang, Y.S. Chung, P.S. Bin, “Preparation of YAG:Europium Red Phosphors by Spray Pyrolysis Using a Filter-Expansion Aerosol Generator”, *J. Am. Ceram. Soc.,* **1999** 82(8) 2056.

[53]M. Nyman, J. Caruso, M.J. Hamden-Smith, T.T. Kodas, “Comparison of solid-state and spray-pyrolysis synthesis of yttrium aluminate powders ”, *J. Am. Ceram. Soc*., **1997** *80* 1231.

[54]J. Li, T. Ikegami, J. Lee, T. Mori, Y. Yajima, “Co-precipitation synthesis and sintering of yttrium aluminum garnet (YAG) powders: the effect of precipitant”, *J. Eur. Ceram.*

*So*c., **2000** *20* 2395

[55]K.T. Pillai, R.V. Kamat, V.N. Vaidya, D.D. Sood, "Synthesis of yttrium aluminium garnet by the gel entrapment technique using hexamine", *Mater. Chem. Phys.*, **1996** *46* 67.

[56]D.M. Veith, S. Mathur S, A. Kareiva, M. Jilavi, M. Zimmer, V. Huch, "Low temperature synthesis of nanocrystalline $Y_3Al_5O_{12}$ (YAG) and Ce-doped $Y_3Al_5O_{12}$ via different sol-gel methods", *J. Mater. Chem.* **1999** *9* 3069.

[57]J.R. Groza, "nanosintering", *Nanostructured Mater.* , **1999** 12 (5-8) 987.

[58]E. Pratsinis, R. Strobel, "Flame aerosol synthesis of smart nanostructured materials", *J. Mater. Chem.*, **2007** 17 (45) 4743.

[59]I.W.P. Chen, J. Chen, "Sintering of Fine Oxide Powders: I, Microstructural Evolution", *J. Am. Ceram. Soc.*, **1996** 79 (12) 3129.

[60]I.W.P. Chen, J. Chen, "Sintering of Fine Oxide Powders: II, Sintering Mechanisms", *J. Am. Ceram. Soc.*, **1997** 80 (3) 637.

[61]T. Hinklin, B. Toury, C. Gervais, F. Babonneau, J.J. Gislason, R.W. Morton, R.M. Laine "Liquid-Feed Flame Spray Pyrolytic Synthesis of Nanoalumina Powders", *Chem. Mater.*, **2004** 16 (1) 21.

[62]J. Marchal, T. John, R. Baranwal, T. Hinklin, R.M. Laine, "Yttrium aluminum garnet nanopowders produced by liquid-feed flame spray pyrolysis (LF-FSP) of metalloorganic precursors", *Chem. Mater.*, **2004** 16 (5) 822.

[63]A. Zacharia, S. Gucer, B. Izgi, H. Karaaslan, "Direct atomic absorption spectrometry determination of tin, lead, cadmium and zinc in high-purity graphite with flame furnace atomizer", *Talanta,* **2007** 72 (2) 825.

[64]M.C. Heine, L. Mädler, R. Jossen, S.E. Pratsinis, "Direct measurement of entrainment during nanoparticle synthesis in spray flames", *Combustion and Flame*, **2006** 144 (4) 809.

[65]T. Hinklin, R.M. Laine, "Synthesis of Metastable Phases in the Magnesium Spinel−Alumina System", *Chem. Mater.,* **2008** 20 (2) 553.

[66]J. Azurdia, J. Marchal, R.M. Laine, "Synthesis and Characterization of Mixed-Metal Oxide Nanopowders Along the CoO_x–Al_2O_3 Tie Line Using Liquid-Feed Flame Spray Pyrolysis", *J. Am. Ceram. Soc.,* **2006** 8 (9) 2749.

[67] J.A. Azurdia, J.C. Marchal, P. Shea, H. Sun, X.Q. Pan, R.M. Laine; "Liquid-feed flame spray pyrolysis (LF-FSP) as a method of producing mixed-metal oxide nanopowders of potential interest as catalytic materials. Nanopowders along the NiO-Al_2O_3 tie-line including $(NiO)_{0.22}(Al_2O_3)_{0.78}$, a new inverse spinel composition", *Chem. Mater.*, 2006 **18**, 731.

[68] S. Kim, M. Kim, R.M. Laine, "Combinatorial processing of mixed-metal oxide nanopowders along the ZnO-Al_2O_3 tie line using liquid-feed flame spray pyrolysis (LF-FSP)", *Chem. Mater.* **2004**, *16*, 2336.

[69] M. Kim, R.M. Laine, "Combinatorial processing of mixed-metal oxide nanopowders along the ZrO_2-Al_2O_3 tie line using liquid-feed flame spray pyrolysis (LF-FSP)", *Ceram. Pro. Res.*, *submitted.*

[70] R.M. Laine, J.M. Marchal, J. Azurdia, R. Rennensund, "Liquid Feed Flame Spray Modification of Nanoparticles", U.S. patent application 20060087062 (**2006).**

[71] R.M. Laine, J. Marchal, J. Azurdia, M, Kim, "Finding spinel in all the wrong places", *Adv. Mater, in press.*

[72] J. Crunteanu, F. Dumas-Bouchiat, C. Champeaux, A. Catherinot, P. Blondy, "Electrical conduction mechanisms of metal nanoclusters embedded in an amorphous Al_2O_3 matrix", *Thin Sol. Films*, **2007** 515 (16) 6324.

[73] T. Markus, U. Niemann, K. Hilpert "High temperature gas phase chemistry for the development of advanced ceramic discharge lamps", *J. Phys. and Chem. Sol.*, **2005** 66 (2-4) 372.

[74] J.M. Auvray, C. Gault, M. Huger, "Evolution of elastic properties and microstructural changes versus temperature in bonding phases of alumina and alumina–magnesia refractory castables", *J. Eur. Ceram. Soc.* **2007** 27 (12) 3489.

[75] P.H. Shipway, J.J. Haqq, "Wear of bulk ceramics in micro-scale abrasion - The role of abrasive shape and hardness and its relevance to testing of ceramic coatings", *Wear*, **2007** 263 (4) 887.

[76] T. Tateiwa, I.C. Clarke, G. Pezzotti, L. Sedel, T. Kumakura, "Surface micro-analyses of long-term worn retrieved "Osteal™" alumina ceramic total hip replacement", *J. Bio. Mater. Res.*, **2007** 83B (2) 562.

[77]J.Z. Sun, T. Stirner, A. Matthews, "Structure and electronic properties calculation of ultrathin alpha-Al_2O_3 films on (0001) alpha-Cr_2O_3 templates", *Sur. Sci.*, **2007** 601 (21) 5050.

[78]R.A. Yukna, R.L. Carr, G.H. Evans, "Histologic evaluation of an Nd : YAG laser-assisted new attachment procedure in humans ", *Int. J. Periondontics and Restorative Dent.* , **2007** 27 (6) 577.

[79]F. Druon, F. Balembois, P. George, "New laser crystals for the generation of ultrashort pulses", *Comptes Rendus Phys.*, **2007** 8 (2) 153.

[80]S.H. Yang, C.Y. Liu, *J. Electrochem. Soc*. "Influence of doping and coating on the photoluminescence properties of yttrium aluminum garnet phosphors", **2007** 154 (12) 397.

[81]J.X Meng, K.W. Cheah, J. Shi, P. Zhao; J.Q. Li, "Intense 1540 nm emission from Er doped Ce : YAG phosphor", *Appl. Phys. Let.*, **2007** 91 (15) 151107 .

[82]R.C. Pullar, M.D. Taylor, A.K. Battacharya, "Effect of sodium on the creep resistance of yttrium aluminium garnet (YAG) fibres", *J. Eur. Cer. Soc.* , **2006** 26 (9) 1577.

[83]S. Redmond, S.C. Rand, X.L. Ruan, M. Xaviany, "Multiple scattering and nonlinear thermal emission of Yb^{3+}, Er^{3+}: Y_2O_3 nanopowders", *J. Appl. Phys.*, **2004** 95 (8) 4069.

[84]S. Ray, A. Patra, P. Pramanik , "Photoluminescence properties of nanocrystalline Tb3+ doped Y_2O_3 phosphor prepared through a novel synthetic route", *Opt. Mater.*, **2007** 30 (4) 608.

Chapter 2: General experimental, materials and methods

2.1 Introduction

This chapter details the general laboratory techniques used in this thesis. Additional experimental descriptions are provided in the following chapters, which are more specific to work conducted in those chapters.

2.2 General materials

This section details the synthesis of the metalloorganic precursors used in LF-FSP and SF-FSP to produce the nanopowders described in this thesis. It also lists the chemical compounds used for processing the nanopowders into green bodies.

2.2.1 Materials

Anhydrous yttrium chloride (YCl_3, 99.99%), yttrium nitrate hexahydrate [$Y(NO_3)_3{\cdot}6H_2O$, 99.9%], aluminum nitrate nonahydrate [$Al(NO_3)_3{\cdot}9H_2O$,98%], methoxyacetic acid ($CH_3COCH_2CO_2H$, 98%), chromium nitrate hexahydrate [$Cr(NO_3)_3{\cdot}6H_2O$, 99.9%], neodymium nitrate hexahydrate [$Nd(NO_3)_3{\cdot}6H_2O$, 99.9%], bicine (99%), were purchased from Aldrich (Milwaukee, WI) and used as received. Anhydrous butanol (99.9%) and THF (99.9%) were also purchased from Aldrich. Yttrium tris(2-ethylhexanoate) [$Y(O_2CCHEtC_4H_9)_3$, 99.8%) and propionic acid ($C_2H_5CO_2H$, 99+%), were purchased from Alfa Aesar and used as received. Yttrium trisacetylacetonate [$Y(CH_2COCH{=}COCH_3)_3$, 99.9%] and aluminum trisacetylacetonate [$Al(CH_2COCH{=}C(O)CH_3)_3$, 99.8%] were purchased from MacKenzie (Bush, LA) and either used as received, or recrystallized by dissolving in boiling THF then cooling the solution to 2°C.

The following surfactants and additives were used for processing the nanopowders into green bodies: Tetronic 304 was received as a gift from BASF (Parsipany, NJ) and used as received. Darvan C-N was recei ed as a gift from Vanderbilt (Norwalk, CT) and used as received. Dynol 604 was received as a gift from Air Products and used as received. Duramax B-1000 was received as a gift from Rohm Haas (Philadelphia, PA) and used as received.

2.2.2 Metalloorganic precursor synthesis

2.2.2.1 Alumatrane, $N(CH_2CH_2O)_3Al$

Alumatrane was prepared by adding 1200 g (5.0 mol) aluminum tri-(*sec*-butoxide) $[C_2H_5CH(CH_3)O]_3Al$ 97% (Chattem Chemical) dropwise through an addition funnel into a 5 L mechanically stirred four-necked flask equipped with a standard distillation head under N_2 (the necks are connected respectively to the addition funnel, the distillation head, the mechanical stirrer and the nitrogen line/exhaust) containing 745 g (5.0 mol) triethanolamine $(HOCH_2CH_2)_3N$ 98% (Aldrich) and ≈ 1 L of ethanol; to reduce the viscosity of the triethanolamine. After complete addition of the aluminum tri-(*sec*-butoxide), the by-product (*sec*-butanol) and ethanol solvent were distilled off until a viscous yellow solution was obtained. The resulting solution was analyzed by TGA for ceramic content. The ceramic yield was confirmed by thermogravimetric analysis, typically 8-10 wt% Al_2O_3.

2.2.2.2 Yttrium methoxyacetate, $Y(O_2CCH_2COCH_3)_3$

Anhydrous YCl_3 (25.0 g, 0.0825 mole) was introduced to a 250 mL two-necked flask equipped with a magnetic stir bar and reflux condenser under N_2. Methoxyacetic acid ($CH_3COCH_2CO_2H$, 50mL, 0.65 mole) was then added via syringe and the solution was heated for 2 h to the boiling point of methoxyacetic acid (135°C) during which time byproduct HCl (g) was vented to a hood. After reaction was complete (≈ 2 h), the solution was cooled, filtered and additional methoxyacetic acid added to produce a 50 mL solution with a TGA ceramic yield of 37 wt. %. The exact product formed was not determined but is assumed to be similar to the propionate below.

2.2.2.3 Yttrium propionate, $Y(O_2CCH_2CH_3)_2OH$

$Y(NO_3)_3{\cdot}6H_2O$ powder (50.0 g, 0.1306 mole) was placed in a 500 mL three-necked flask equipped with a still head, addition funnel, under a flow of N_2 sparged directly into the liquid via a fritted glass tube. The N_2 flow also serves the function of stirring the solution. Propionic acid (250 mL, 3.40 moles) was added rapidly and the resulting solution heated to the boiling point of propionic acid (145°C) for 6 h to distill off ~150 mL of liquid (water/propionic acid) and release NO_x gas. A pH-meter probe was placed in a water bubbler above the distillation pot, to monitor release of NO_x. The pH decreases from 8 to 3.5 during the reaction. When the reaction no longer releases any detectable NO_x (small quantities of NO_x in propionic acid give a orange/red hue to the solution), the solution is then cooled for one hour under N_2.

The solution is then tested (to confirm the presence of yttrium propionate) by adding 0.5 ml of the solution to 25 mL of ethanol and 1 gram of aluminum acetylacetonate ($Al(CH_2COCH{=}CO)CH_3)_3$, insoluble in ethanol): yttrium propionate ($Y(CH_3CH_2COO)_2OH$) complexes with the aluminum acetylacetonate, as discussed in Chapter three and the test-solution becomes clear after 5 second of manual stirring (the complex formed being soluble in ethanol), confirming the presence of yttrium propionate.[yp]

50 mL of THF is added to precipitate the product. The precipitated product is washed with another 50 mL of THF and dried in flowing nitrogen for 30 min and then vacuum for 4 h. The dry product was characterized as discussed in Chapter three, and identified as $Y(O_2CEt)_2OH$.

2.2.2.4 Chromium propionate, $Cr(O_2CC_2H_5)_3$

$Cr(NO_3)_3{\cdot}6H_2O$ powder (100 g, 0.29 mole) was placed in a 1000 mL three-necked flask equipped with a still head, addition funnel, under a flow of N_2 sparged directly into the liquid via a fritted glass tube. Propionic acid (500 mL, 6.8 moles) was added rapidly and the resulting solution heated to the boiling point of propionic acid (145°C) for 12 h to distill off ~250 mL of liquid (water/propionic acid) and release NO_x gas. The solution is then placed in a rotary evaporator until all solvents are evaporated leaving a dry red solid. The precursor was identified by TGA-DTA: After evaporation of residual solvent, two mass losses are observed. The first one is attributed to the reaction:

$$Cr(O_2CEt)_3 \longrightarrow Cr(OH)_3 + 3CH_3CH{=}C{=}O$$

The calculated mass loss is 62.0% (observed mass loss is 62.3%)

The second mass loss is attributed to

$Cr(OH)_3 \longrightarrow 0.5\ Cr_2O_3 + 1.5\ H_2O$

The calculated mass loss is 12.9% (observed mass loss is 12.7%).

2.2.2.5 Neodymium propionate, $Cr(O_2CC_2H_5)_3$

$Nd(NO_3)_3{\cdot}6H_2O$ powder (50 g, 0.11 mole) was placed in a 500 mL three-necked flask equipped with a still head, addition funnel, under a flow of N_2 sparged directly into the liquid via a fritted glass tube. Propionic acid (250 mL, 3.40 moles) was added rapidly and the resulting solution heated to the boiling point of propionic acid (145°C) for 8 h to distill off ~150 mL of liquid (water/propionic acid) and release NO_x gas. The solution is then placed in a rotary evaporator until all solvents are evaporated leaving a dry purple solid. The precursor was identified by TGA-DTA: After evaporation of residual solvent, two mass losses are observed. The first one is attributed to the reaction:

$Nd(O_2CEt)_3 \longrightarrow Nd(OH)_3 + 3CH_3CH{=}C{=}O$

The calculated mass loss is 46.3% (observed mass loss is 46.2%)

The second mass loss is attributed to

$Nd(OH)_3 \longrightarrow 0.5\ Nd_2O_3 + 1.5\ H_2O$

The calculated mass loss is 9.6% (observed mass loss is 9.6%).

2.3 General processes

This section describes the LF-FSP and SF-FSP process used in this thesis as well as the techniques used to process the nanopowders obtained.

2.3.1 Liquid-feed and suspension-feed FSP

The apparatus used for LF-FSP and SF-FSP consists of an aerosol generator, a combustion chamber and an electrostatic powder collection system.

The aerosol generator consists of a pump injecting the solution/suspension in a Bernoulli mist nozzle, with oxygen used as the aerosol gas

Two methane/oxygen pilot torches ignite the aerosol formed by the nozzle in the quartz combustion chamber. The chamber can have two air intakes located at the pilot torches and/or 1 meter from them. Combustion produces temperatures >1500°C which can be adjusted by the solution/oxygen ratio, the pumping rate, the air intakes and the precursors in solution/suspension.

The nanosized oxide powders resulting from the combustion are collected in aluminum electrostatic precipitators (ESP, kept at 10 kV potential and air cooled) connected to the combustion chamber by quartz connectors. The production rate was typically ~50 g/h (range of 10-200 g/h).

2.3.2 Heat treatments

Heat treatments in air were conducted in a Lindberg/Blue box furnace (Model No. 58114, Watertown WI, controlled by a Eurotherm microprocessor, model No. 818P, Northing, England). Heat treatment under controlled atmospheres were done using a Lindberg 55322 tube furnace (using a quartz tube) for dry air/oxygen/nitrogen up to 1200°C or a Thermolyne 54500 tube furnace (using a 99% dense alumina tube) up to 1500°C or under vacuum/hydrogen-nitrogen. Pressure was kept at 15 psi for controlled atmosphere. Heating rates and specific dwelling times are described in their respective chapters.

2.3.3 General formation of green compacts

Nanopowders (5g per batch) were dispersed in 250 mL of acetone/water solution (10/90 volume ratio) using a 12.57 mm ultrasonic horn (Sonics and Materials 600 VCX, Newtown, CT) for 50 min in a Teflon beaker (cycle of 10 minute at 10% power, 20 minute at 40%, 10 minute at 25%, 10 min at 40%). Pre-dissolved surfactants (2 wt% bicine or 2 wt% stearic acid in water) were added if needed as described in Chapters four and five. The suspension was left idle for 8 h to settle any large particles. The dispersed powders were dried at 100°C overnight and ground. The powders were then sieved using a 200-mesh nylon sieve and re-dispersed in either ethanol/acetone or water/acetone with pre-dissolved binders (PVA, PEG, PMA) as described in Chapters four and five. They were than dried at 70-100°C for 12-48 h, ground in an alumina mortar and pestle and sieved with a 400-mesh nylon sieve.

The modified powders were then pressed (100-170 MPa) in a 12.57 mm dual action tungsten carbide coated die before being pressed (250-350 MPa) in an isostatic press (Autoclave Engineers, Erie PA).

2.4 Analytical methods

This section describes the various analysis techniques used to analyze the nanopowders obtained by LF-FSP/SF-FSP, the green bodies and sintered monoliths made from these nanopowders.

2.4.1Thermal gravimetric analysis-differential thermal analysis (TGA-DTA)

TGA-DTA was performed on a SDT 2960 simultaneous DTA-TGA (TA instrument, Inc., New Castle, DE). The instrument was calibrated with gold supplied by Perkin-Elmer. Measurements were performed under a continuous flow of air (60 mL/min). Samples (100 mg) were heated at 10°C/min to 1400°C and then allowed to cool to ambient at 20°C/min. If needed additional runs were made using a ramp rate of 10°C/min to 850°C and then 1°, 2° or 5°C/min to 1200°C to determine activation energies of the exothermic reactions observed.

2.4.2 X-ray diffraction analysis (XRD)

XRD was performed on a Rigaku Rotating Anode Goniometer (Rigaku Denki Co., LTD., Tokyo, Japan). The powders were packed on a glass specimen holder. XRD scans were made from 10° to 60° 2θ, using a scan rate of 1-2°/min in 0.05° increments and CuKα radiation (1.542 A°) operating at 40 kV and 100 mA. The Jade program (version 3.1 and 7.0 from Materials Data, Inc, Livermore, CA) was used to identify the crystallographic phases and to determine the relative phase compositions.

For this latter part, we first used the phase analysis integrated function of the Jade program, then used a simulation function to confirm the results. The size of the particles is an important parameter for this simulation and was chosen as the mean average size given by the surface area analysis. The particle size was then adjusted until the simulated pattern matched the XRD pattern. X-ray broadening was also used to confirm the size obtained by surface area analysis and simulation.

2.4.3 Diffuse reflectance FTIR spectra (DRIFTs)

DRIFTs were recorded on a Galaxy series 3000 FTIR (Mattson Instruments, Inc, Madison, WI). Each sample consisted of 500 mg of single crystal KBr first ground in an alumina mortar and then mixed with 5 mg of nanopowder and ground again. A new reference sample (500 mg ground KBr) was made every 5 samples. The system was flushed with nitrogen for 15 min before each analysis to remove atmospheric CO_2. Each analysis consisted of a minimum of 64 scans and the resolution was ± 4 cm^{-1}.

2.4.4 Surface analyses

Specific surface area analyses were conducted at 77K using a Micromeritics ASAP 2000 (Norcross, GA), with N_2 as the adsorbate gas. Samples were degassed at 400°C until the outgas rate was 5 mm Hg/min. The specific surface areas were calculated using the BET multipoint method with a minimum of 5 data points. The particle average size (APS) was derived from the equation 4 (<R> is the average particle diameter, ρ is the density and ssa is the specific surface area obtained from the BET method):

$$<R> = \frac{6}{\rho \times ssa} \tag{4}$$

2.4.5 Scanning electron microscopy (SEM)

Micrographs were taken using a XL30 SEM (Phillips) or a Nova Nanolab dualbeam focused ion beam workstation and scanning electron microscope (FEI, Hillsoboron Oregon). Powder samples were dispersed in distilled water using an ultrasonic horn (Vibra-cell, Sonics and Materials, Inc., Newton, CT). Drops of the dispersed materials were deposited on an aluminum SEM stub and dried for 3 h on a hot plate. Ceramic monolith samples where either cracked or cut and polished, then thermally etched at 1200°C in air. All samples were then coated with a gold/palladium coating by sputtering for 1-2 min, using a Technics Hummer VI sputtering system (Anatech, Ltd., Alexandria,VA).

2.4.6 Transmission electron microscopy

Micrographs were taken on a JEOL 2100 XL (JEOL, Tokyo Japan). Samples were prepared using a carbon coated copper TEM grid (300 mesh). The powder was dispersed in distilled water using an ultrasonic horn, as above, and then a drop of the dispersed powder/water mixture was deposited on the grid. The grid was then dried for 4 h at 80^oC. The JEOL 2100 XL was used with an accelerating voltage of 200 kV.

2.4.7 Sintering curves

Constant heating rate sintering curves were obtained using a Dilatronics 6548 (theta, Port Washington, NY) operating under 10 psi (oxygen, nitrogen or air) or under vacuum. Samples consisted of sections of the green bodies (after binder burnout as described in chapter four and five) and heating rates were 1-20°C/min.

Chapter 3: Yttrium aluminum garnet nanopowders produced by liquid-feed flame spray pyrolysis (LF-FSP) of metalloorganic precursors.

3.1 Introduction

We report here the synthesis of yttrium-aluminum garnet oxide ($Y_3Al_5O_{12}$) nanopowders by liquid-feed flame spray pyrolysis (LF-FSP) of combinations of yttrium and aluminum precursors dissolved in EtOH, nBuOH and/or THF. These include solutions of: yttrium and aluminum nitrates in EtOH or nBuOH; yttrium 2-ethylhexanoate and alumatrane [$N(CH_2CH_2O)_3Al$] in THF or EtOH; yttrium methoxyacetate and alumatrane in EtOH; yttrium acetylacetonate and alumatrane in EtOH, and yttrium propionate and aluminum acetylacetonate, in EtOH or THF. Each precursor system was aerosolized using oxygen and subsequently ignited. Following combustion, the resulting powders were collected by electrostatic precipitation at rates of 50 g/h.

Surprisingly, the precursor choice strongly influences both the initial phase composition and morphology of the LF-FSP powder, as well as the phase changes that occur during annealing. As-collected LF-FSP nanopowders ($\leq$100 nm ave. particle size) had the YAG composition of the precursor feed; but XRD shows what initially appears as a mixture of hexagonal $YAlO_3$ (I) and $Y_4Al_2O_9$ (YAM). Since such a phase mixture cannot account for all the alumina in the powder, the remaining alumina would be anticipated to be present either as nanosegregated amorphous alumina or in defect structures. However, the most homogeneous powders exhibit FTIR, TGA/DTA, TEM and XRD data that suggest a new phase with a modified $YAlO_3$ (I) crystal structure and a YAG composition. Annealing studies demonstrated that at 900-1000°C (7-10 d) these powders transform without coincident grain growth or necking to free-flowing YAG phase powders. The activation energy for this phase transition was found to be $\approx$100 kJ/mol, much lower than most reported values.[1]

YAG ($Y_3Al_5O_{12}$) materials in various forms have proven useful for many diverse applications. For example, Ce^{3+} doped YAG is a phosphor used for fast response scanners and scintillators.[2-5] YAG phosphors have also been well studied because of their stability in electron beams.[6] YAG single crystals grown from the melt are used for laser applications.[7] Polycrystalline YAG exhibits extremely low creep, and melts at ~1900°C, making it an excellent material for high temperature structural applications.

YAG nanopowders offer the potential to carefully control the final grain structure in dense polycrystalline YAG[8] used for structural applications, while nanosized spherical particles offer potential for higher definition and brightness in phosphor applications.[3] Sintered micron-sized YAG powders provide efficient, transparent, polycrystalline YAG lasers as well.[9] In addition, a wide variety of nanopowders exhibit lasing properties that differ from micron-sized powders: an emission behavior explained by Anderson localization of light and now reported by several groups.[10-12,14] Hence there is significant motivation to develop methods of preparing large-scale quantities of high quality YAG nanopowders.

Many techniques have been used to synthesize YAG nanopowders including coprecipitation,[15] gel entrapment,[16] spray pyrolysis[17-18] and thermal decomposition of mixed-metal alkoxides.[19] Although YAG is the thermodynamically stable phase; kinetically favored phases [e.g., hexagonal, orthorhombic or cubic $YAlO_3$ and monoclinic $Y_4Al_2O_9$] often form first in these processes. For example, hexagonal and orthorhombic $YAlO_3$ are the common kinetic phases formed during gas phase synthesis techniques. Nyman et al[18] studied the influence of precursor on the formation of YAG during spray pyrolysis, concluding that short reaction times prevent the formation of the YAG phase (they obtained Y_2O_3 and hexagonal $YAlO_3$). In earlier work from these laboratories, Baranwal et al were able to use LF-FSP of metalloorganics to produce YAG composition ($YAlO_3/Al_2O_3$) nanopowders.[20] However, efforts to transform these $YAlO_3/Al_2O_3$ nanopowders to pure YAG phase by heating led to extensive particle necking followed by excessive grain growth.

We report here the successful synthesis of YAG composition nanopowders that readily transform to YAG phase without necking or particle growth. We further report on the surprising effects of changes in precursor chemistry on the properties of FSP derived powders.

3.2 Experimental Section

Additional information can be found in Chapter 2

Yttrium proprionate (Precursor 6 and 7).

The dry product described in chapter 3 was characterized as discussed below. The ^{1}H NMR data for the resulting material is listed in Table **3.1**. The peaks at 4.8 and 3.1 ppm can be attributed to trace amounts of methanol solvent used in the precipitate synthesis. Peaks attributed to THF of crystallization are found at 3.52 and 1.66 pm. The peaks at 2.05 and 0.89 ppm correspond to the CH_2 and CH_3 groups of the propionate ligand. Note that the integration ratio of the peaks attributed to THF:peaks attributed to the proprionate was constant in four different samples suggesting that the compound forms a stable THF solvate, as discussed below in more detail.

3.3 Results

As noted above, the goal of this work is to produce unaggregated, single crystal, phase pure, dispersible, YAG nanopowders using the LF-FSP process. We recently learned that despite the fact that the LF-FSP flame temperatures range from 1500° to 2000°C, the choice of precursor seems to make a considerable difference in the quality of the powder produced both in terms of phase and particle morphology.[13,22,23] As a consequence, especially because of our previous failure to make high quality YAG nanopowders, we revisited these materials, the types of precursors used, and can now report success.

In recent studies on LF-FSP processing of high quality alumina powders, we determined that metal nitrates although relatively inexpensive are actually very poor precursors for FSP processing since they tend to form larger (200-2000 nm) hollow particles, whereas alumatrane $(NCH_2CH_2O)_3Al$ provides access to very high quality powders.[13] Based on these results, and our previous experience in making spinnable YAG precursors,[37] we selected a series of possible FSP precursors and precursor formulations, including the nitrates listed in Table **3.2**. We then used these seven precursors to produce nine different powder samples, which we analyzed using various analytical tools (BET, SEM, XRD, FTIR, TGA-DTA), to determine the optimal precursor in terms of powder size, morphology and ease of conversion via annealing to dispersible YAG nanopowders. We also obtained a commercial sample of YAG precursor powder from Tal Materials Inc. Our discussions begin with the precursor materials.

3.3.1 Precursor formulations

The seven different precursor systems used are those listed in Table **3.2**. Previously, our understanding of the FSP process was such that we assumed that precursor chemistry would not make a difference in the type of nanopowders produced, given the high flame temperatures, which were assumed to convert any precursor compounds to ions, simple oxide molecules or clusters.[20,22,23] However, as noted above, this proved not to be the case.

Consequently, we began studies to elucidate the various chemistry issues with coincident goals of producing optimal mixed-metal oxide nanopowders using LF-FSP processing. As shown below, the yttrium proprionate based YAG precursor systems offer the best nanopowders produced to date. Hence, we begin by describing the nature of this yttrium precursor system.

Yttrium propionate

Yttrium propionate was prepared from yttrium nitrate using the method described in the experimental section. The resulting product can be precipitated from reaction solutions as a white powder upon addition of THF. Following vacuum drying, FTIR of the dry powder shows a strong ν-OH peak at 3370 cm^{-1}. Two broad peaks observed at 1500 and 1290 cm^{-1} correspond to νC-O bands of bound carboxylate groups. The FTIR suggests the presence of at least one hydroxyl group on the yttrium.

^{1}H NMR (see experimental) studies confirm the presence of the propionate groups but no OH proton, which is expected because of rapid exchange with the deuterated solvent. Surprisingly, ^{1}H NMR reveals the presence of THF solvent molecules in a ≈ 2:3 THF:yttrium propionate ratio. This ratio was constant in four different batches of the powder. The presence of THF solvate is further supported by the TGA results.

TGA studies were conducted to identify the decomposition patterns for comparison with our previous work.[25,37] In the TGA (Figure **3.1**), a mass loss of ≈ 16 wt. % is observed beginning at ≈ 100°C (10 °C/min/air) and is assumed to be loss of THF of crystallization.

After loss of the solvate molecules, a further mass loss is observed (≈ 175°C, Figure **3.1**) of 39 wt %. If we ignore the solvent loss for the moment, then the actual ceramic yield at this point is 53.2 %. On further heating, a slower mass loss of 17 wt. % is observed that appears to continue to ≈ 700°C. The final ceramic yield, disregarding solvent loss is 43.7 wt. %.

Based on these numbers and our previous studies,[25,37] several model compounds can be suggested for the actual structure of the yttrium propionate, as shown in Figure 3.**2**. The corresponding ceramic yields are also given.

Based on the FTIR data and the ceramic yield data, model "a," $Y(O_2CEt)_2OH$, appears to be the correct choice. Further support for this model comes from the following.

If we assume that the precursor is actually $Y(O_2CEt)_2)OH$ (F.W. = 252.006) and THF is present in a 2:3 ratio, then it is possible to calculate that the expected solvent loss will be 16.1 wt. %. We observe a value of 16.1 wt. %. We can then suggest that the 175°C mass loss arises from thermal fragmentation of the carboxylates with loss of ketene based on our earlier studies of metal carboxylate decomposition patterns, and as shown below:[25,37]

$$Y(O_2CEt)_2OH \longrightarrow Y(OH)_3 + 2CH_3CH{=}C{=}O \qquad (1)$$

The expected mass loss is then 43.7 wt % which is exactly that found. The final ≈ 17.0 wt% mass loss can be attributed to loss of the hydroxyl groups, reaction (2), which is calculated to be 19 %.

$$Y(OH)_3 \longrightarrow 0.5\ Y_2O_3 + 1.5\ H_2O \qquad (2)$$

The fact that there are two THF molecules:three yttriums, suggests a trimeric species has formed.

The precursors listed in Table **3.2**, were combusted under conditions very similar to those described in earlier work[20,22] and as described in Chapter 3. Typically, 43 wt % (37.5 mol%) alumina as precursor and 57 wt % (62.5 mol%) yttria as precursor were dissolved in the chosen solvent and aerosolized at rates that led to production of ≈ 50 g/h of powder. The pressure in the aerosol generator was kept at 20 psi. Two methane torches were used to ignite the aerosol.

Although most precursor systems remain soluble for indefinite periods of time; precursor 7 was difficult to work with because of the poor solubility of $Al(acac)_3$ in THF, leading to off-stoichiometries as discussed below. An eighth and ninth sample were prepared using precursor 6 and by increasing the flow speed (as well as improving the regularity of the flow) in the process. These two samples had much smaller particle sizes and correspondingly higher surface areas.

3.3.2 Powder characterization

Given that our goal is to produce high quality YAG nanopowders in terms of particles sizes, surface chemistry, morphology, and phase composition, we begin by discussing powder surface areas and then powder morphology for the nine samples. We first discuss the specific surface areas (SSAs) obtained by porosimetry. The goal is to identify the precursor that produces the highest surface area materials without microporosity as this will provide a first estimate of particle size. FTIR and XRD were then used to analyze the surface chemistry, phases present and also as a second indirect method of determining particle sizes. SEM micrographs were also obtained as a direct method of examining particle sizes and size distributions. This was done primarily to observe the general population especially with respect to larger particles. TEM images were also obtained. As XRD studies showed that YAG phase is not formed directly by FSP, we then conducted TGA-DTA studies to learn which samples convert most easily to YAG phase. These studies provide the basis for determining optimum annealing conditions for conversion to the YAG phase.

3.3.2.1 Surface area analyses.

Mean particle sizes determined from the specific surface areas[24] and x-ray line broadening are shown in Table **3.3**. As seen, the SSAs show a strong dependence on the precursor used and to a lesser extent, on the solvent used. X-ray line broadening studies show very similar results, apart from Sample 2, which consists of a mixture of 30 nm and polycrystalline 200-2000 nm particles.

As expected[13,20,26,28] the nitrate based precursors (Samples 1 and 2) gave low surface area powders. However, precursors that are expected to have significant vapor pressurs,[27] such as the yttrium and aluminum acetylacetonates, and alumatrane permit better mixing and burning conditions,[13] and thus produce finer powders. Hence, FSP powders obtained from precursors 3, 4, 6, and 7 have similar higher SSAs and smaller apparent particle sizes. Note that without the propionate precursor, the acetylacetonates are highly insoluble, suggesting the formation of a mixed-metal precursor in solution.

3.3.2.2 Scanning electron microscopy (SEM)

SEM was used to assess the particle size distribution for the various FSP produced nanopowders. Micrographs show that the particles exhibit spherical morphologies. SEMs of the nitrate-based precursors show large and sometimes hollow particles ranging from 200 nm to 2 μm, Figure 3.3,[13,26] however a significant portion of particles have sizes <100 nm. This suggests that two separate mechanisms contribute to the generation of the nitrate-derived powders. One is premature decomposition common for spray pyrolysis of nitrates.[26] In this process, the nitrates partially melt and then decompose rather than combust on heat up just after exiting the spray nozzle. This produces hollow, large particles typical of spray pyrolysis rather than the fine particles typical of combustion. The second process likely results from straightforward combustion of the spray droplet without melting. These processes may be a consequence of where the droplets are in the cone of mist that exits the nozzle.

In contrast to the nitrate products, Precursors 3, 4 and 6 produce very regular particles. As illustrated for Sample 6 in Figure **3.4**, almost all the particles are 20-50 nm in diameter, as might be anticipated from the SSA and XRD line broadening studies. Samples 8 and 9 consisted of particles in the 5-100 nm range, with most particles in the 5-25 nm range.

3.3.2.3 Thermal analyses (TGA)

TGAs were performed to determine the quantity of various surface species on the powders, water in particular. Sample 1 TGA differs from all the other samples giving a ceramic yield of 99.8 wt. % at 1400°C, which indicates an absence of contaminating surfaces species, as confirmed by FTIR (see below). This observation is surely a consequence of the large average particle sizes, which equates to relatively low SSAs. Sample 2, with a similar SSA behaves differently since significant portions of its particles are much smaller (<30 nm).

All samples, apart from 1 and 6 show mass losses of 1-2 wt. % below 200°C, which can be attributed to water loss (confirmed by FTIR, see below). Samples 7 and 8 exhibit a mass loss of 3-4 wt % at 200°C, indicating a higher proportion of surface species, as expected for the higher surface areas. Although, Samples 6 and 7 have exactly identical surface areas, they do not show similar mass losses. An explanation is that the surface chemistries are different, one favoring formation of chemi- and physisorbed water and the other not. This implies that the atomic mixing is different between Samples 6-9. As such, FTIR of these four samples should show some important differences, especially with respect to the OH peaks.

Sample 5 shows two additional mass losses at 450°C (0.36 wt%) and at 800°C (0.52 wt%). As discussed below, this can be linked to the presence of surface carbonaceous species.

3.3.2.4 FTIR (DRIFT mode)

FTIR was used both to identify surfaces species present on sample surfaces and to observe the phases present. $Y_3Al_5O_{12}$, $YAlO_3$ (I), δ:θ-Al_2O_3 and Y_2O_3 all present very specific FTIR spectra, mostly in the 400-1000 cm^{-1} range.[29-35] As relatively few studies have been made of the FTIR spectra of the other phases in the Y_2O_3-Al_2O_3 system, we decided to compare our samples to reference powders also prepared using FSP.

<u>FTIR reference materials</u>

Yttria powders were prepared by FSP using yttrium proprionate in EtOH (solution ceramic yield, 5 wt%). The XRD powder patterns for these materials indicate formation of a 30/70 mixture of monoclinic and cubic Y_2O_3 (ratio determined by Jade program as described in chapter 3). We also synthesized δ:θ-Al_2O_3 by FSP using an alumatrane solution in EtOH (solution ceramic yield, 5 wt %).[13] Commercial samples of amorphous aluminum hydroxide [$Al(OH)_3$] powder were also used as a reference. A YAG reference material was obtained by heating Sample 6 at 1200°C/30 min/air. A reference YAP sample was also prepared using a 1:1 yttrium methoxyacetate:$Al(Acac)_3$ EtOH solution. XRD was used to confirm the phase. Scans of LF-FSP samples are showned in Figures **3.6, 3.7, 3.9,** and **3.10**. A commercial YAG composition nanopowder from Tal Materials Inc. (TM) is included in Figures **3.7, 3.10**.

Spectra for the various samples, YAG, as-shot yttria, $YAlO_3$ (I) crystallized by heating at 900°C, δ:θ- and amorphous alumina are presented in Figures **3.5** and **3.8**. Most peaks observed in these spectra are common to all samples and can be related to those observed in the reference materials.

Broad peaks between 3800 and 3200 cm^{-1} can be assigned to O-H stretching vibrations (νOH) indicative of the presence of surface hydroxyl groups arising from both physi- and chemisorbed water, per the work of Peri,[31,32] on alumina surfaces. Bands in the 3500 to 3200 cm^{-1} range are attributed to νOH from physisorbed water, while those in the 3800-3600 cm^{-1} range derive from isolated hydroxyl groups.

YAG, δ:θ-alumina[13] and amorphous alumina exhibit similar peaks in this range, showing both types of hydroxyls groups. The $YAlO_3$ (I) sample also shows the same two peaks, but their relative intensities are different. It appears from the νOH band pattern that more physisorbed than chemisorbed water is present on the surface. It should also be noted that hydroxyl peaks in the yttria sample are very weak, while the surface area of this sample is similar to other samples (all reference samples have average particle sizes of 20-50 nm, except the amorphous alumina which consists of micron sized particles and the Tal Materials Inc. sample which has an 80 nm average particle size).

Apart from Sample 1, where no surface species are seen (as expected from its TGA, see Table **3.4**), all samples exhibit typical νOH peaks. Sample 7 exhibits a third water peak centered at 3800 cm^{-1}, which may arise from isolated alumina specific νOH sites per Lee and Condrate.[33]

As noted above, the TGA studies suggest that samples 6 and 7 have different surface chemistries based on their different mass losses in the region where chemi- and physisorbed water come off. The DRIFTS data support this and suggest some nanosegregation within Sample 7 particles or at least at their surfaces, which is likely solvent dependent since the precursors are the same. Thus in addition to precursor effects, solvents also seem to play a role in product formation. The role could take the form of solvation of mixed-metal complexes that form as intermediates or in the flame temperature. Since we note above that Al(Acac)$_3$ is not particularly soluble in THF, we suspect that this is at least partially the reason for the difference in surface chemistries: as discussed above yttrium proprionate appears to form a trimeric species with THF of crystallization. The isolated compound does not react with Al(Acac)$_3$ to form the putative "yttrium proprionate/aluminum acetylacetonate complex." Alternately, it may be that the particles are off-stoichiometry based on the poor solubility. Because THF has a higher fuel value than ethanol, flame temperatures should not be an issue, THF's higher temperatures are likely to favor formation of YAG phase-see above. The fuel value of THF is 2533 kJ/mol[41] while ethanol has a fuel value of 1366 kJ/mol.[42]

The peaks observed in our samples and the reference materials, in the 1560-1600 cm^{-1} and 1320-1380 cm^{-1} regions, are typically assigned to asymmetric and symmetric νC-O bands in carbonate (CO_3^-) species,[33,35] respectively. Given that all our samples are produced in a flame; have small average particle sizes and therefore high surface areas, they can be expected to absorb CO_2 to form carbonate species. The one exception is Sample 1, which has a much larger average particle size and much lower surface area (6

m^2/g) compared to the other samples (>20 m^2/g). Hence CO_2 pickup should be limited, as observed.

For all of the Samples, the peaks below 1000 cm^{-1} are unexceptional, except for the peak at 740 cm^{-1} in most samples. This peak is usually assigned to asymmetric νAl-O in isolated AlO_4 tetrahedra or combinatorial vibrations between AlO_x tetrahedra or pentahedra and AlO_6 octahedra as discussed by Saniger[34] and Tarte.[35] As such, this peak is not observed in δ:θ-alumina,[13] $Al(OH)_3$, nor in the YAP reference (made with a 1:1 Y/Al ratio). In the Y_2O_3-Al_2O_3 system, this peak might be expected if excess Al^{3+} (Y:Al ratio <1) substitutes for Y^{3+} in the $YAlO_3$ (I) phase. It is also observed in the YAG phase[29,30] where all Al^{3+} ions are located in isolated AlO_4 tetrahedra and AlO_6 octahedra. As such this peak is observed in the reference YAG sample as expected. However based on the characteristic YAG peaks (see Table **3.5**), these materials are not YAG.

The 740 cm^{-1} peak is observed in Samples 5, 6, 8, 9 and the Tal Materials (TM) sample and to a lesser extent in Samples 1 and 7. Note that although sample 4 gives good particle sizes this peak is absent, suggesting different mixing at the nanoscale. This type of intimate mixing at the very least has important implications vis a vis YAG phase crystallization activation energies and temperatures as discussed below. This will be discussed further in Chapter four as indicative of a new $Y_3Al_5O_{12}$ phase.

3.3.2.5 XRD analyses

Figures **3.11** and **3.12** provide XRD data for the as-processed samples. The YAG phase from an annealed sample (see below) and pure $YAlO_3$ (I) phase are shown at the bottom to illustrate the differences. As expected from our earlier work,[20] none of the precursors provide YAG phase in the as-processed FSP powders. Among the known crystalline phase in the Y_2O_3-Al_2O_3 system only a mixture of $YAlO_3$ (I) and some YAM phase seem to match the XRD pattern observed. Close examination reveals that the match is far from perfect which will be discussed in much more detail in chapter four as it indicates a new crystalline phase.

It should be noted that Sample 1 was mostly amorphous. Differences in flame temperature and in cooling rates, due to differences in the combustion of the various precursors could explain the phase variation between samples, but further studies of flame temperature effects must be made to fully understand this phenomenon. In addition, despite the differences in the FTIR for Samples 6 and 7, their XRDs show essentially identical powders.

Kriven et al[1] have reviewed the effects of temperature on YAG crystallization in variously processed YAG composition powders. They found that the temperature determined which intermediate phase would form on crystallization of YAG. This could partially explain the influence of flame temperature and cooling rate on the phase distribution seen here.

$YAlO_3$ and $Y_4Al_2O_9$ are aluminum deficient compared to the 3:5 Y:Al ratio of the precursors used to produce Samples 1-9 and TM. Thus, around half of the Al^{3+} ions must be present in an amorphous phase or are in defect structures wherein Al^{3+} for Y^{3+} substitution occurs in the $YAlO_3$ (I) phase as discussed above.

The above FTIR interpretation suggests that for Samples 5-9 and TM, the latter hypothesis may be the correct interpretation, as Al^{3+} ions appear to be present in defect positions. Similar hypotheses were made by Yamaguchi[38] and Veitch,[39] who both observed the formation of several $YAlO_3$ phases as intermediary to YAG formation in differently processed YAG composition powders and explained the placement of the excess Al^{3+} by either defects[38] or amorphous phases.[39] Intermediate $YAlO_3$ phases were also observed by Hess et al[40] who studied the crystallization of YAG from amorphous powders. They suggest that low temperature reactions could allow the direct formation of YAG, as earlier work in our group[37] also indicates, while higher temperatures would result in the formation of intermediate $YAlO_3$. The question of placement of the excess Al^{3+} remains unresolved. Quick calculations from the XRD patterns suggest that in all samples ≈ 50% of the Al^{3+} is unaccounted for. Based on stochiometry one would expect an amorphous hump to be easily observed in the XRD if these Al^{3+} were in an amorphous phase. The absence of an amorphous hump in all samples but Sample 1 makes the presence of an amorphous phase dubious and again suggests the excess Al^{3+} is present in a regular defect structure.

Given that that the XRD 2θ values for the peaks mostly correspond to the $YAlO_3$ (I) phase, but not to the peak intensities [e.g. in particular the (002) peak is only a fraction of its theoretical intensity] we sought to identify a peak associated with the defect structure. Thus, further XRD studies were done at lower angles. Figure **3.13** reveals the presence at

8.3-8.5 °2θ peaks in Samples 5, 6, 8, 9 and the TM commercial sample, but not in Sample 4 as might be expected from the absence of the 740 cm^{-1} peak in the FTIR. Also important is that YAG samples (obtained from sample 5 and 6 after annealing at 1200^{o}C/30min) don't show this peak. This is despite the fact that a peak in this range should correspond to a lattice parameter of ≈ 1.1 nm, close to the unit cell dimensions for crystalline YAG and close to the (001) interplanar distance of $YAlO_3$ (I). Authentic samples of $YAlO_3$ (I) do not exhibit this peak because of the equivalence between (002) and (001) planes. While qualitatively, samples with finer particle sizes (6, 8, 9) show much stronger peaks in this region, the TM sample also exhibits a strong peak despite the larger particle size.

3.3.2.6 Transmission electron microscopy (TEM)

TEM studies were performed to examine particle morphology. Almost all particles are below 100 nm with most in the 10-50 nm range, as expected from Table **3.3**. Figure **3.14** gives a representative image.

3.3.2.6 Annealing

Given that our goal is free flowing, high quality YAG phase nanopowders and given that none of the as-processed powders were YAG phase by XRD, we resorted to annealing to effect conversion to the YAG phase without necking. To determine the optimum annealing temperature and duration, DTA studies were first run as shown in Figure **3.15**.

Most samples exhibited several exotherms. To identify the various processes associated with these exotherms, samples were heated to just beyond the exotherm temperature (at the same heating rate of 10°C/min), cooled (-10°C/min) and then analyzed by XRD.

All precursor-derived powders except Samples 5, 6, 8 and 9 show two exotherms, the first exotherm is actually two nearly coincidental peaks which were discerned by running additional DTAs at lower heating rates (1°C/min). These peaks correspond respectively to the formation of the $YAlO_3$ (II) and YAM phases as confirmed by XRD (one example is seen in Figures **3.16**).

Clearly, the Samples that do not show the 740 cm^{-1} peak in the FTIR nor the 8.3 °2θ peak in the XRD do not offer the degree of atomic mixing and homogeneity of the other materials. This again points to differences in molecular structures in the precursors and to the formation of different species or poorly mixed species in the gas phase. The conclusion is that chemistry is very important in the FSP process, as discussed in more detail below.

Note that the exotherms for Samples 1 and 2 are at higher temperature than for the other samples. The DTA data for Samples 5, 6 and 9 differ in having only one obvious exotherm >800°C, the $YAlO_3$ (II) and YAM peaks are very faint and can only be observed on heating at 1°C/min. Further XRD and DTA analyses showed that these phases form but at slower rates than with the other precursors. This could be explained by a regular defect structure (or new intermediate phase) as suggested by the FTIR, XRD and TEM: the uniform dispersion of Al^{3+} would favor a direct reaction path to YAG, which would, for these two samples, have a lower E_a than the YAH path. In this direct reaction path, the defect (new intermediate phase) structure should lower the Ea, as the Al^{3+} ions needs less displacement in transforming from the $YAlO_3$ (I) to the YAG crystal structure, as discussed below.

Sample 5 also exhibits an exotherm at 450ºC, which likely corresponds to the elimination of traces of carbonaceous surface species as confirmed by the mass loss observed in the TGA. It is important to note that the only carbonaceous species seen above are carbonates as seen in Figures **3.6** and **3.7**.

Given that the DTA exotherms for YAG conversion (1100°-1400°C) occur at temperatures where necking and sintering are anticipated to occur, and based on annealing studies of nano-mullite powders,[22] we explored the use of annealing to promote phase transformation at 800°-900°C. With the goal of converting the powders to the YAG phase in a reasonable amount of time, without necking; we determined the activation energy (E_a) for phase conversion using methods similar to those of Kriven.[1]

We used the constant heating method, with the modified Kissinger equation to calculate E_a in Table **3.6** from the shift of the YAG exotherm in the DTA (T_m-T_0) with changes in heating rate (c is a constant, α is the heating rate, T_m is the peak temperature of the exotherm observed on a DTA run at the rate α>5°C/min , T_0 is the peak temperature of the exotherm when the DTA run at the rate of 5°C/min):[1]

$$\ln\left(\frac{\alpha}{T_m - T_0}\right) = \frac{1}{T_m} \times \frac{E_a}{R} + c$$

These activation energies provide a reasonable basis for defining the annealing studies and for choice of the optimum precursor. According to the activation energy calculations, complete conversion to the YAG phase should occur after annealing at 850°C for 10 d with Sample 6. We were able to confirm complete conversion to YAG (100% YAG crystalline phase as observed by XRD): 850°C for 10 days with Sample 6. This temperature is much lower than the usual temperature for YAG formation,[15-18] and allows conversion without necking or particle growth (SSA remains unchanged at 39, 79, 92 m^2/g for Samples 6, 8 and 9 respectively and SEM shows no necking).

General comments:

Both DTA and FTIR seem to indicate that samples 5, 6, 8, 9 and TM have better atomic mixing, which may be explained by the formation of mixed-metal precursor complexes. We have previously reported that the formation of yttrium:aluminum mixed-metal precursors allows direct formation of YAG phase without the intermediacy of YAP or YAM.[37] However, it is still unclear how a mixed-metal solution phase precursor might give a better nanopowder product after combustion.

The simplest explanation is that in the short time before combustion, partial evaporation of the aerosol droplet occurs that might lead to some segregation or vaporization in systems where a mixed-metal precursor cannot form.[36] If we assume that this is the case, then it might be reasonable to argue that combustion leads to a vapor phase were there is an uneven distribution of ions. Due to the rapid quenching that occurs during FSP, this would lead to uneven condensation of these ions to form the first nuclei, as we have discussed earlier.[23]

Finally, the diminution or absence of the 740 cm^{-1} νAl-O band typical of combinatorial vibrations in the other samples (e.g. Sample 4) suggests less efficient mixing during FSP. Less efficient mixing will the regularity of these defects that is indicated by the combinatorial vibration, resulting in the diminution or elimination of this peak.

A metastable, regular defect structure (or new intermediate phase) seems to be caused by this efficient mixing, as FTIR indicates the presence in Samples 5, 6, 8, 9 and TM commercial sample offer a regular defect structure of isolated AlO_x, which will be discussed in greater detail in chapter 5.

Kriven[1] conducted similar studies on YAG crystallization from amorphous YAG composition glass (micron-sized powders) finding an E_a of 427 kJ/mol. In our experiments E_a was found to be much lower and precursor dependent. This was expected, as smaller particle sizes will result in lower E_a for phase formation. But particle sizes alone cannot explain the difference in E_a: in particular Samples 6 and 7 have same average particle size but different E_a, while Sample 5 has lower E_a despite having higher average particle size.

The presence of a regular defect structure or new intermediate phase could explain these differences: A powder with more homogenous mixing of Y^{3+} and Al^{3+} ions (shorter diffusion distances), as this metastable structure will require less energy for conversion to YAG phase than, for example, powders formed from core-shell type condensation mechanisms.[23,28] It should be noted that the much lower E_a values than any previously reported,[1,40] suggest that diffusion in the phase transformation process is intraparticle and short-range, as they are much lower than reported for intergranular diffusion in the YAG phase.

The difference in the DTA analyses can also be explained by a metastable or intermediate phase structure: Samples 5, 6, 8 and 9 all transform directly to YAG which may suggest a metastable intermediate phase, while Samples 1-4 seem to follow a $YAlO_3$ (II) route of transformation. In Samples 5, 6, 8 and 9, the regularity of this structure allows direct transformation to YAG, which can be expected to have a lower E_a than a transformation process via an additional intermediate phase, ie. $YAlO_3$(II).

3.4. Conclusions

Phase pure, dispersible, yttrium aluminum garnet nanopowders are easily synthesized using liquid-feed flame spray pyrolysis followed by careful annealing (850°C for 7 d) at lower temperature than usual in processing YAG powders, due to very low activation energies (≈ 100 kJ/mol). The FSP derived powders can have very high specific surface areas, up to 90 m^2/g. The precursors and to some extent the solvent systems play a critical role in the formation of YAG nanopowders. The data also suggest the formation of a novel phase in the as-processed powders. Additional work on this new phase will be described in Chapter four, including detailed studies on the type of phase/defect structure formed and the low-temperature sintering of these materials.

Peak positions	4.8 ppm	3.52 ppm	3.1 ppm	2.05 ppm	1.66 ppm	0.89 ppm
Integration (multiplicity)	0.25	5.8 (t)	0.1	2.0 (q)	5.76 (septet)	2.83 (t)

Table 3.1 NMR data of the dried yttrium proprionate.

Sample	Y source	Al source	Solvent	Ceramic yield (wt%)
1	$Y(NO_3)_3 \cdot 6H_20$	$Al(NO_3)_3 \cdot 9H_20$	EtOH	2.5
2	$Y(NO_3)_3 \cdot 6H_20$	$Al(NO_3)_3 \cdot 9H_20$	BuOH	5
3	$Y(O_2CCH_2OCH_3)_3$	$N(CH_2CH_2O)_3Al$	EtOH	5
4	$Y(O_2CCHEtC_4H_9)_3$	$N(CH_2CH_2O)_3Al$	THF/EtOH 90/10 mol%	2.5
5	$Y(O_2CCH_2OCH_3)_3$	$N(CH_2CH_2O)_3Al$	$EtOH/H_2O$ 97/3 mol%	5
6/8/9	$Y(O_2CEt)_2OH$	$Al(Acac)_3$	EtOH	2.5
7	$Y(O_2CEt)_2OH$	$Al(Acac)_3$	THF	2.5

Table 3.2 List of precursors formulated (all with 3Y:5Al stoichiometry).

Sample	1	2	3	4	5	6	7	8	9	Tal*
SSA (m^2/g)	5.4	6.7	30	36	14	39	39	**79**	**92**	15
Mean particle size (nm)	247	198	44	37	95	34	34	**16**	**13**	88
Size by line broadening (nm)	na	30	45	35	90	35	35	**15**	**10**	90

*Commercial material obtained from Tal Materials, Inc.

Table 3.3 Initial surface area and mean particle size.

Sample	1	2	3	4	5	6	7	8	9
Ceramic yield Wt %	99.8	98	97.5	98	96	98	96	97	98

Table 3.4 Ceramic yield of the powders at 1400°C

Peaks	Y_2O_3	YAG	$Al(OH)_3$	δ-Al_2O_3	$YAlO_3$ (I)
νOH chemisorbed H_2O	3580 (w,br)	3540 (w,br)	3560 (w,br)	3580 (w,br)	3600 (w,br)
νOH physisorbed H_2O	3210 (w,br)	3210 (w,br)	Broad	Broad	3200 (w,br)
νM-O	570 (s), 500 (s), 460 (m), 430 (w), 410 (w),	440 (m), 500 (s,br), 570 (s), 700 (w), 740 (s,br) and 790 (s)	610 (br)	810 (br) and 610 (br)	440 (s), 500 (s), 650(m), 700 (s),800 (w) 860 (w), 870(w), 900 (w)
νCO carbonate	1575 (w,br), 1350(w,br)	1500 (w,br) 1380 (w,br)	1500 (w,br)	1600 (w,br) 1350 (w,br)	1540 (w,br), 1350 (w,br)

- s = strong, m = medium, w = weak, br = broad; center of peak reported.
- **Table 3.5** FTIR peaks of reference materials (cm^{-1}).

Precursor	1	2	3	4	5	6	7	8	9
YAG formation (°C)	1280	1270	1060	1050	960	1100	1110	1100	1075
E_a (kJ/mol)	210	208	210	280	86	106	166	100	96

The formation starting temperature was obtained at a heating rate of 10°C/min.

Table 3.6. YAG starting formation temperature and E_a.

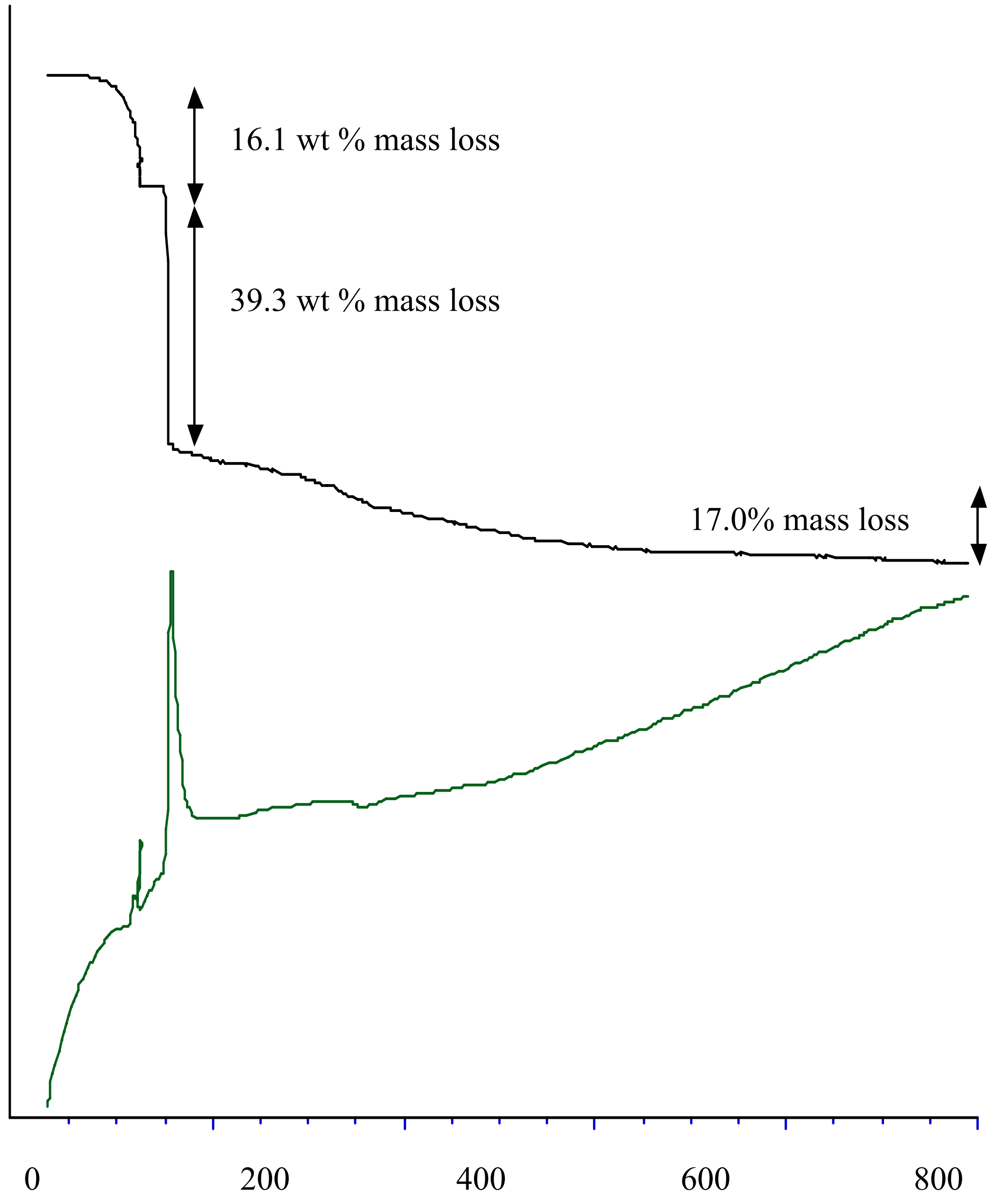

Figure 3.1 TGA (top)-DTA (bottom) of the proprionate powder-THF solvate.

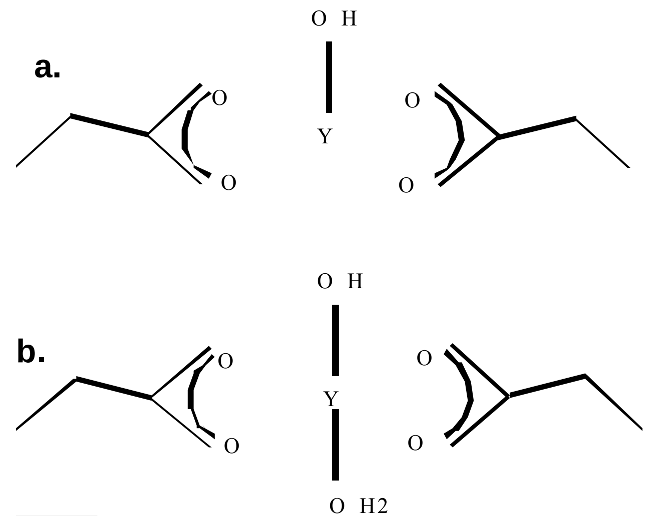

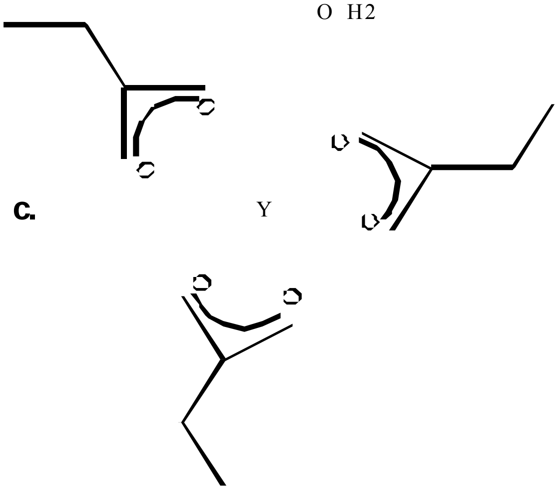

Model/Calc.	Ceramic Yield (wt %)
a	43.0
b	46.0
c	33.9
d	53.6

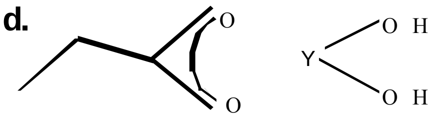

Figure 3.2 Possible structures for the yttrium proprionate precursor.

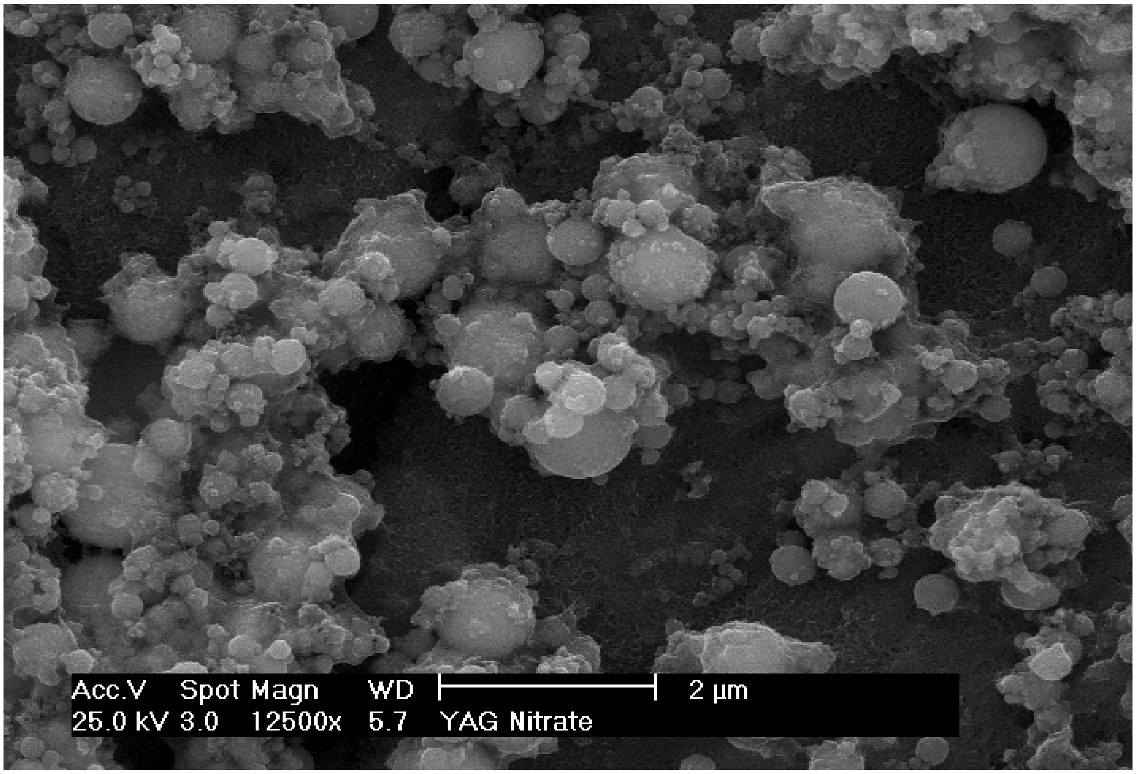

Figure 3.3 Micrograph of Sample 1 (yttrium nitrate/aluminum nitrate).

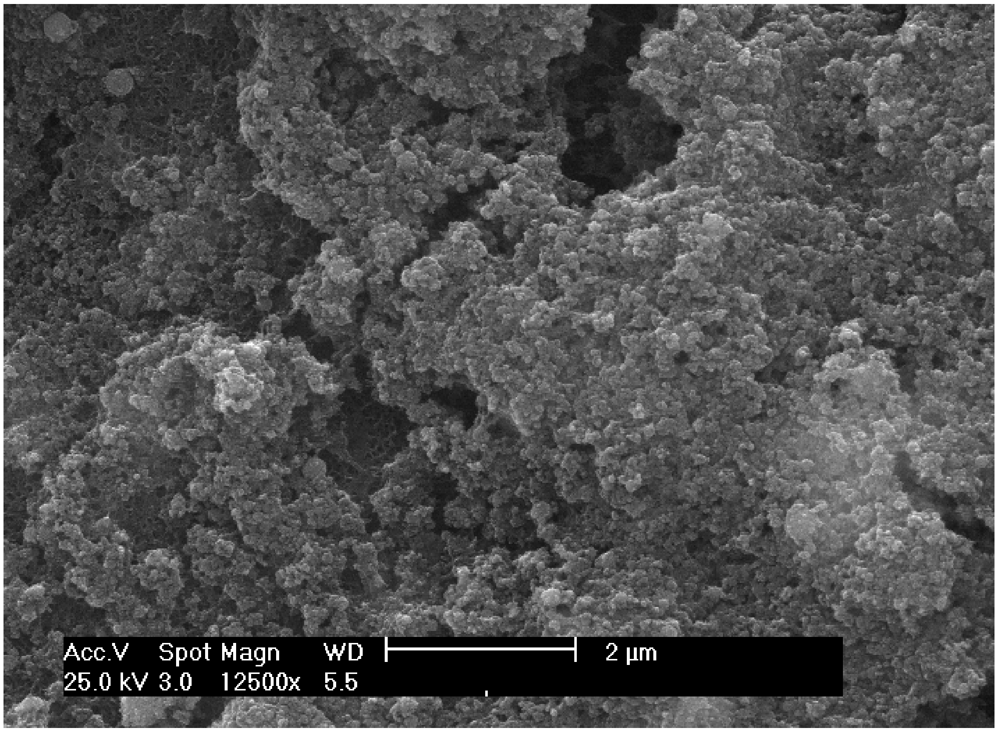

Figure 3.4 SEM micrograph of Sample 6 (yttrium proprionate/aluminum acetylacetonate)

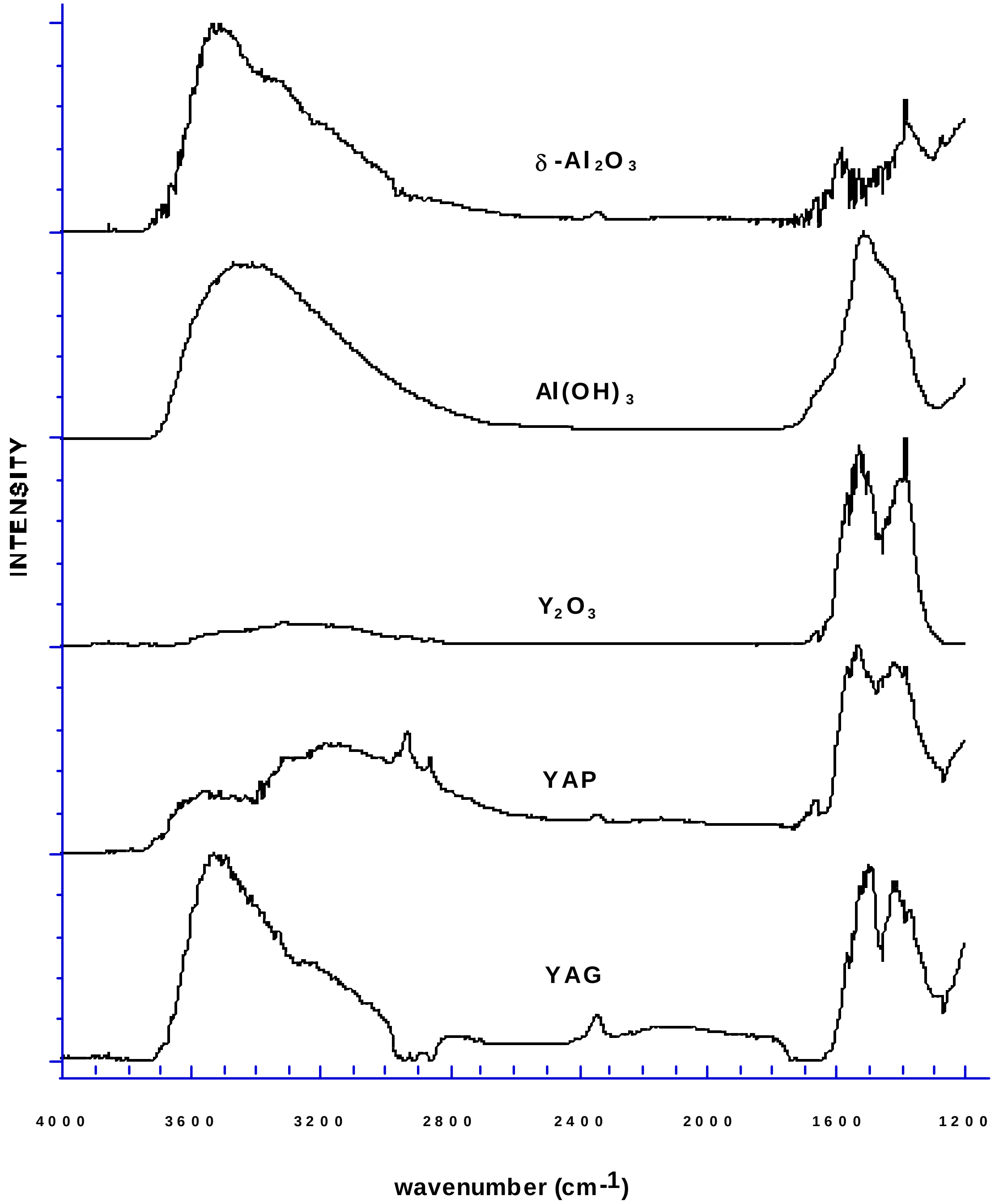

Figure 3.5 FTIR of reference samples (4000-1200 cm^{-1}).

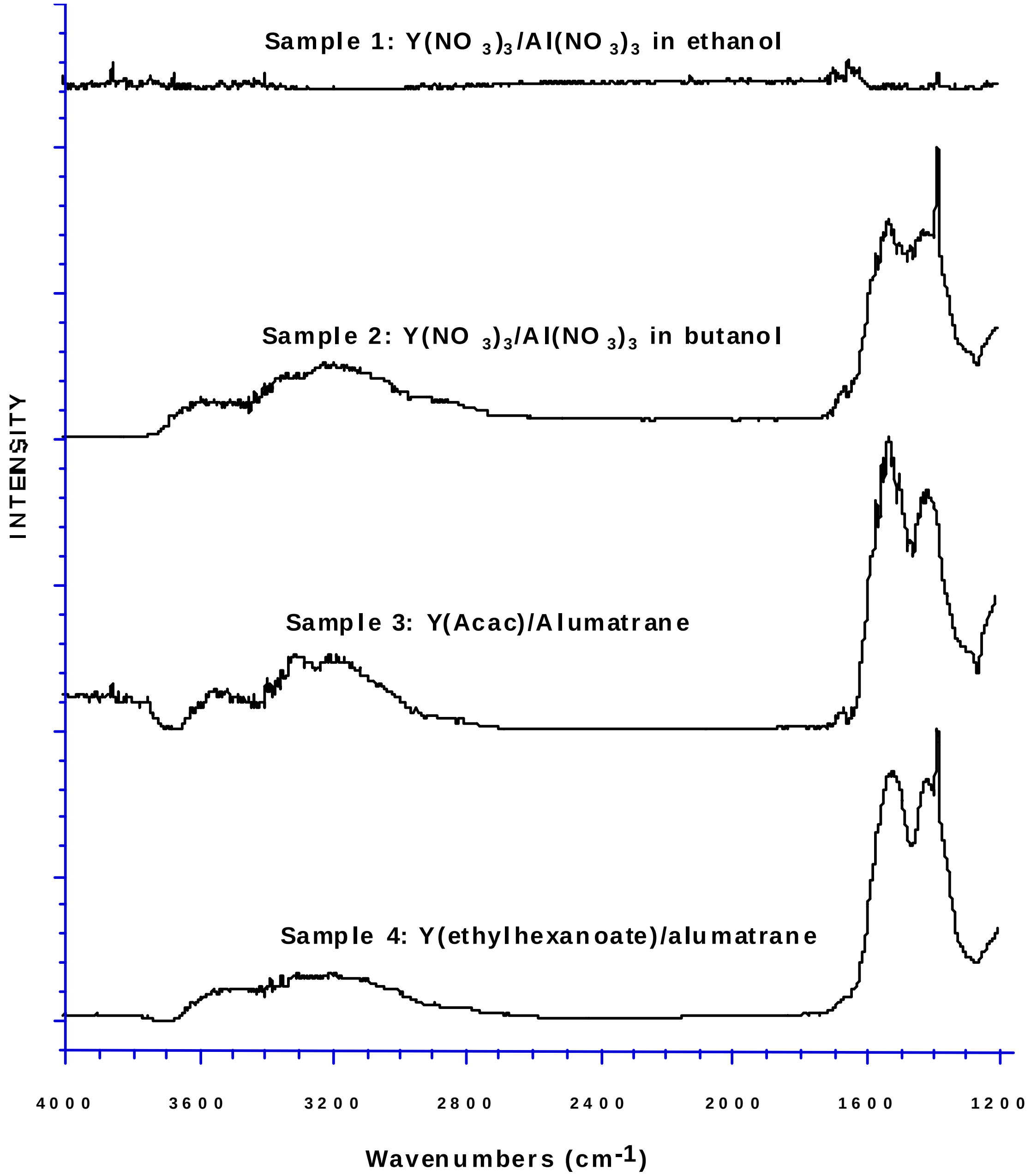

Figure 3.6 FTIR of various samples (4000-1200 cm^{-1}).

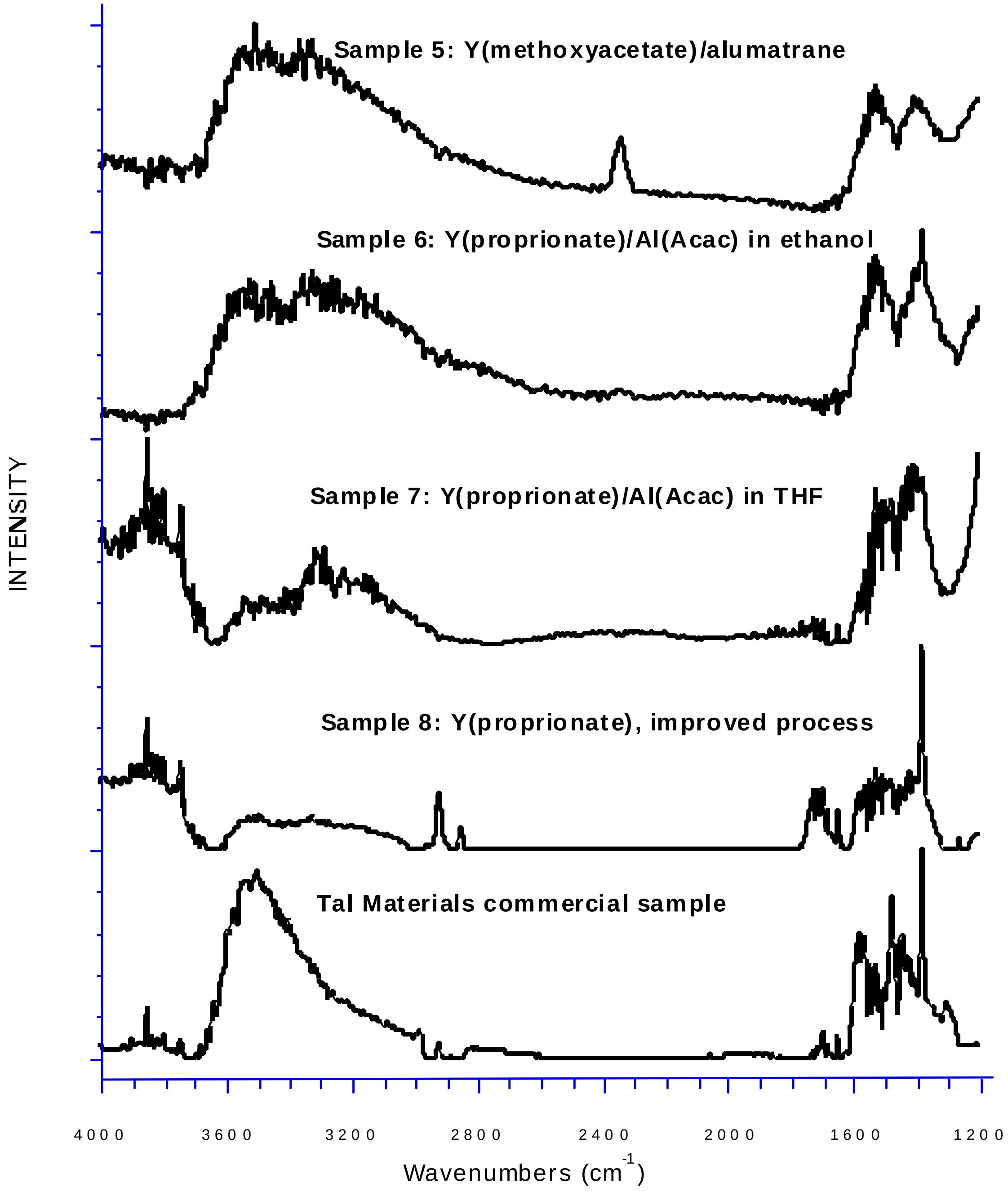

Figure 3.7 FTIR of various samples (4000-1200 cm^{-1}).

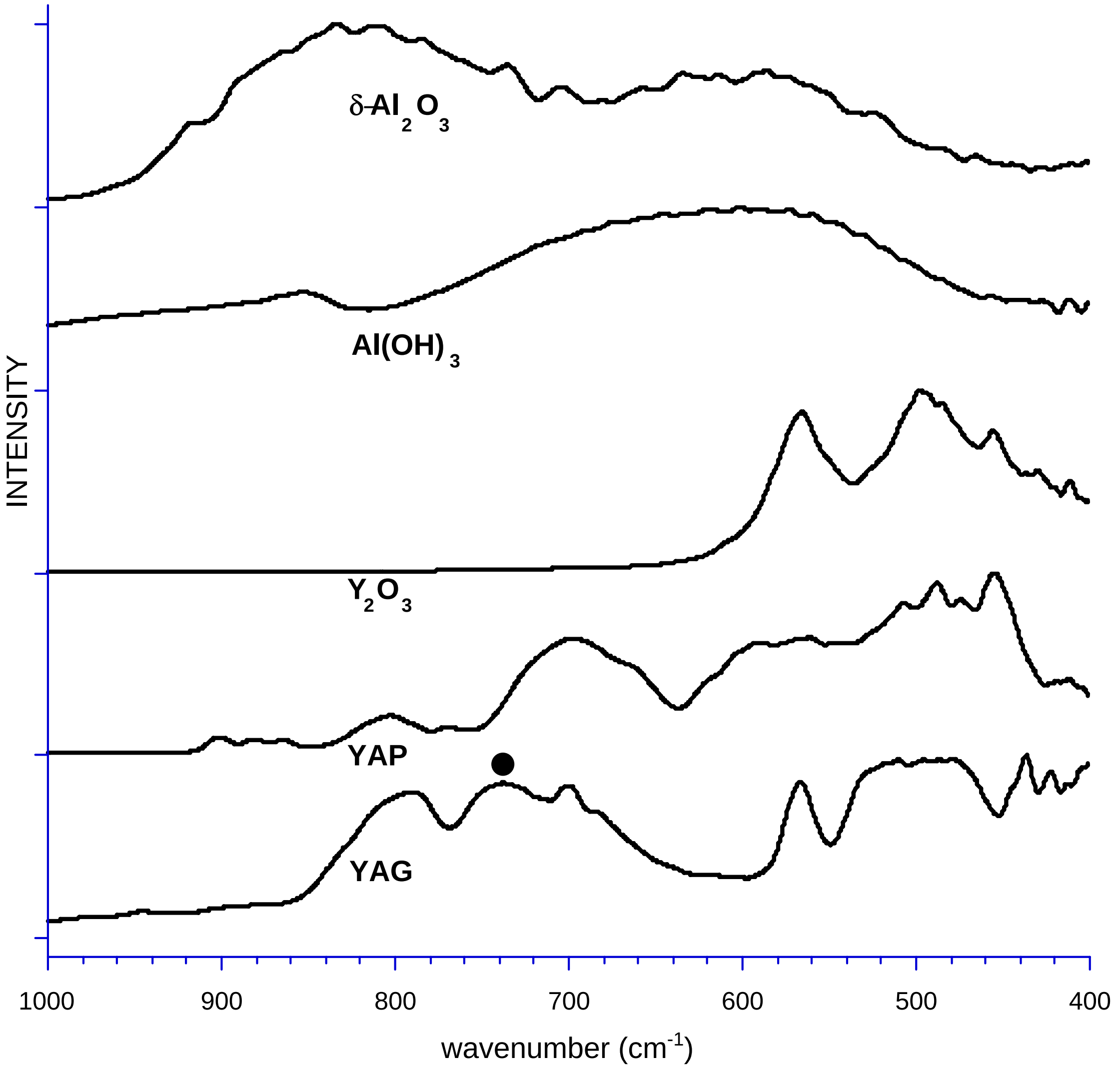

Figure 3.8 FTIR of reference samples (1000-400 cm^{-1}). Black dot indicates ν-Al-O combinatorial vibrations.

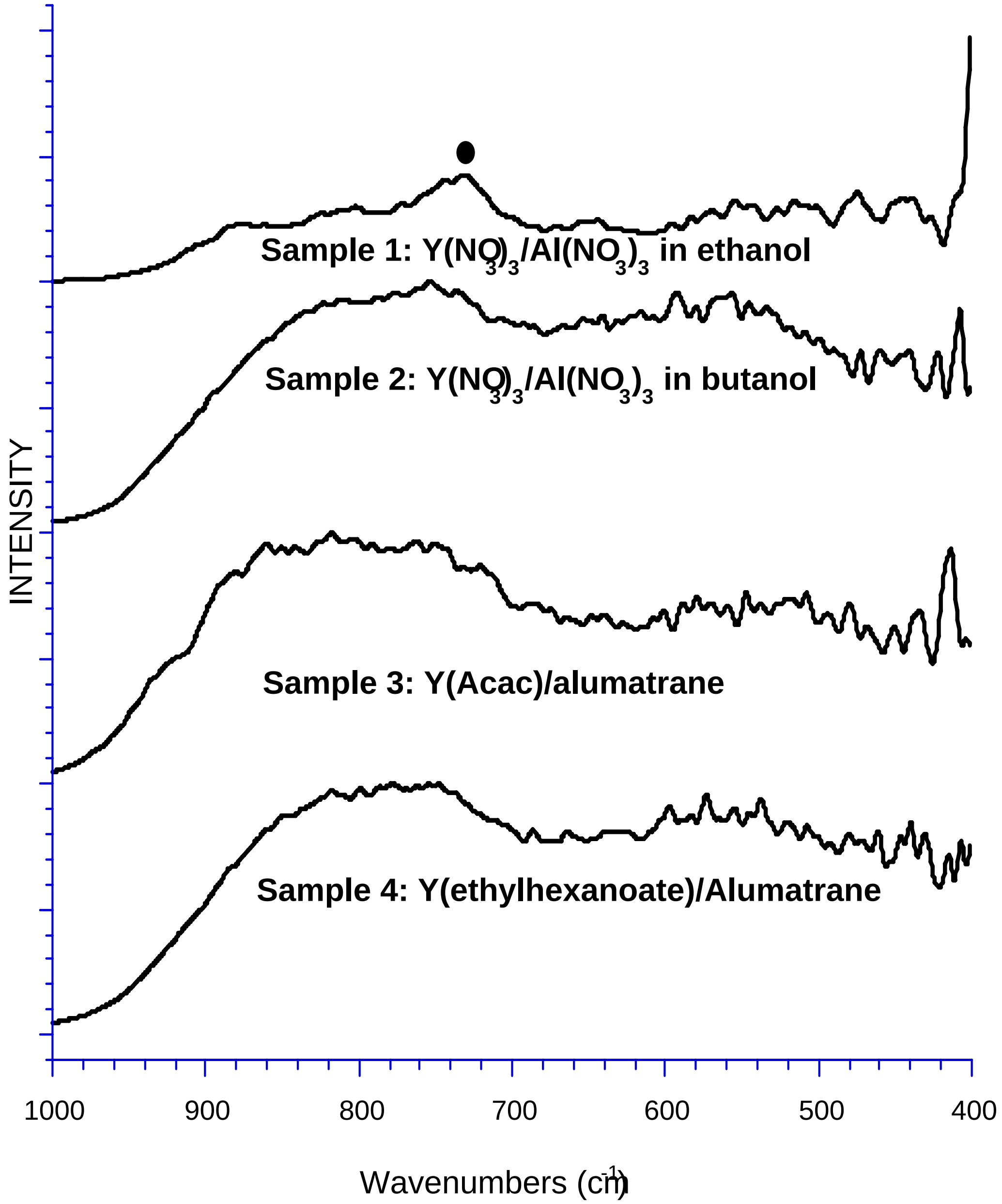

Figure 3.9 FTIR or various samples (1000-400 cm^{-1}). Black dot indicates ν-Al-O combinatorial vibrations.

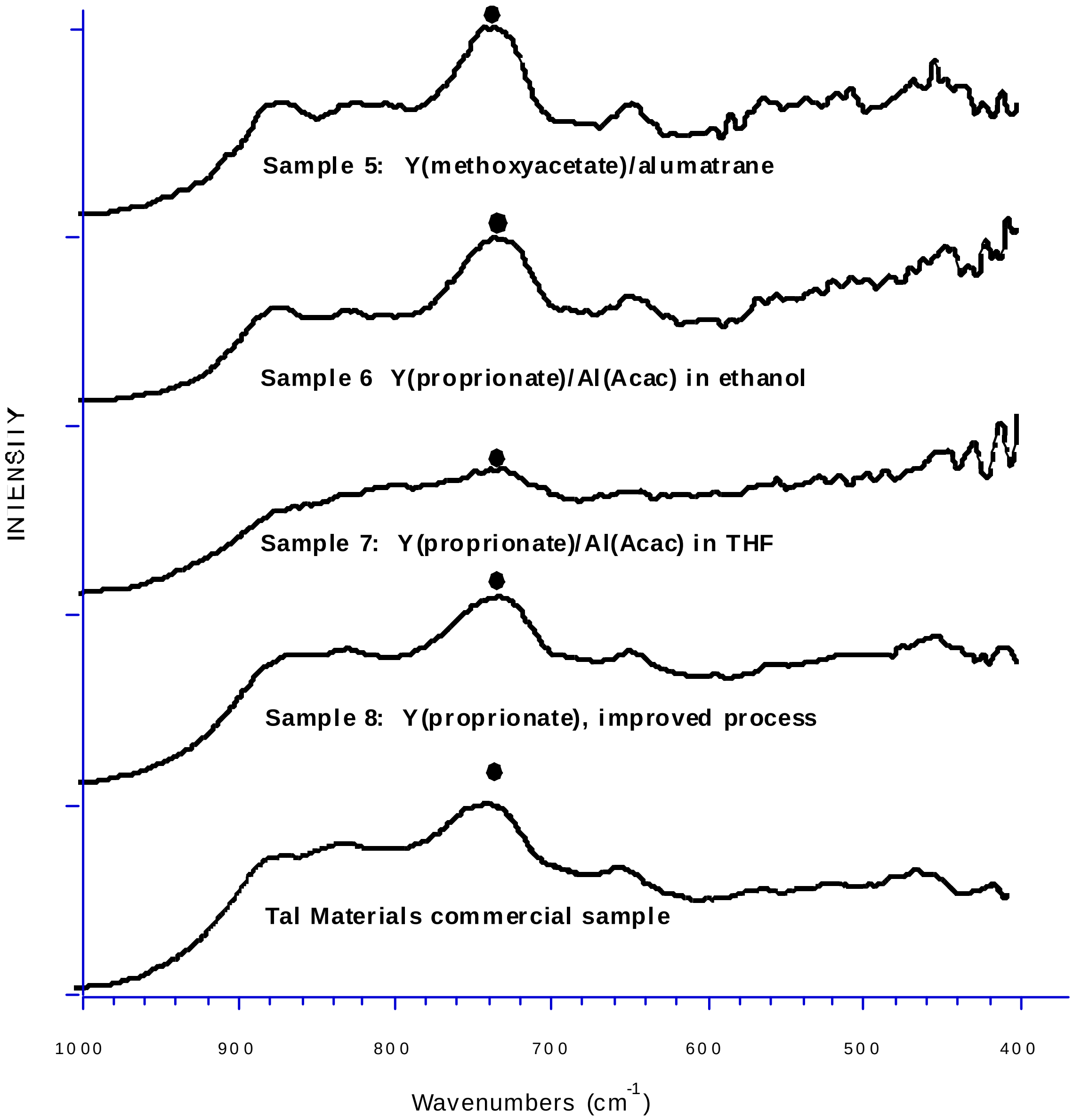

Figure 3.10 FTIR of various samples (1000-400 cm^{-1}). Black dot indicates ν-Al-O combinatorial vibrations.

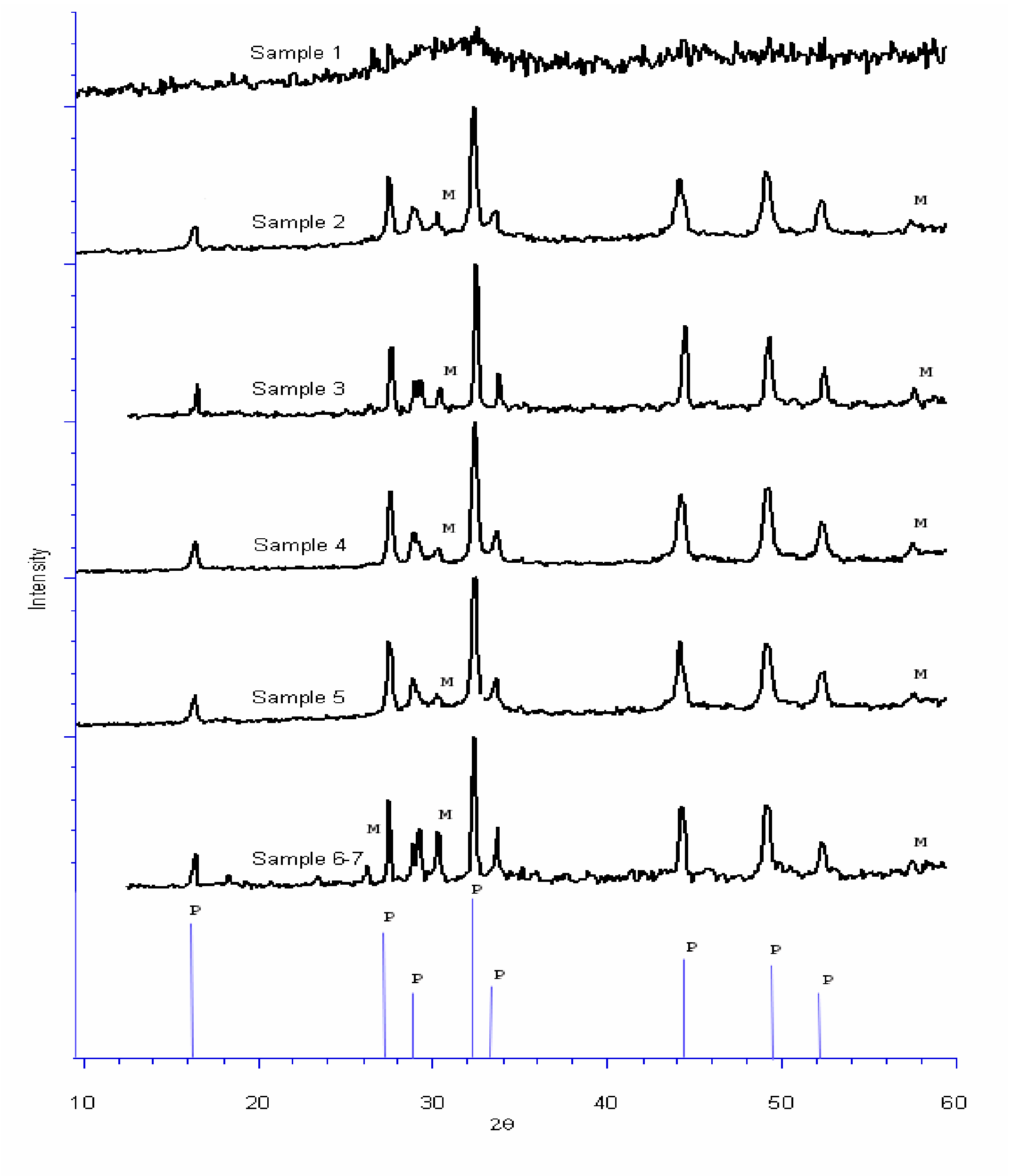

Figure 3.11 XRD of the as-collected powders, M = $Y_4Al_2O_9$ (PDF File No. 34-0368) and P = $YAlO_3$ (I) phase (PDF File No. 74-1334).

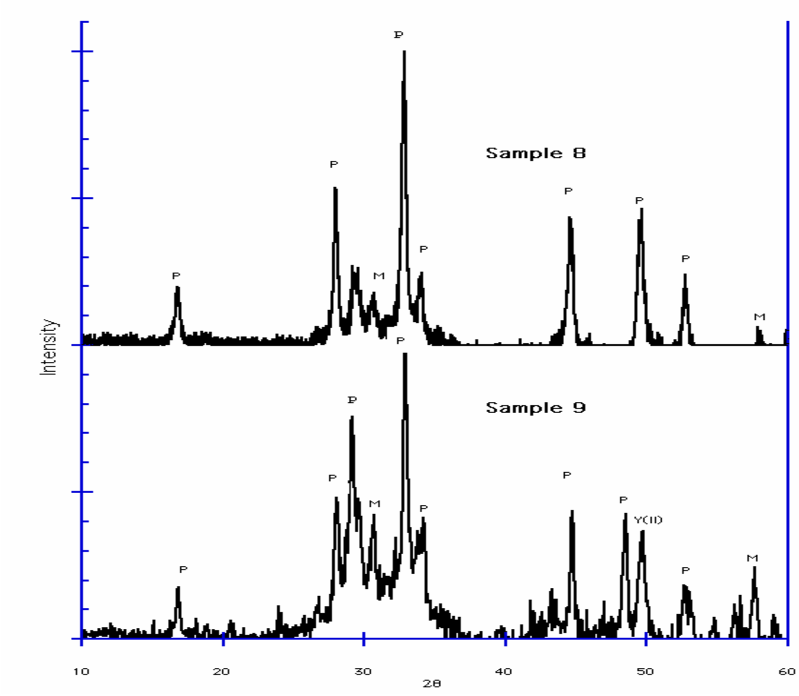

Figure 3.12 XRD of the as-collected powders, M = $Y_4Al_2O_9$ (PDF File No. 34-0368) and P = $YAlO_3$ (I) phase (PDF File No. 74-1334), Y (II) corresponds to tetragonal yttroalumnite (II) (PDF File No. 09-0310).

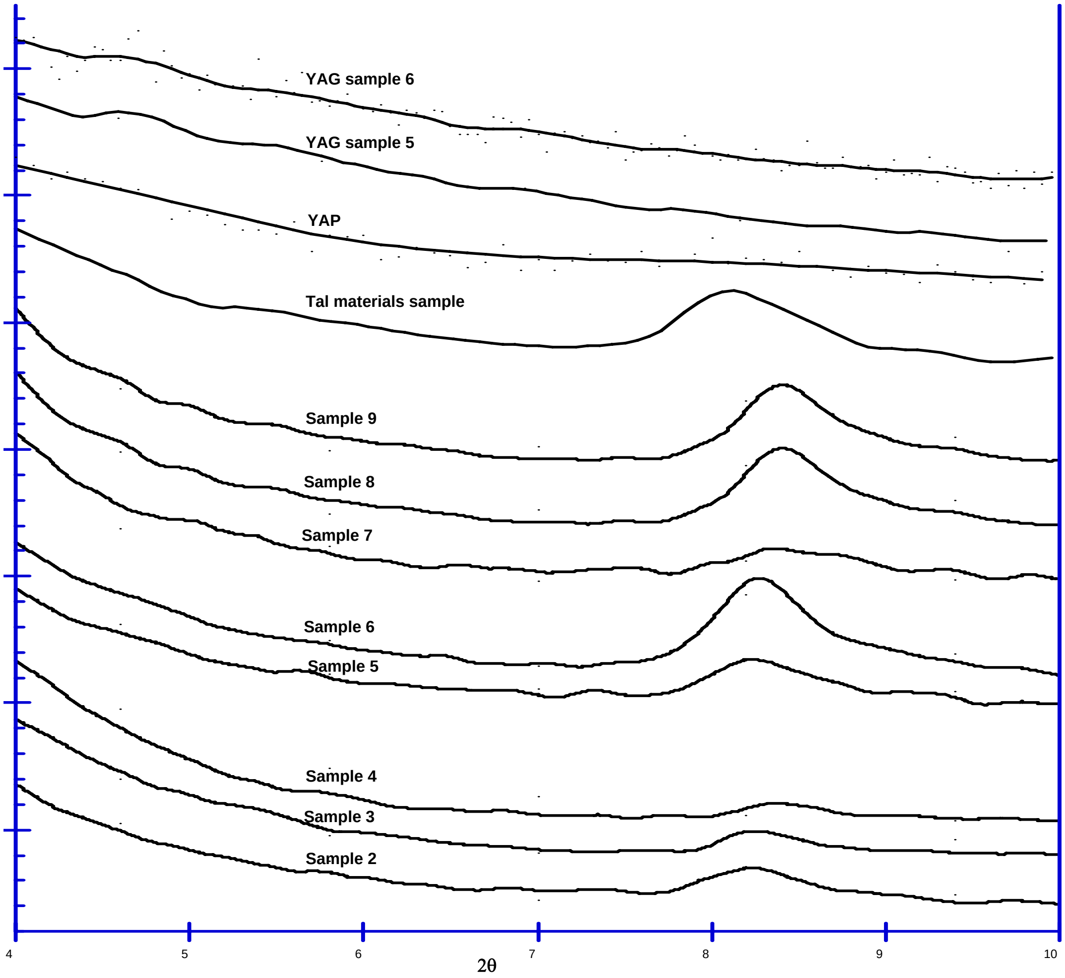

Figure 3.13 Low angle XRD of the as-collected powders.

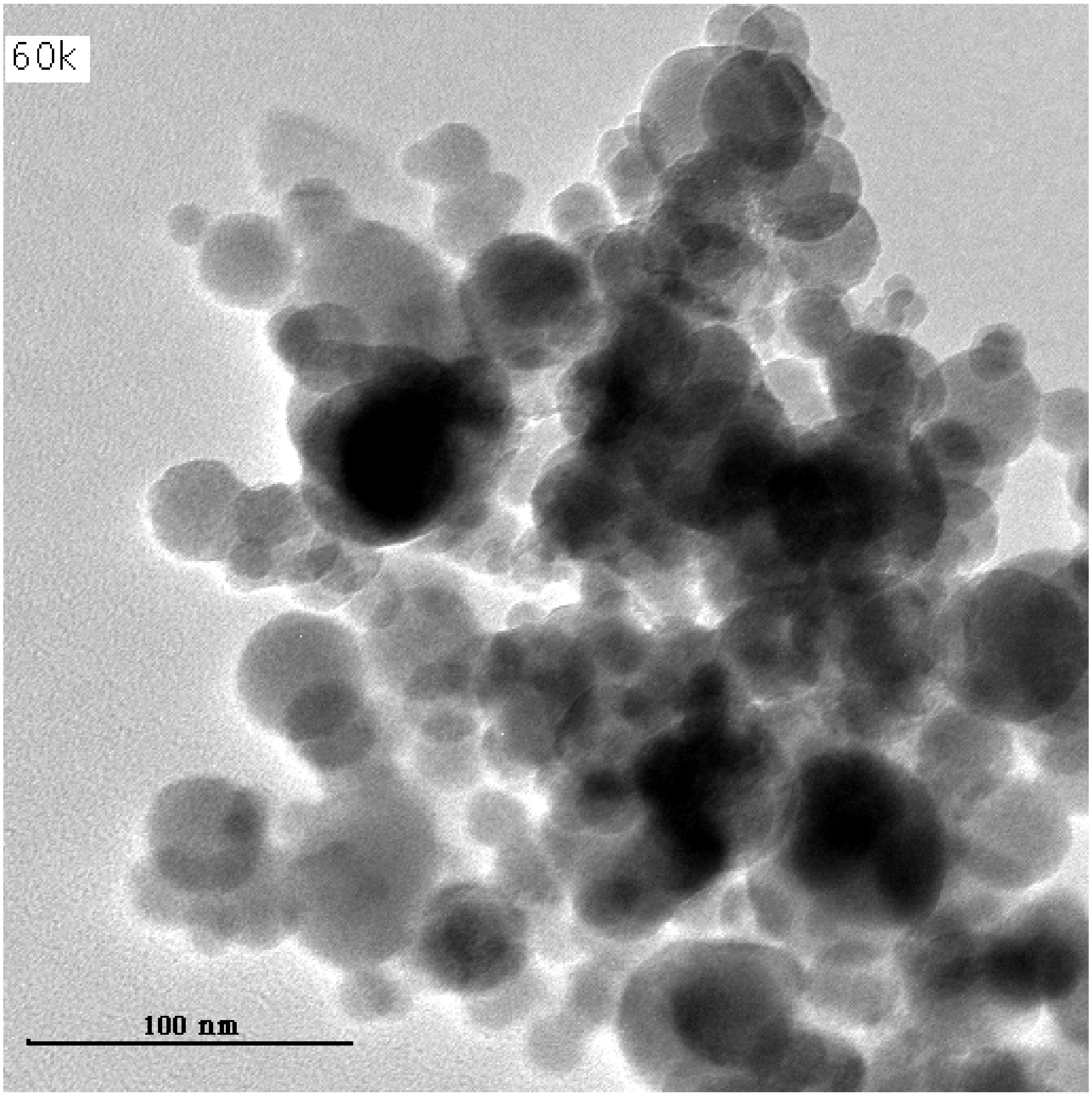

Figure 3.14 TEM of Sample 6 (yttrium propionate/aluminum acetylacetonate), APS ≈ 18 nm.

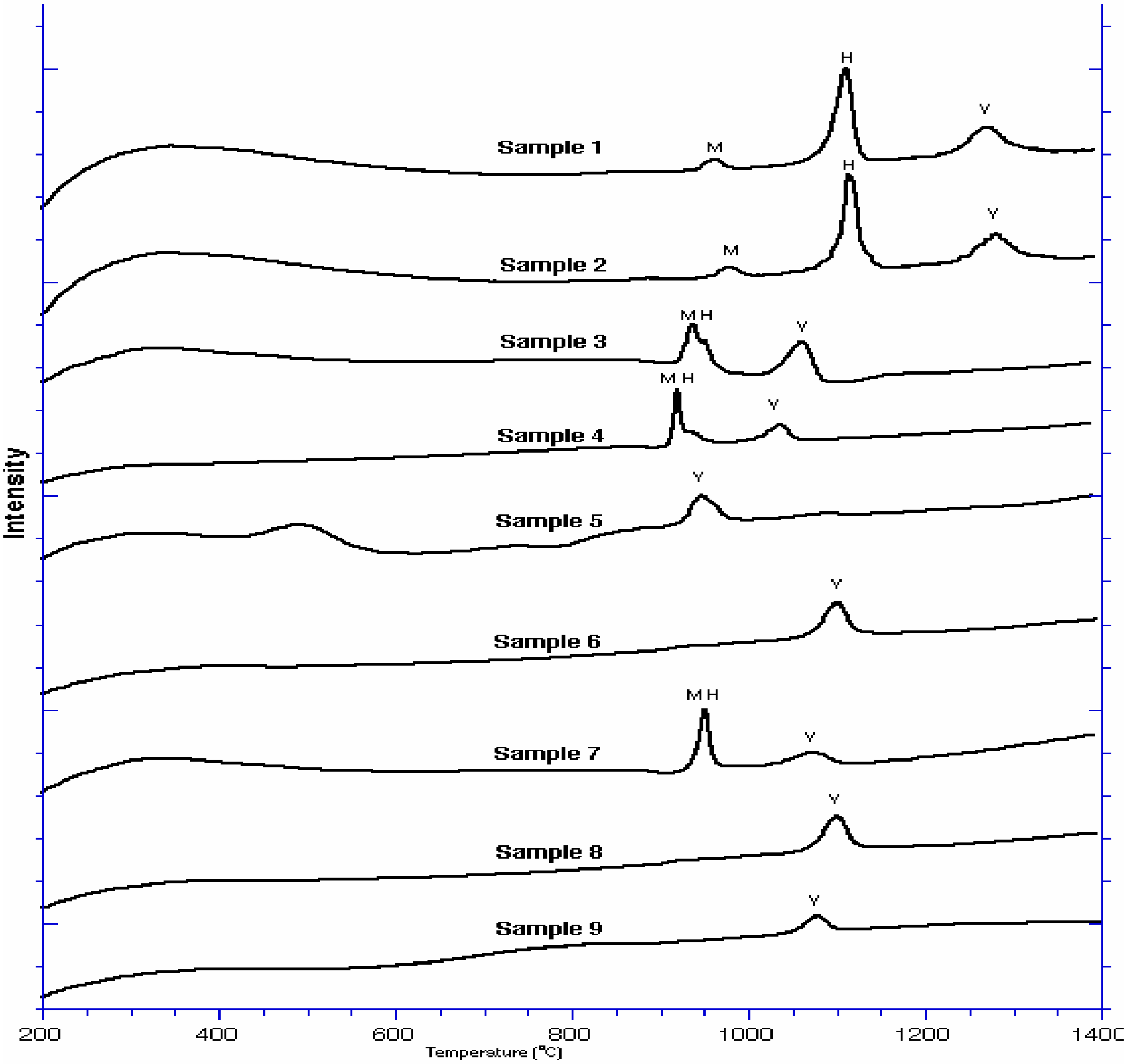

Figure 3.15 DTA of various Samples (M/H/Y: Exotherm attributed respectively to the formation/development of the $Y_4Al_2O_9$/$YAlO_3$/YAG phase).

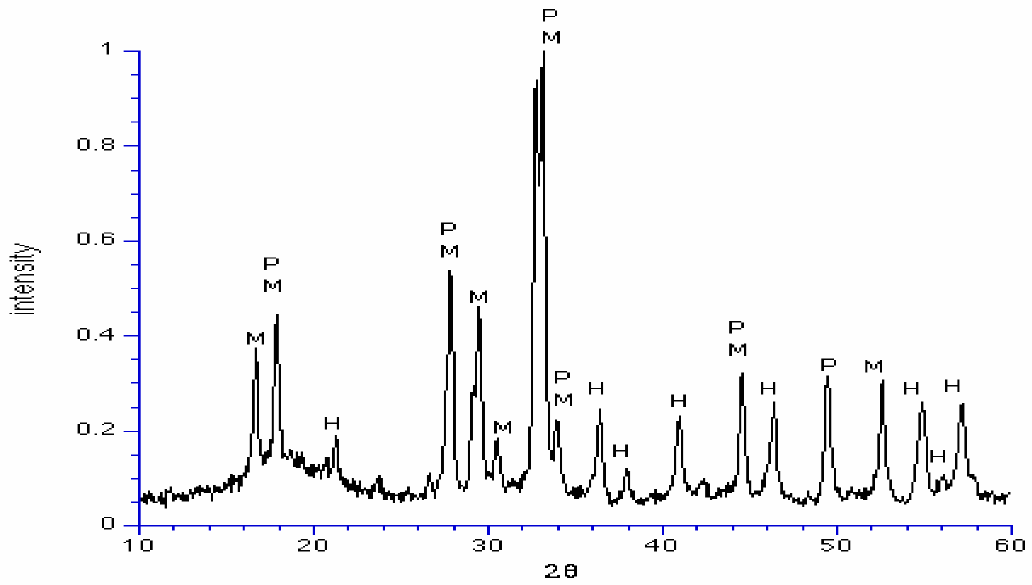

Figure 3.16 XRD of Sample 2 showing the formation of the $YAlO_3$ (II) phase on heating to 1050°C/10°C/min and then cooling at the same rate. M = $Y_4Al_2O_9$, H = $YAlO_3$ (II) and P = $YAlO_3$ (I) phase.

3.5 References

[1]B.R. Johnson, W.M. Kriven, “Crystallization kinetics of yttrium aluminum garnet”, *J. Mater. Res*., **2001** 16 1795.

[2]Y.C. Kang, I.W. Lenggoro, S.B. Park, K. Okuyama, “YAG : Ce phosphor particles prepared by ultrasonic spray pyrolysis”, *Mater. Res. Bulletin*, **2000** *35* 789.

[3]J. McKittrick, B. Hoghooghi, W. Dubbelday, K. Kavanagh, K Kinsman, L. Shea, E. Sluzky, “Size effect in YAG-Cr phospors”, *MRS Symp. Proc.,* **1994** 348 519.

[4]P.R. Rao, “Synthesis of fine grain YAG:RE^{3+} phosphors for low-voltage display devices”, *Proc. SPIE*, **1996** *2651* 139.

[5]Y.C. Kang, I.W. Lenggoro, S.B. Park, K. Okuyama, “Photoluminescence characteristics of YAG : Tb phosphor particles with spherical morphology and non-aggregation”, *J. Phys. Chem. Sol.*, **1999** 60 1855.

[6] O. Katsutoshi, T. Kusunoki, “The effect of ultrafine pigment color filters on cathode ray tube brightness, contrast, and color purity”, *J. Electrochem. Soc.* ,**1996** *143* 1063.

[7] Y. Peizhi, D. Peizhen, Y. Zhiwen, T. Yulian, ”The growth defects in Czochralski-grown Yb : YAG crystal”, *J. Crystal Growth*, **2000** *218* 87.

[8]R.C. Pullar, M.D. Taylor, A.K. Bhattacharya, ”The sintering behaviour, mechanical properties and creep resistance of aligned polycrystalline yttrium aluminium garnet (YAG) fibres, produced from an aqueous sol-gel precursor”, *J. Eur. Ceram. Soc.,* **1999** *19* 1747.

[9]A. Ikesue, T. Kinoshita, K. Kamata, K. Yoshida, “Fabrication and Optical Properties of High-Performance Polycrystalline Nd:YAG Ceramics for Solid-State Lasers”, *J. Am. Ceram. Soc*., **1995** 78 (4) 1033.

[10]R.M. Laine, T. Hinklin, G. Williams, S.C Rand, “Low-cost nanopowders for phosphor and laser applications by flame spray pyrolysis”, *Metastable Mech. Alloyed Nano Mater.*, 2000 (1-2) 500.

[11]P.W. Anderson, ”The question of classical localization” *Phil. Mag*., **1985** *52* 505.

[12]D. Wiersma, A. Lagendijk, ” Interference effects in multiple-light scattering with gain”, *Phys. A,* **1997** *241* 82.

[13]T. Hinklin, B. Toury, C. Gervais, F. Babonneau, J.J. Gislason, R.W. Morton, R.M. Laine "Liquid-Feed Flame Spray Pyrolytic Synthesis of Nanoalumina Powders", *Chem. Mater.*, **2004** 16 (1) 21.

[14]C. Shihui, H. Sentiong, C Hui, "Design of gain clamped erbium doped fiber amplifiers", *LEOS'99,* **1999** *2* 417.

[15]J. Li, T. Ikegami, J. Lee, T. Mori, Y. Yajima, " Co-precipitation synthesis and sintering of YAG powders: the effect of precipitant", *J. Eur. Ceram. Soc.*, **2000** *20* 2395.

[16]K.T. Pillai, R.V. Kamat, V.N. Vaidya, D.D. Sood, "Synthesis of yttrium aluminium garnet by the gel entrapment technique using hexamine", *Mater. Chem. Phys.*, **1996**, *46* 67.

[17]Y.C. Kang, Y.S. Chung, P.S. Bin, "Preparation of YAG : Europium red phosphors by spray pyrolysis using a filter-expansion aerosol generator", *J. Am. Ceram. Soc.,* **1999** *82* 2056.

[18]M. Nyman, J. Caruso, M. J. Hamden-Smith, T.T. Kodas, "Comparison of solid-state and spray-pyrolysis synthesis of yttrium aluminate powders", *J. Am. Ceram. Soc.*, **1997** *80* 1231.

[19]D. M. Veith, S. Mathur, A. Kareiva, M. Jilavi, M. Zimmer and V. Huch, "Low temperature synthesis of nanocrystalline YAG and Ce-doped YAG via different sol-gel methods", *J. Mater. Chem.* **1999** *9* 3069.

[20]R. Baranwal, "Synthesis of Nanopowders" Ph.D. Dissertation, University of Michigan **1996.**

[21]R.M. Laine, K. Waldner, C. Bickmore, D. Treadwell, U.S. patent 5,614,596 (March **1997**).

[22]R. Baranwal, M.P. Villar, R. Garcia, R.M. Laine, "Flame spray pyrolysis of precursors as a route to nano-mullite powder: Powder characterization and sintering behavior", *J.Am. Ceram. Soc.*, **2001** *84* 951.

[23]R.M. Laine, R. Baranwal, T. Hinklin, D. Treadwell, A. Sutorik, C.R. Bickmore, K. Waldner, S.S. Neo "Novel Synthetic and Processing Routes to Ceramics", Ed. by Uematsu, H. Otsuka, Eds., Key engineering Materials, K. Trans Tech Publ. Ltd. Switzerland, **1998** 17.

[24] $$\langle Diameter \rangle = \frac{6}{SSA \times \rho}$$

[25] R.M. Laine, K.A. Youngdahl, R.A. Kennish, M.L. Hoppe, Z.F. Zhang, “Superconducting fibers from organometallic precursors. Part II: Chemistry and low temperature processing”, *J. Mater. Res.,* **1991** *6* 895.

[26] S. Jain, D.J. Skamser, T. Kodas, “Morphology of single-component particles produced by spray pyrolysis”, *Aer. Sci. Tech*., **1997** *27* 575 b. R. Mahadevan, D. Lee, H. Sakurai, M.R. Zachariah, “Measurement of condensed-phase reaction kinetics in the aerosol phase using single particle mass spectrometry”, *J. Phys Chem. A*, **2002** *106* 11083 c. L. Madler, S.E. Pratsinis, “Bismuth oxide nanoparticles by flame spray pyrolysis”, *J. Am. Ceram. Soc*. **2002** *85* 1713.

[27] G.T. Carreno, M.P. Morales, C.J. Sena, ”Preparation of uniform γ-Fe_2O_3 particles with nanometer size by spray pyrolysis”, *Mater. Let*., **1993** *18* 151.

[28] S.E. Pratsinis, S. Vemury, “Particle formation in gases: A review”, *Powder Tech.,* **1996** *88* 267.

[29] A.M. George, N.C Mishra, M.S. Nagar, N.C Jayadevan, “Formation of YAG from coprecipitated yttrium aluminium hydroxides”, *J. Therm An.,* **1996** *47* 1701.

[30] S. Le Floch, M. Gervais, F. Gervais, ”Infrared reflectivity study of the metastable solid solution Y_2O_3-Al_2O_3 on both side of the YAG composition”, *Mater. Sci. Eng*., **1995** *B33* 217.

[31] J.B. Peri, “Infrared and gravimetric study of surface hydration of gamma-alumina”, *J. Phys. Chem*., **1965** *69* 211.

[32] J.B. Peri, “A Model for the Surface of γ-Alumina”, *J. Phys. Chem*., **1965** *69* 220.

[33] D.H. Lee, R.A. Condrate, “An FTIR spectral investigation of the structural species found on alumina surfaces”, *Mater. Lett*., **1995** *23* 241.

[34] J.M. Saniger, “Al-O Infrared vibrational frequencies of gamma-alumina”, *Mater. Lett*., **1995** *22* 109.

[35] P. Tarte, “Infra-red spectra of inorganic aluminates and characteristic vibrational frequencies”, *Spectr. Acta,* **1967** *23A* 2127.

[36] A. Gurav, T. Kodas, T. Pluym, Y. Xiong, ”Aerosol processing of materials” *Aer. Sci. Tech*., **1993** *19* 411.

[37]Y. Liu, Z.F. Zhang, B. King, J. Halloran, R.M. Laine, “Synthesis of yttrium aluminum garnet from yttrium and aluminum isobutyrate precursors”, *J. Am. Ceram. Soc*., **1996** *79* 385.

[38]O. Yamaguchi, K. Takeoka, A. Hayashida, “Formation of alkoxy-derived $Y_3Al_5O_{12}$”,*J. Mater. Sci. Lett*., **1991** *10* 101.

[39]C.D. Veitch, “Synthesis of polycrystalline yttrium-iron garnet and yttrium-aluminum garnet from organic precursors”, *J. Mater. Sci*., **1991** *26* 6527.

[40]N.J. Hess, G.D. Maupin, L.A. Chick, D.S. Sunberg, D.E. McCreedy and T. R. Armstrong, “Synthesis and crystallization of yttrium-aluminum garnet and related compounds”, *J. Mater. Sci.,* **1994** *29* 1873.

[41]A.S. Pell, G. Pilcher, “Measurement of heat of combustion by calorimetry”, *Trans. Faraday Soc*. **1965** *61* 71.

[42]F.D. Rossini, *J. Res. NBS*, “The heat of formation of hydrogen chloride and some related thermodynamic data”, **193** *8* 119.

[43]J. Marchal, R.M Laine, H. Sun, X Pan, “A new $Y_3Al_5O_{12}$ phase produced by liquid-feed flame spray pyrolysis (LF-FSP)”, *Adv Mater*., **2005** 17 830.

Chapter 4: A new $Y_3Al_5O_{12}$ phase produced by liquid-feed flame spray pyrolysis (LF-FSP)

4.1 Introduction

Yttrium aluminum garnet, YAG ($Y_3Al_5O_{12}$) materials have been studied extensively over many decades because of their exceptional high temperature mechanical strength coupled with low creep, utility as phosphors, scintillators and most importantly for their photonic properties.[1-6] Single crystal YAG dominates commercial solid-state laser markets while also offering aesthetic beauty as YAG jewelry.

Laser applications have provided the impetus for in-depth examinations of the properties and processing of $Y_3Al_5O_{12}$ composition melts, glasses and single-phase materials.[6-10] The recent advent of transparent polycrystalline YAG lasers that outperform single crystal YAG lasers has intensified interest in the development of very fine YAG particles that are easily sintered to full density and transparency.[11,12] In chapter 3 we produced nanosized $Y_3Al_5O_{12}$ powders for this purpose that result in a new phase.

LF-FSP allows the synthesis of nanopowders with average particle diameters < 20 nm (≈ 90 m^2/g) with the $Y_3Al_5O_{12}$ composition. Characterization of these powders by FTIR, XRD, TGA-DTA, TEM and powder pattern modeling studies suggest the formation of a new hexagonal phase with the $Y_3Al_5O_{12}$ composition with unit cell parameters of a = 0.736 nm and c = 1.052 nm and a density of 5.5 g/cc vs 4.5 for the YAG phase. Hexagonal $Y_3Al_5O_{12}$ nanopowder is easily formed into green bodies with densities that are 62-64 wt % of theory. Those green bodies sinter to the YAG phase and higher than 99.5% density at 1400°C/2 h with grain sizes < 500 nm, using sintering conditions that involve an intermediate heating step in vacuum at 1000°C. This novel material offers potential for making high quality YAG materials including ceramic lasers with exceptional control of processing parameters.

4.2 Experimental

4.2.1 Pellets formation

Powder dispersed as described in chapter 3, were re-dispersed (5 grams of powder in 500 mL of ethanol) with an ultrasonic horn in ethanol with 2 wt/% PEO/PVA binders. The suspension was then dried at 80°C in a drying oven for 48h. The resulting powder was then hand ground in an alumina mortar and sieved with a polymer 400 mesh. Compacts were formed by loading 1.00 ± 0.10 g of powders into a tungsten carbide double-action die (diameter of 12.75 mm) and pressing in a laboratory press (model 3912, Carver). Powder were compacted between 40 and 260 MPa for ≈ 10 minute, we found that 120 MPa gave the best mechanical properties to the green bodies and further experiments were done with pellets processed at this pressure. Then the pellets were cold isostatically pressed.

4.2.2 Cold Isostatic pressing

Pellets were placed in Food Saver bags and evacuated using a Food Saver 400 (Jarden, NY) which automatically sealed the evacuated bags under vacuum. The bags were pressed in an Autoclave Engineers (Erie, PA) cold isostatic press. The bags were pressed at 300 MPa, with a ramp of 5 MPa/min and held for 30 min and released at 5 MPa/min. The dimensions, measured by digital micrometer, and mass of the compact were used to calculate the green densities.

4.3 Results

4.3.1 Analysis

In Chapter three, we found that 3:5 mixtures of $Y(O_2CCH_2CH_3)_2OH$ and $Al(Acac)_3$ dissolved in EtOH gave nanopowders with average particle sizes (APS) below 50 nm (Figure **4.1a**). The as-produced particles are unnecked, easily dispersed and single crystals as determined by high resolution TEM (Figure **4.1b**).

In contrast to what was anticipated, the digital diffraction and XRD powder patterns for the

as-produced powders do not match those of YAG as described in Chapter 3. As shown in Figure **4.2**, the XRD most closely resembles that of the hexagonal phase of $YAlO_3$. Since this is a commonly observed kinetic phase in this system, this finding was not too surprising. However, if we had produced $YAlO_3$ then the overall stoichiometry of the system would be $3YAlO_3 \cdot Al_2O_3$. The excess alumina (25 mol %) would be expected to be visible either as a crystalline phase (not observed), an amorphous phase with an amorphous hump in the XRD powder patterns (not observed), or last and least likely, present in defect structures.

On careful examination, the XRD peak intensities obtained differ from those expected for $YAlO_3$. This prompted examination of the low angle XRD pattern shown in chapter three, revealing a peak at 8.3-8.5°2θ corresponding to a lattice parameter of ≈ 1.1 nm, close to the unit cell dimensions for crystalline YAG and to the (001) interplanar distance of hexagonal $YAlO_3$. However neither true YAG samples (obtained after annealing at $1200^{\circ}C$/30 min), nor authentic samples of LF-FSP nano hexagonal $YAlO_3$ show this peak (due respectively to the structure factor of YAG and the equivalency of $YAlO_3$ (002) and (001) planes).

FTIR studies also suggest a novel material. The $Y_3Al_5O_3$ composition powders contain small but typical νO-H and carbonate νC-O bands in the 3400-3600 cm^{-1} and 1400-1600 cm^{-1} regions, respectively. Both result from the high water and CO_2 environment in the flames. Likewise peaks for νAl-O and νY-O are those common to most of the materials in the Y_2O_3-Al_2O_3 system. However, one peak at 740 cm^{-1} is unique to the new material. This peak is usually assigned to asymmetric νAl-O in <u>isolated</u> AlO_4 tetrahedra as in the YAG phase. Alternately, it is observed for specific interactive vibrations between AlO_4 or AlO_5 species bound to AlO_6 octahedra as discussed by Saniger[14] and Tarte.[15] Restated, this band appears when at least one $AlO_{4,5}$ species forms Al-O-Al (Y) bonds to a second AlO_6 or YO_6 species. As such, this peak is not observed in δ-alumina, $Al(OH)_3$, or in hexagonal $YAlO_3$.

In the Y_2O_3-Al_2O_3 system, this peak might be expected if excess Al^{3+} (Y:Al ratio <1) substitutes for Y^{3+} in the hexagonal $YAlO_3$ phase resulting in AlO_6 octahedra connected to $AlO_{4,5}$ species forming a regular defect structure.

Random substitution of Y^{3+} by Al^{3+} would not show either the 740 cm^{-1} FTIR peak or the differences in the XRD pattern. Furthermore, the XRD powder pattern reported above can be closely simulated (Figure **4.2**) in terms of peak positions and intensities suggesting a regular atomic ordering of atoms and therefore a new phase in the $Y_3Al_5O_{12}$ composition.

The simulation also allows us to suggest a structure for the new phase that is hexagonal, a = 0.736 nm and c = 1.052 nm. This unit cell resembles hexagonal $YAlO_3$

but is 4 times bigger and has a regular defect structure in the (002) plane: half of the Y^{3+} are substituted by Al^{3+} forming a regular pattern. The structure is best described layer by layer (all parallel to the 001 plane): Layer a: hexagonal layer of yttrium ions, layer b: hexagonal layer of oxygen ions, layer c: hexagonal layer of alternating five coordinate Al^{3+} and O^{2-} ions, layer d: hexagonal layer of alternating octahedral Y^{3+} and octahedral Al^{3+} ions. Thus, the unit cell consists of an ABCBDBCBA arrangement contrasting with the ABCBABCBA layers of hexagonal $YAlO_3$. This causes the extra 8.4° 2θ peak in the low angle XRD. These unit cell dimensions indicate that the density of this material is 5.52 vs 4.51 for YAG. A model of the lattice cell is shown in Figure **4.3**.

The literature on YAG glasses[8,9] suggests that there are actually two glass phases, one having a lower density than the other and being the thermodynamically most stable of the two. It is tempting to argue that LF-FSP produces hexagonal $Y_3Al_5O_{12}$ by gas phase formation of the higher density of these two glasses followed by crystallization. However, the structure of these materials is dominated by a tetrahedral alumina framework, which differs from that observed here where it appears that the only Al^{3+} ions present are penta- or hexa-coordinated. As YAG glasses form with all three Al^{3+} ion types, a different crystallization route seems more probable.

The E_a for conversion to the YAG phase was determined in Chapter 3 to be ≈ 110 kJ/mol,[13] much lower than the 550 kJ/mol[16] reported for conversion from $YAlO_3$ and Al_2O_3 to YAG. Hence, there appears to be a very strong driving force for formation of the YAG phase. This driving force when coupled with the roughly 20% higher density of the hexagonal phase should provide improved sintering as conversion to the lower density

YAG phase may aid in removing porosity during the sintering process. This prompted the following sintering studies.

4.3.2 Sintering studies

We cleaned the powders as described in Chapter 2 and added binders as described in the experimental section. We then formed several green bodies by regular pressing at 120 MPa, followed by CIPing at 300 MPa, as described in the experimental section (green density of 62-64%). The pellets were then heated at 800°C (heating rate of 5°C/min, 2 hours dwell) under pure oxygen (flow of 60mL/min) to remove the binders. The resulting pellets were then annealed under vacuum at 1000°C (heating rate of 10°C/min, 2 hours dwell) to homogenize the pellet phase and the pore size as discussed in Chapter 1.

Several sets of pellets prepared identically were sintered in a vacuum furnace using heating rate from 5 to 20°C and dwelling temperature of 1375-1425°C. The highest final density was obtained with pellets sintered at 1400°C (10°C/min to 800°C for 2 hours, vacuum 10°C/min to 1000°C for 2 h, followed by 10°C/min to 1400°C, 8 h), which were 97^{+}% dense (as determined with an Archimedes balance) while maintaining grain sizes of < 500 nm as can be seen in Figure **4.4**

4.4 Conclusions

The LF-FSP process allows the synthesis of a new hexagonal $Y_3Al_5O_{12}$ phase characterized using FTIR, XRD, TGA-DTA and TEM. This phase is only present as a high surface area (70-90 m^2/g) nanopowder and consists of spherical, easily dispersed, nanoparticles. This new phase can be processed in high density green bodies through typical wet processing. While the nanopowder converts to YAG nanopowder with low activation energy as described in chapter 3, green bodies of the new phases can be sintered to essentially full density YAG monoliths at 1400°C while keeping grain size below 500 nm.

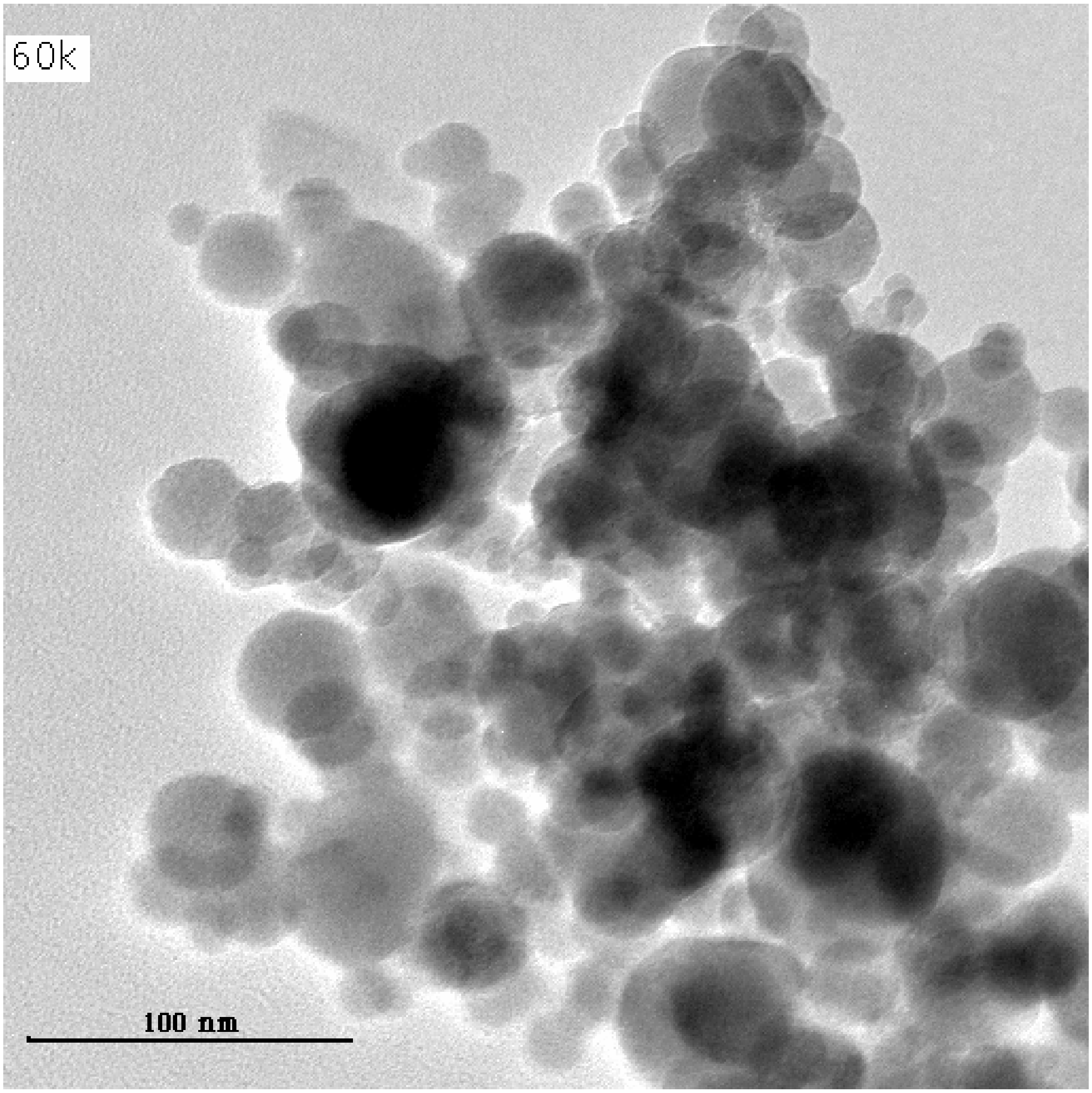

Figure 4.1 a. TEM of LF-FSP produced $Y_3Al_5O_{12}$ composition nanopowders (Sample 6 described in chapter 3, APS 20-50 by XRD line broadening, BET surface area analysis, 40-90 m^2/g).

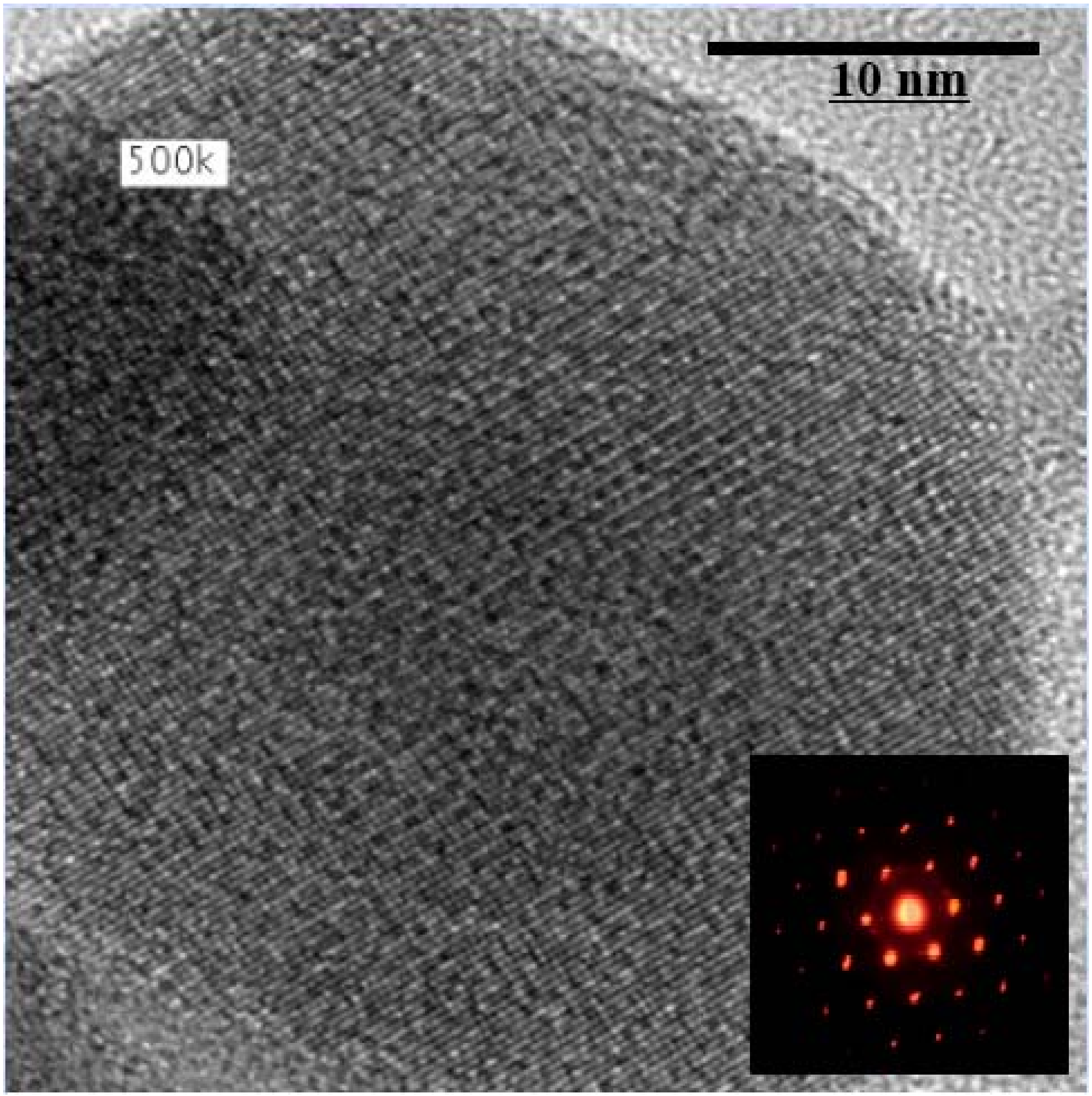

Figure 4.1 b. HTREM of single particle (Sample 6, described in Chapter 3), digital diffraction pattern inset.

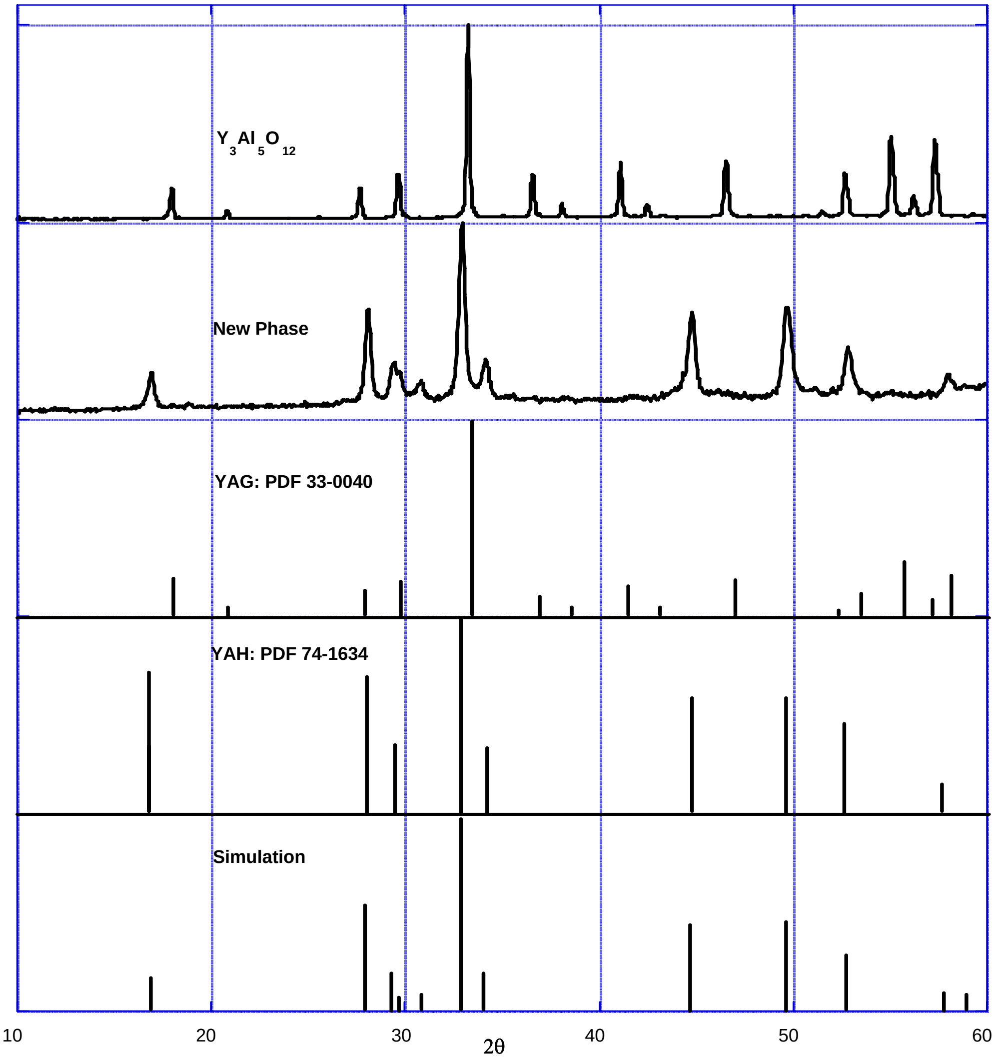

Figure 4.2. XRD patterns of **a.** YAG from annealed powder, **b.** new phase, low angle peak at 8.2°2θ not shown, **c**. YAG ICDD 33-0040, **d**. Hexagonal $YAlO_3$ ICDD 74-1634 and d. Simulation of XRD powder pattern of new phase

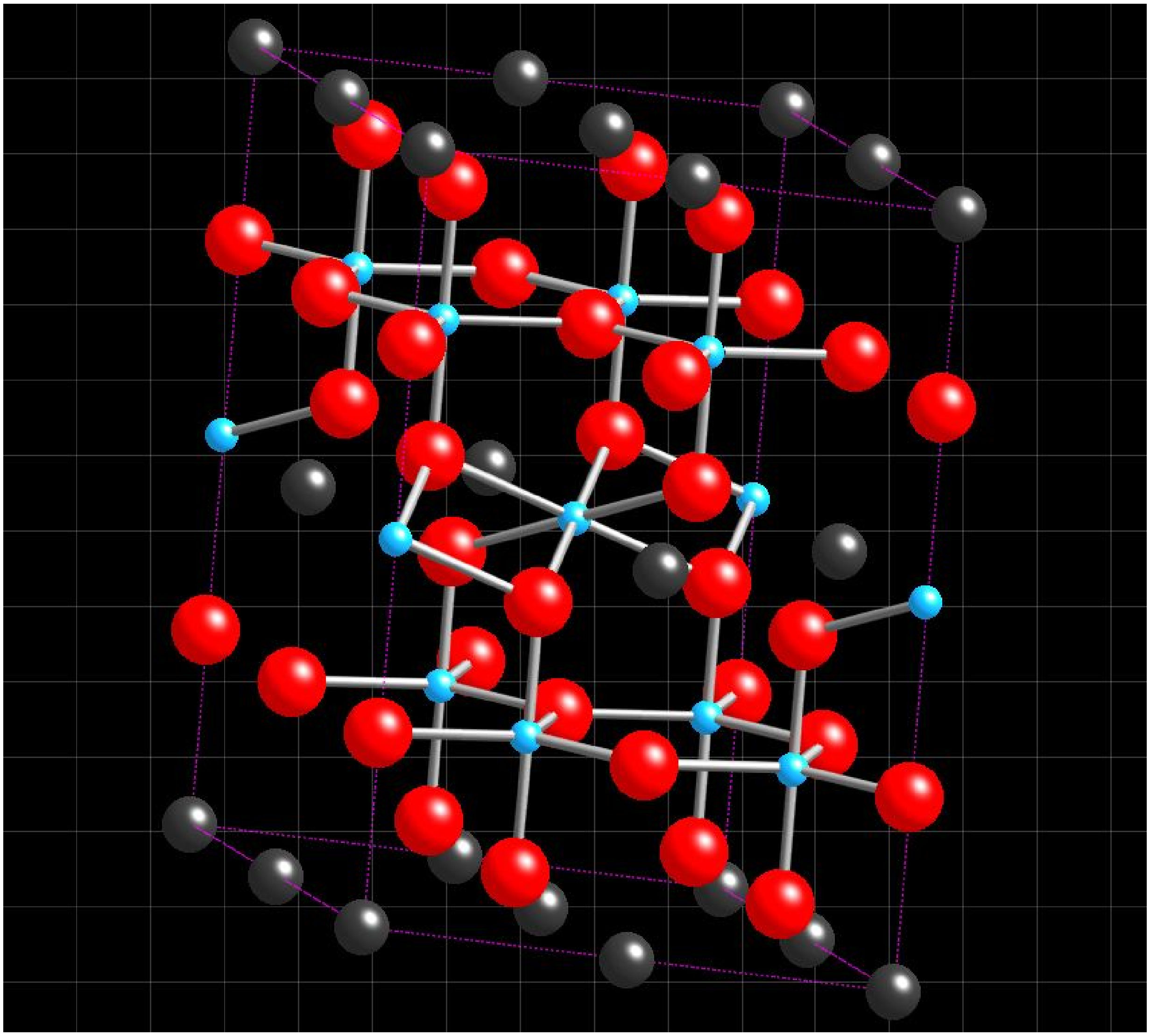

Figure 4.3 Model of the new hexagonal $Y_3Al_5O_{12}$ phase.

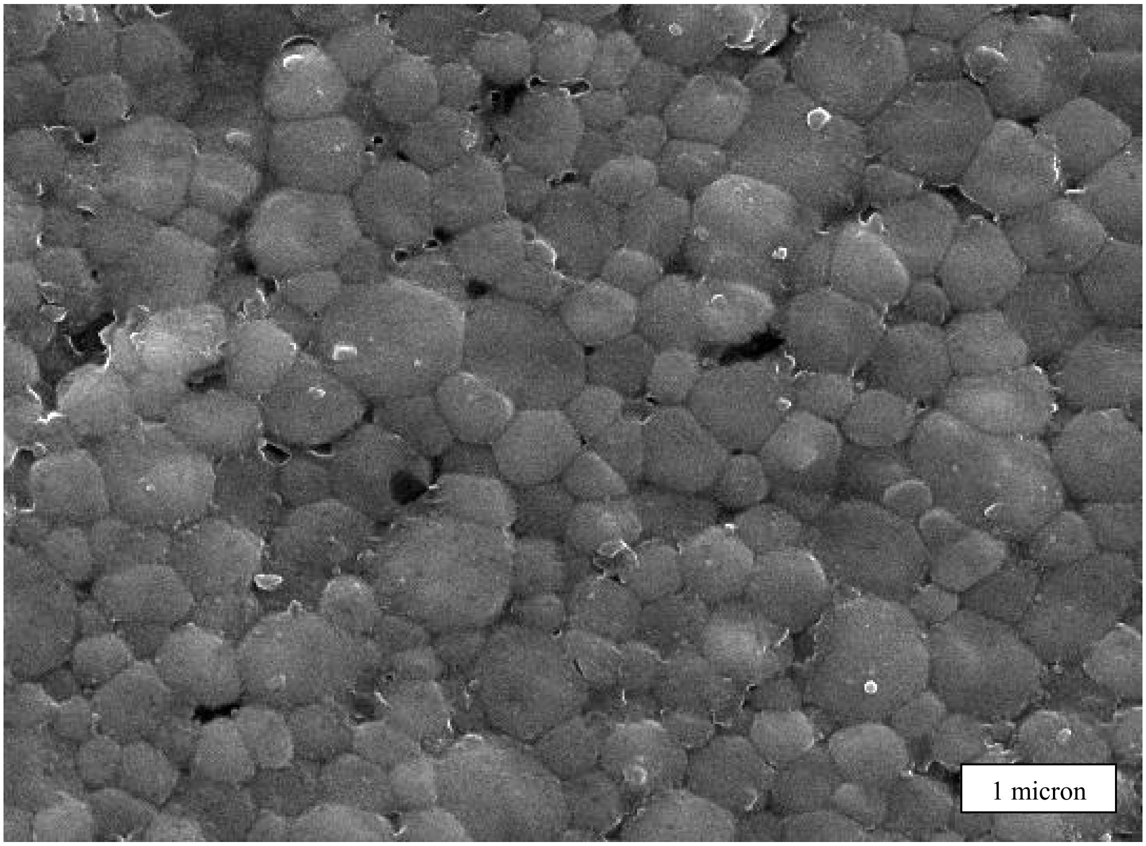

Figure 4.4 SEM of a pellet (sintered at 1400°C for 8 h, heated rate of 10°C/min with a 2 h step at 1000°C) fractured surface after additional thermal etching at 1200°C.

4.5 References

[1]W.R., Blumenthal; D.S. Phillips, "High-Temperature Deformation of Single-Crystal Yttrium-Aluminum Garnet (YAG)", *J. Am. Ceram. Soc.*, **1996** *79* 1047.

[2]S., Karato; Z .,Wang; K., Fujino, "High-temperature creep of yttrium-aluminium garnet single crystals", *J. Mat. Scie.*, **1994** *29* 6458.

[3]Y., Pan; Y., Sun; M.,Wu; Q., Su," Effect of pre-aging pH on the formation of yttrium aluminum garnet powder (YAG) via the solid state reaction method", *J. Phys. Chem. Sol.,* **2004** *65* 845.

[4]Y.H., Zhou; J., Lin; M., Yu; S.M., Han; S.B., Wang; H.J., Zhang," Morphology control and luminescent property of $Y_3Al_5O_{12}$:Tb particles prepared by spray pyrolysis", *Mater. Res. Bul.,* **2003** *38* 1289.

[5]J. McKittrick; L.E. Sheab; C.F. Bacalskia; E.J., Boszea, "The influence of processing parameters on luminescent oxides produced by combustion synthesis", *Displays*, **1999** *19* 169.

[6]V. Babin, A. Krasnikov, Y. Maksimov, K. Nejezchleb, M. Nikl, T. Savikhina and S. Zazubovich, "Luminescence of Pr^{3+}-doped garnet single crystals", *Opt. Mater.,* **2007** *30* 30.

[7]K. Nagashio; K. Kuribayashi, "Rapid solidification of $Y_3Al_5O_{12}$ garnet from hypercooled melt", *Acta Materiala,* **2001** *49* 1947.

[8]P. Yang; P. Deng; Z. Yin,; Y. Tian, "The growth defects in Czochralski-grown Yb : YAG crystal", *J. Crys. Growth*, **2000** *218* 87.

[9]M.C. Wilding; P.F. McMillan; A. Navrotsky, "Calorimetric study of glasses and liquids in the polyamorphic system Y_2O_3-Al_2O_3", *Phys. Chem. Glasses*, **2002** *43* 306.

[10]M.C. Wilding, P.F. McMillan, A. Navrotsky, “Thermodynamic assessment of the MgO–Al_2O_3–SiO_2 system”, *Physica A,* **2002** *314* 379.

[11]J. Zhang; J. Ning; X. Liu; Y. Pan; L. Huang, “Low-temperature synthesis of single-phase nanocrystalline YAG:Eu phosphor”, *J. Mater. Sci. Lett.*, **2003** *22* 13.

[12]A. Ikesue; K. Yoshida; K. Kamata, “Transparent Cr^{4+}-doped YAG ceramics for tunable lasers”, *J. Am. Ceram. Soc.*, **1996** *79* 507.

[13]J. Lu, M. Prabhu, J. Song, C. Li, J. Xu, K.I. Ueda, H., Yagi, T. Yanagitani, A.A. Kaminskii, “110 W ceramic Nd $^{3+}$:$Y_3Al_5O_{12}$ laser”, *Jpn. J. Appl. Phys.,* **2001** *40* 552.

[14]J. Marchal, J. Tyrone, R. Baranwal, T. Hinklin, R.M. Laine, “Yttrium Aluminum Garnet Nanopowders Produced by Liquid-Feed Flame Spray Pyrolysis (LF-FSP) of Metalloorganic Precursors”, *Mater. Chem. ,* **2004** *16* 822.

[15]J.M. Saniger, “Al-O infrared vibrational frequencies of gama-alumina”, *Mater. Lett.*, **1995** *22* 109.

[16]P. Tarte, “Infrared Spectra of Inorganic Aluminates and Characteristic Vibrational Frequencies”, *Spectr. Acta,* **1967** *23A* 2127.

[17] R.S. Hay, “Kinetics and Deformation during the Reaction of Yttrium-Aluminum Perovskite and Alumina to Yttrium-Aluminum Garnet”, *J. Am. Ceram. Soc.,* **1994** *77* 1473.

Chapter 5: Nano-α-Al_2O_3 by liquid-feed flame spray pyrolysis (LF-FSP)

5.1 Introduction

From a commercial perspective, there is considerable impetus to develop an economical source of sub-100 nm average particle size (APS) α-Al_2O_3 for applications ranging from tough prosthetic implants, to transparent armor, to transparent rather than translucent sodium vapor lamp envelopes, and possibly polycrystalline lasers, as well as for more common applications, nano/submicron-grained α-Al_2O_3 shapes offering significant advantages over micron-grained shapes[1-6] Despite this considerable potential, there are no commercial sources of sub-100 nm α-Al_2O_3, even though nano-alumina is easily produced in ton quantities.

Nano-alumina is produced using a variety of gas phase processes[7-11] and consist of transition aluminas, mainly of δ– with some γ– and θ-Al_2O_3. While transition aluminas do convert to the desired α phase, the high E_a for nucleating α-Al_2O_3 greatly impedes efforts to process dense α-Al_2O_3 with controlled grain sizes especially for submicron materials. Typically α-Al_2O_3 nucleation within t-aluminas is sporadic rather than uniform leading to exaggerated grain growth and vermicular microstructures without full densification.[7] As of yet there is no published technique for converting these easy to obtain t-aluminas into the α-alumina nanopowder required to manufacture fully dense sub-micron grained alumina monoliths.

Liquid-feed flame spray pyrolysis, has proven to be a cheap way of producing important quantities of t-aluminas.[10] The short time during which particles are exposed to high temperature, as well as the fast quenching, limits aggregation in the resulting powder. While the powders obtained from LF-FSP of metallo-organic precursors are transition alumina instead of the desired α phase, they are easily dispersed in various alcohols, which prompted us to modify the process to use a suspension of t-aluminas as precursor. High temperature in the flame should allow for nucleation of the alpha phase, while fast quenching and limited contact between particles in the flame should limit necking or particle growth.

This suspension-feed flame spray pyrolysis (SF-FSP) process allows the formation of dispersible α alumina nanopowder of 30-80 nm average particle size, with a conversion rate of 50-85%. This nanopowder exhibits some unusual properties, which initially were problematic in further processing of the powder. Nonetheless, fully dense α-alumina monoliths were obtained by presssureless sintering without sintering aids. Additional sintering studies were done to further investigate the sintering mechanisms in this new material.

5.2 Experimental

5.2.1 Precursors preparation

Precursors powders for the SF-FSP process consisted of three gas-phase synthesized nanopowders obtained from Degussa, Nanophase and home made by LF-FSP of alumatrane.[10] A different precursor was also made using Gibbsite. Each precursor consisted of 1-10 wt % nano t-alumina powders milled with alumina media in an ethanol/acetone solution (90/10 by volume) for 24 hours. After being left to decant for twelve hours, the suspension was ultrasonicated for 30 min with a 500 W titanium horn (Sonic, Newton, CT).

This dispersion is aerosolized with O_2 using techniques described in Chapter 3 and combusted at temperatures near 1600°C. Pumping rate was 70 mL/min and oxygen flow was 40 mL/min (pressure of 480 kPa) to form the aerosol. Production rate of the nanopowder was 100g/h.

5.2.2 Pellet preparation

Batches of 10 grams of SF-FSP powders obtained from Degussa or LF-FSP precursors were dispersed with Bis-(2-hydroxyethyl)-glycine (Bicine, 2 wt%) in 500 mL of ethanol/acetone solution (90/10 by volume) using a 500 W titanium horn (Sonic, Newton, CT) for 30 minutes. The suspension was then decanted for 24 hours and the upper portion was separated. The non-dispersible portion of the powder was below 10 wt% in all samples. Binders were added to the suspension (1 wt% PVA and 1 wt% 8000 MW PEG) and dispersed for another 30 minutes. The suspension was then dried for 48 hours at 80°C.

The resulting powder was hand ground in an alumina mortar and pestle and sieved through a polymer 400 mesh. Pellets were then uniaxially pressed (45 MPa) from 1 gram of powder each. After cold isostatic pressing at 200 MPa, the pellets had green densities of 53±2%. Binder burnout was done in controlled atmosphere furnace as described in chapter 3 (5°C/min/800°C/4 h/O_2). The resulting pellets were then annealed under vacuum at 1000°C (heating rate of 10°C/min, 2 hours dwell) to homogenize the pellet phase (as well as pore size). Pellets were then used for sintering studies using dilatometry as described in Chapter 3 and 5.

5.3 Results and discussion

From an academic perspective, there is considerable speculation in the literature as to why it is apparently impossible to make polycrystalline nano-α-Al_2O_3 monoliths let alone free flowing nanopowders of α-Al_2O_3.[12-16] Based on studies of high surface area polycrystalline t- and α-alumina, the literature suggests that it may be difficult to generate α-Al_2O_3 nuclei under conditions where complete conversion of t-aluminas to the alpha phase will occur without extensive grain growth. More problematic, the vermicular microstructures caused by this phase change inhibit any further densification of these materials. Studies by McHale et al suggest that polycrystalline nano-α-Al_2O_3 is not stable with respect to polycrystalline nano-γ-Al_2O_3 at surface areas of ≈ 125 m^2/g, equivalent to grain sizes of ≈ 8 nm.[16] One possible explanation is that hydrated, nanostructured polycrystalline γ-Al_2O_3 might be more stable than similarly hydrated α-Al_2O_3; however the McHale et al studies appear to rule this out.[16] It should be noted that a brief report by Krell et al describes the preparation of nano-α-Al_2O_3 by templating crystallization of amorphous aluminum-sec-butoxide and aluminun nitrate with diaspore.[17] This work highlights the difficulties in obtaining homogenous green bodies from nanopowders.

Our studies in chapter 5 as well as works described elsewhere[18-19] indicate that LF-FSP and SF-FSP, because they offer access to kinetic products have the potential to produce novel phases as well as expand known phase-fields. Conditions in the SF-FSP process could therefore allow α nucleation while keeping the powder dispersible and consisting of un-necked nanoparticles. The four powders synthesized by the SF-FSP process were analyzed as described below. Pellets were also made from SF-FSP powder derived from Degussa and LF-FSP nanopowder and used for sintering studies to investigate sintering mechanism of this new material.

5.3.1 SF-FSP powder characterization

Analysis of the SF-FSP powder had two goals: first to determine the actual phase composition of the powder (determined by XRD), but more importantly to determine that the powder particle size was still below 100 nm (BET, SEM, TEM, DLS). FTIR were also done to investigate hydroxyl groups on the surface of the powder.

5.3.1.1 X-ray powder diffraction patterns (XRD)

The precursors obtained from gas synthesis are mostly a mixture of the various δ phases and the γ phase (Table **5.1** and Figure **5.1**). The as-collected powders exhibit XRD patterns (Table **5.1** and Figure **5.2**) that indicate a high degree of conversion to mixtures of θ and α-Al_2O_3, with the gibbsite derived powders having the lowest conversions at roughly 50% and the LF-FSP, Nanophase and Degussa δ-Al_2O_3 nanopowders having conversions at 80-85%. The initial presence of θ and α-Al_2O_3 in the LF-FSP t-alumina explain the higher α content in this powder, the actual conversion rate seems similar between those three gas synthesis powders. Crystallites sizes increase between the gas synthesis precursor powders and the SF-FSP powders with a final size of 29-36 nm, this would indicates that each alpha crystallite is formed by several close neighbor particles in the flame. In the case of the gibbsite powder, the size decrease is due to two factors: first the 89% increase in density between gibbsite and $\alpha-$alumina and secondly to the removal of hydroxyl groups from the gibbsite structure to form $\alpha-$alumina.

To our knowledge there are no precedents for converting t-aluminas to dispersible sub 100 nm α-Al_2O_3 powders. Thus, the actual conversion mechanism here can only be conjecture. It may be that although hydration energetics are not an issue in determining the relative stability of polycrystalline, high surface area α- vs γ-Al_2O_3,[14] it is an issue here, in an environment where grain boundary interactions are nonexistent. This appears to be a reasonable argument given that the LF-FSP process generates enormous amounts of H_2O and CO_2, at high temperatures.

5.3.1.2 Scanning electron microscopy and transmission electron microscopy

Figure **5.3** shows a SEM of the SF-FSP powder, (the three gas synthesis precursor giving similar SF-FSP powders), showing the uniformity of the as-produced α-Al_2O_3 with no particles > 100 nm. The particles are faceted contrary to most particles formed by

LF-FSP (as seen in chapter 4), but this was observed before with the traces of alpha alumina in LF-FSP produced transition aluminas.[10] Figure **5.4** and **5.5** shows TEMs of groups of alpha particles after dispersion in EtOH and further drying. Those TEMs shows that the particles can be dispersed and are not necked. HRTEM and electron diffraction were done on a single 15 nm alpha particles as shown in Figure **5.6** and **5.7**, showing the facets more clearly as well as the hexagonal crystal structure.

5.3.1.3 Particle size analysis

To confirm the APS of the resulting nano-α-Al_2O_3, bicine dispersions of the SF-FSP powders were examined by dynamic laser light scattering (Figure **5.8**) giving APS of 30-40 nm. BET of the same powder gave similar results (with SSA of 40-60 m^2/g). This is in keeping with APS values obtained from XRD line broadening (Table **5.1**) and indicating that the powders are mostly single crystals.

5.3.1.4 Infrared spectroscopy

FTIR spectra of the Degussa alumina precursor powder before and after conversion is shown in Figures **5.9**. The spectra is characterized by broad νOH bands in the 3700 to 3500 cm^{-1} region which likely indicates an overlap of both physi- and chemisorbed species. Typically, isolated νOH bands for chemisorbed species appear at 3600-3700 cm^{-1} whereas bands for hydrogen-bonded OH groups appear lower, at 3400-3500 cm^{-1}. These are typical for most LF-FSP derived powders as discussed in Chapter 4. The degussa and nanophase alumina nanopowder shows similar broad peaks.

The SF-FSP α-Al_2O_3 nanopowder surprisingly does not exhibit those peaks, which would indicate that the surface of the powder is devoid of any chemisorbed or physisorbed water. This is highly unusual for powder obtained either from LF-FSP or SF-FSP process[18-19] and the fact that water presence in the flame should have an influence on α nucleation.

5.3.2 Sintering studies

Although the resulting α-Al_2O_3 nanopowders are not 100 % phase pure, the residual θ−Al_2O_3 is expected to convert without vermicular growth due to the high number of α-nuclei as shown in work with Taimicron powders.[21] One of the difficulties in processing the resulting powder is that, contrary to regular LF-FSP transition alumina (disperse spontaneously in water or EtOH)[10] surfactants are essential to dispersing these powders. This can be explained by the lack of hydroxyl groups on the surface of the powder linked to the surface being hydrophobic without the use of surfactants (as opposed to other LF-FSP nanopowder whose surfaces are generally hydrophilic). Bis-(2-hydroxyethyl)-glycine (Bicine) was most efficient (using 2 wt%),[20] allowing homogenous drying of the dispersions and further processing into green bodies.

5.3.2.1 Constant heating rate experiments

To determine optimum temperature conditions for sintering while keeping grain size as low as possible we heated a pellet of the SF-FSP powder under a constant heating rate (20˚C/min) in a dilatometer as described in Chapter two, as shown in Figure **5.10.** First stage of sintering (necks formation) seems to end around 1260°C and the third stage of sintering (pores removal) to start at 1550°C. There were no discernable differences between the two different kind of pellets (SF-FSP obtained from LF-FSP or Degussa precursor powder).

5.3.2.2 Controlled grain size

From those sintering curves experiments we were able to determine optimum sintering temperatures to limit grain growth while obtaining full density. Pellets were heated at 20°C/min to 1425°C, kept there for 1 h then step-cooled to 1350°C where they dwelled for 5 h, under vacuum. Figure **5.11** shows the SEM of a representative fractured surface (after thermal etching at 1250°C for two hours). Grain sizes are below 500 nm and the pellet is essentially dense (> 99% as determined by Archimedes measurements). The sintering temperature of 1350°C was chosen as it correspond to the second stage of sintering on the sintering curve, but still has limited sintering rates (high sintering rates during the second stage of sintering are indicative of faster grain growth.)[23] After using a hot isostatic press at 1400°C and 138 MPa (heating rate of 10°C/min), the pellet (2.8 mm thick, 9.5 mm diameter) is highly transluscent as can be seen in Figure **5.12**.

5.4 Conclusions

SF-FSP allows conversion of easily obtained transition alumina nanopowders into dispersible α-alumina nanopowders. This nanopowder can be used to form dense nano-grained ceramic monoliths, without using sintering aids. Preliminary results with hot isostatic pressing shows that these pellets can be sintered to transluscency.

As-received/as-processed powders				
PDF No. /Size	LF-FSP	Degussa	Gibbsite[†]	Nanophase
δ: 46-1131	32	63	0	0
δ*: 46-1215	48	6	0	0
δ^c: 01-77-3965	0	0	0	68
γ: 29-0063	8	31	0	32
α: 71-1124	5	0	0	0
S:70-2038	0	0	100	0
θ: 23-1009	7	0	0	0
Particle Size*	15 nm	11 nm	>100 nm	35 nm
After SF-FSP processing				
α : 71-1124	86	77	54	77
θ: 23-1009	14	23	46	23
Particle size*	29	36	88	36

*The average particle sizes reported here are based on Rietveld refinement but are consistent with BET determined particle sizes. The error is ±3%. [†]Spacerite (Gibbsite).

Table 5.1 Rietveld refinement phase composition of nano-Al_2O_3 before/after LF-FSP.

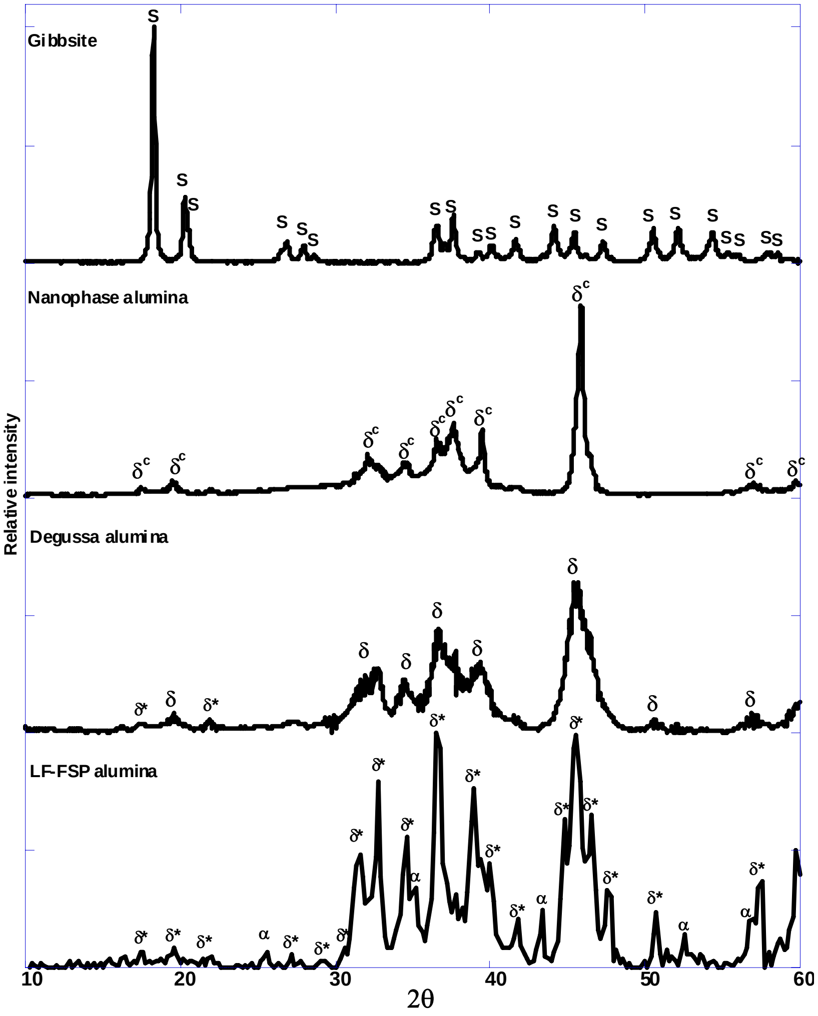

Figure 5.1 XRD of precursor transition alumina powders (S= PDF# 70-2038, δ^c=PDF# 01-77-3965, δ= PDF# 46-1131, δ*= PDF# 46-1215, α=71-1124).

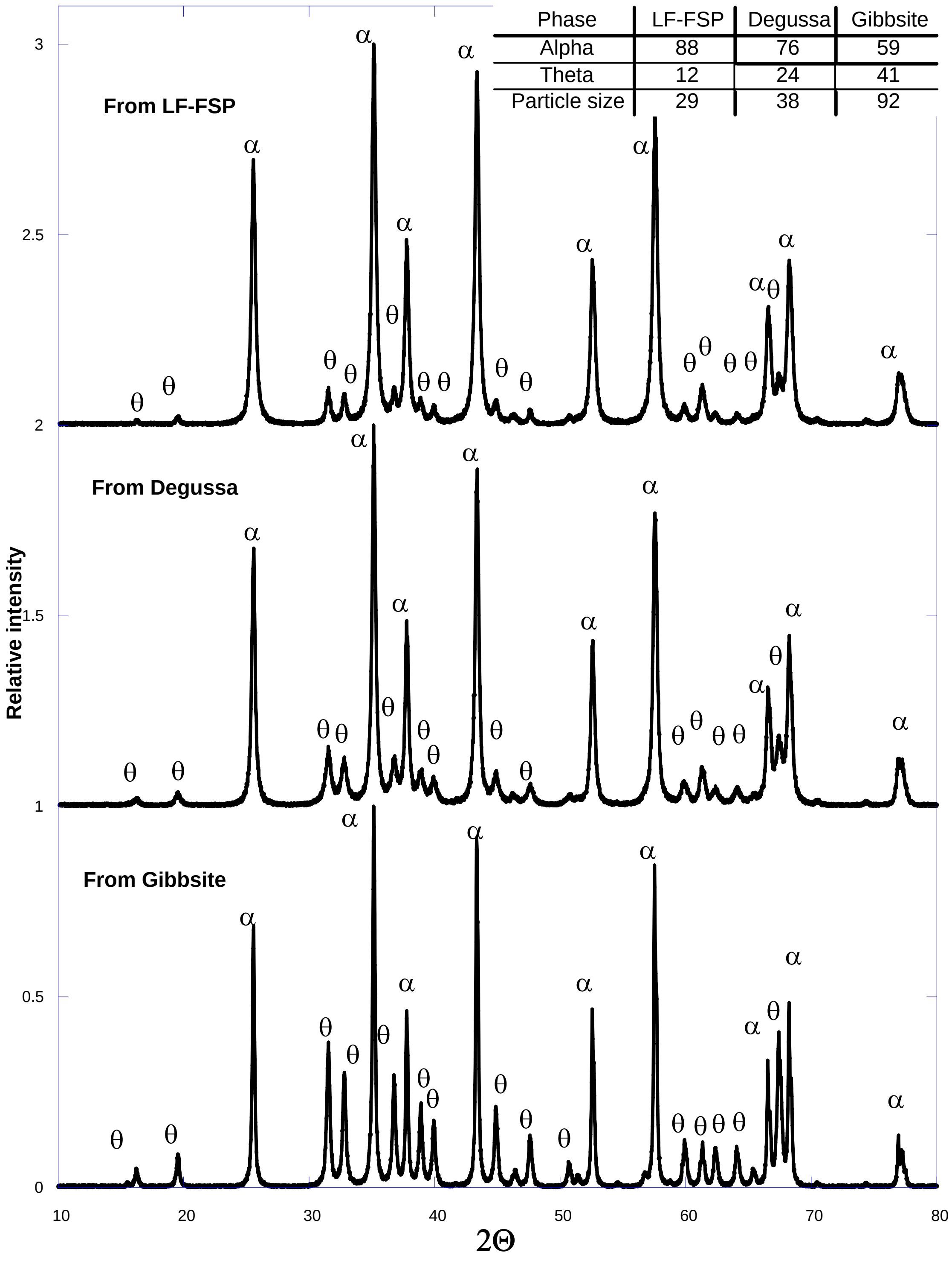

Phase	LF-FSP	Degussa	Gibbsite
Alpha	88	76	59
Theta	12	24	41
Particle size	29	38	92

Figure 5.2 XRD of SF-FSP powder (α = PDF 71-1124, θ = PDF 23-109).

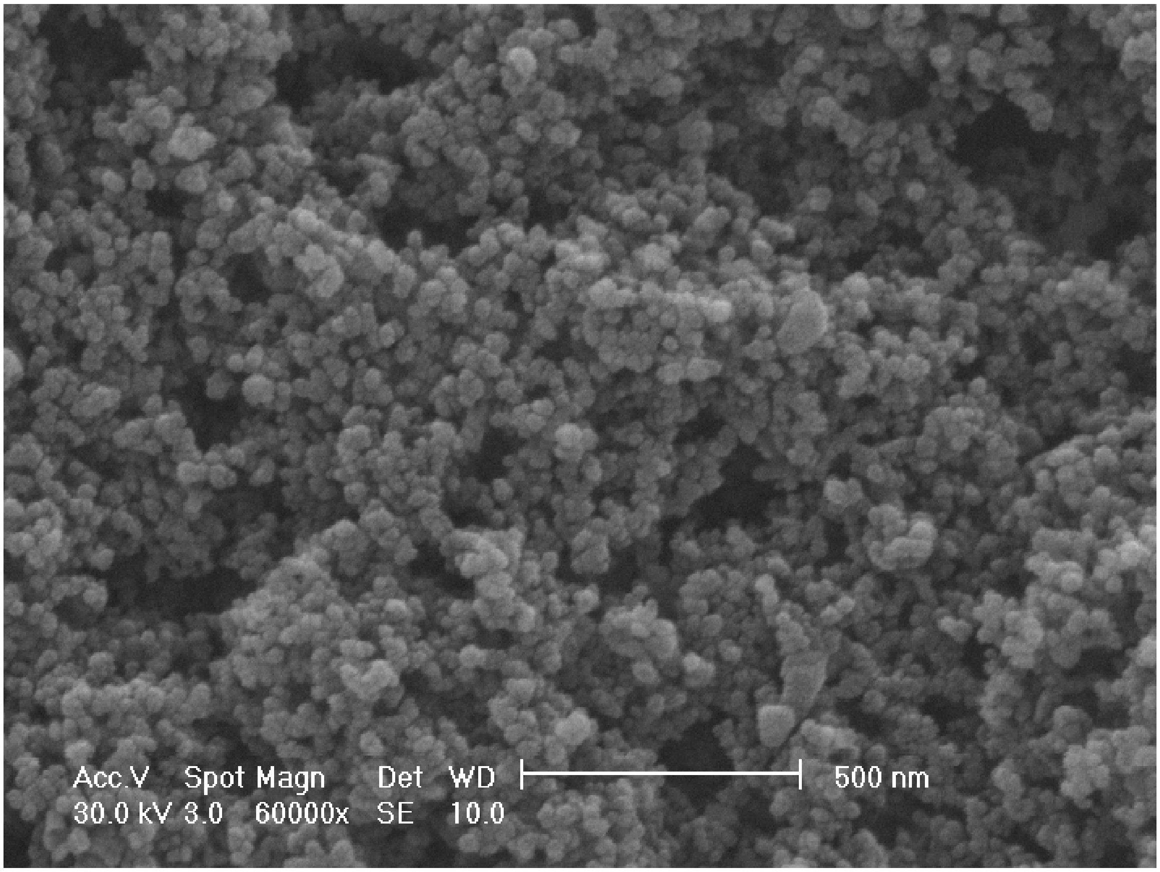

Figure 5.3 SEM of SF-FSP powder (86% α-Al_2O_3) obtained from LF-FSP t-Al_2O_3 precursor powder.

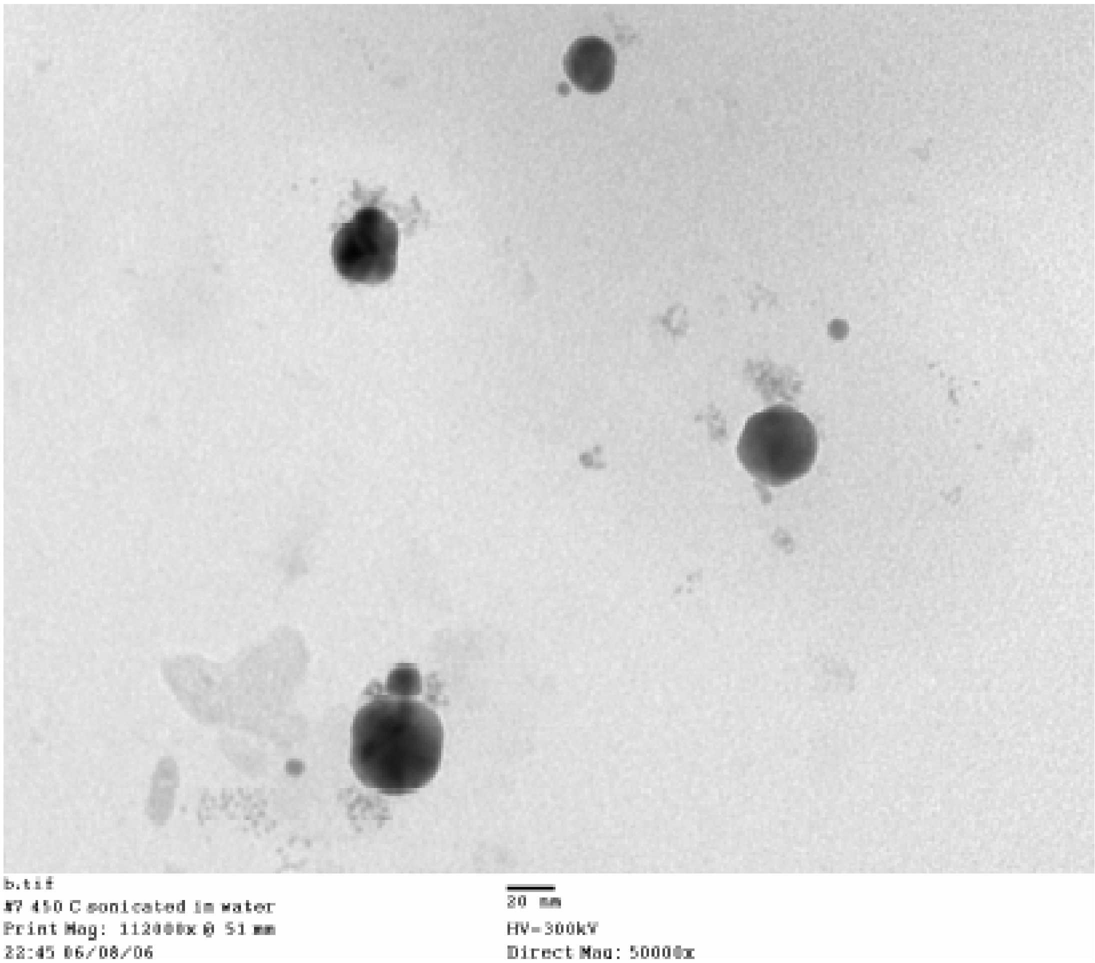

Figure 5.4 TEM of SF-FSP (86% α-Al_2O_3) powder obtained from LF-FSP t-Al_2O_3 precursor powder (Darvan-CN was used as dispersant)

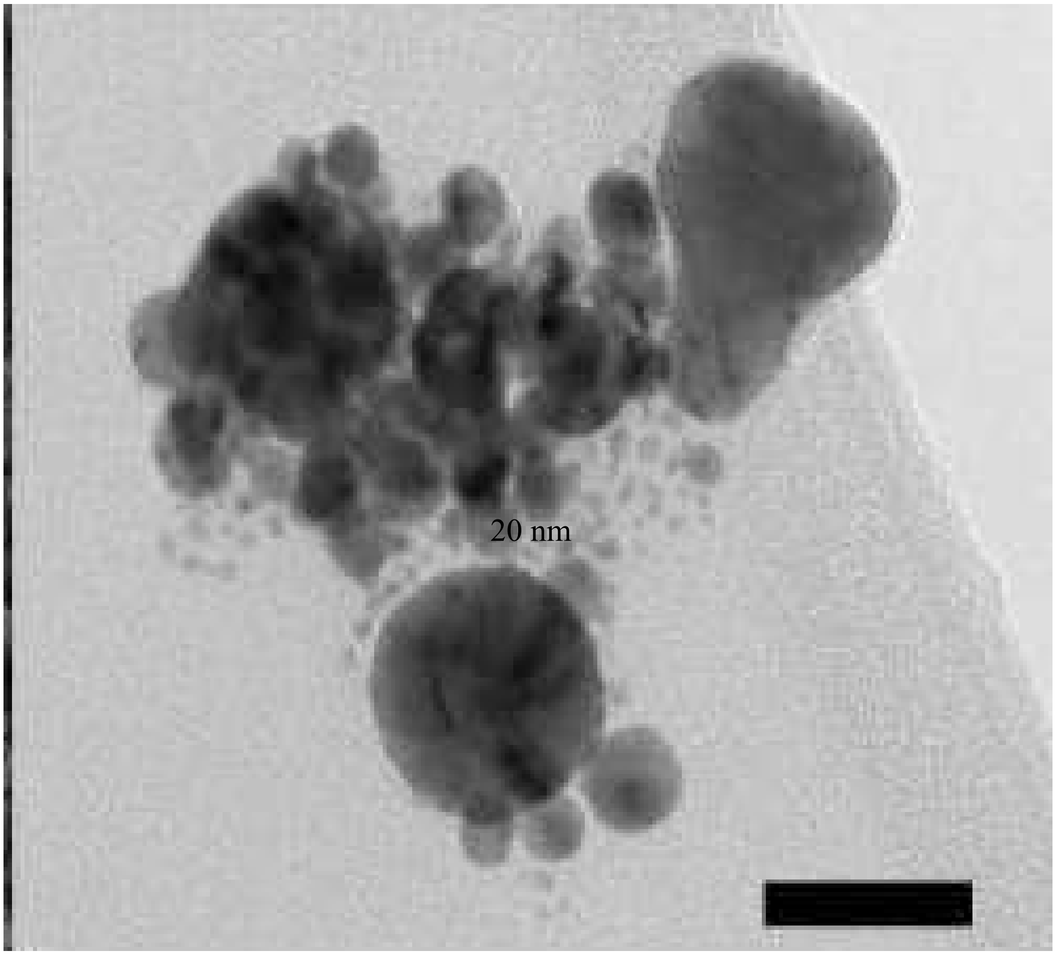

Figure 5.5 TEM of SF-FSP (86% α-Al_2O_3) powder obtained from LF-FSP t-Al_2O_3 precursor powder.

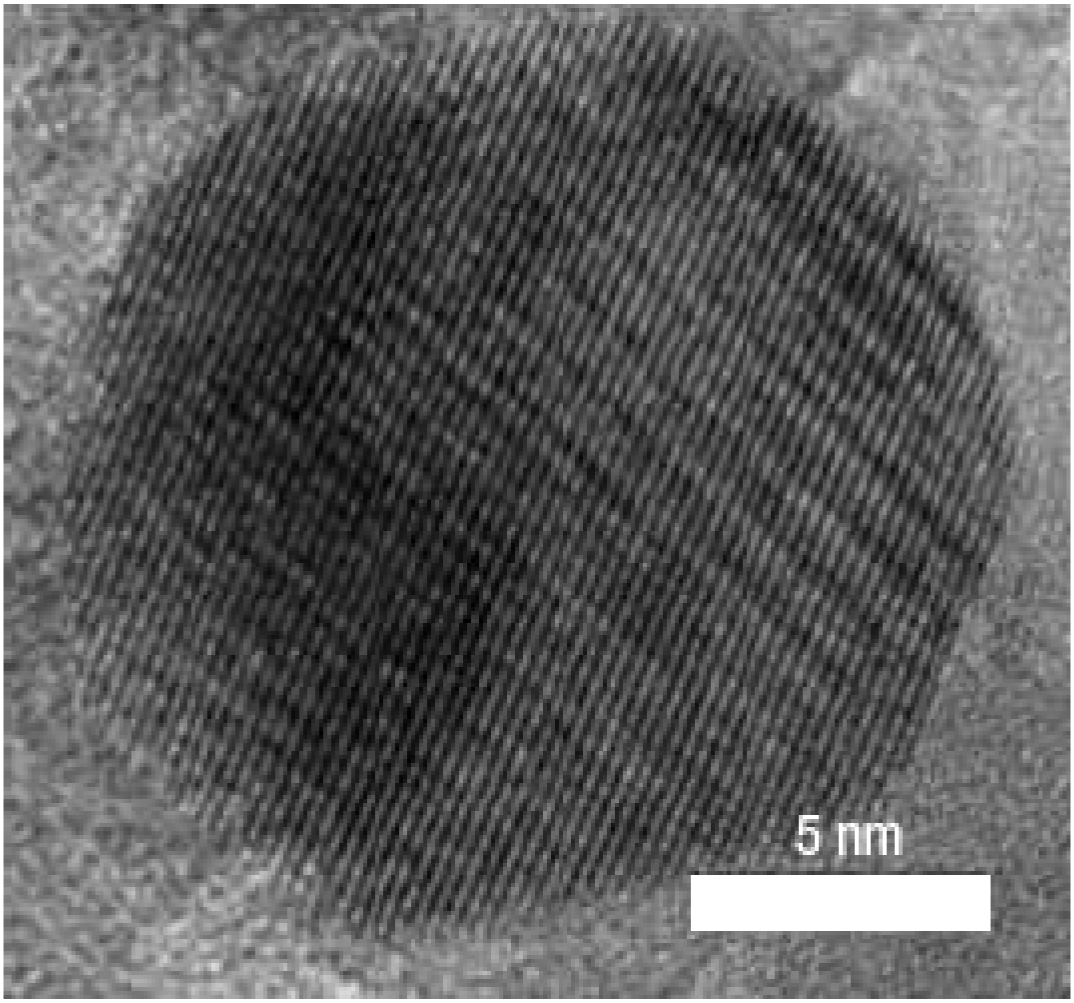

Figure 5.6 HRTEM of a single particle of SF-FSP α-Al_2O_3 powder obtained from LF-FSP t-Al_2O_3 precursor powder (Moire fringes can be observed at 45° from the lattice planes due to interference from other crystallographic planes).

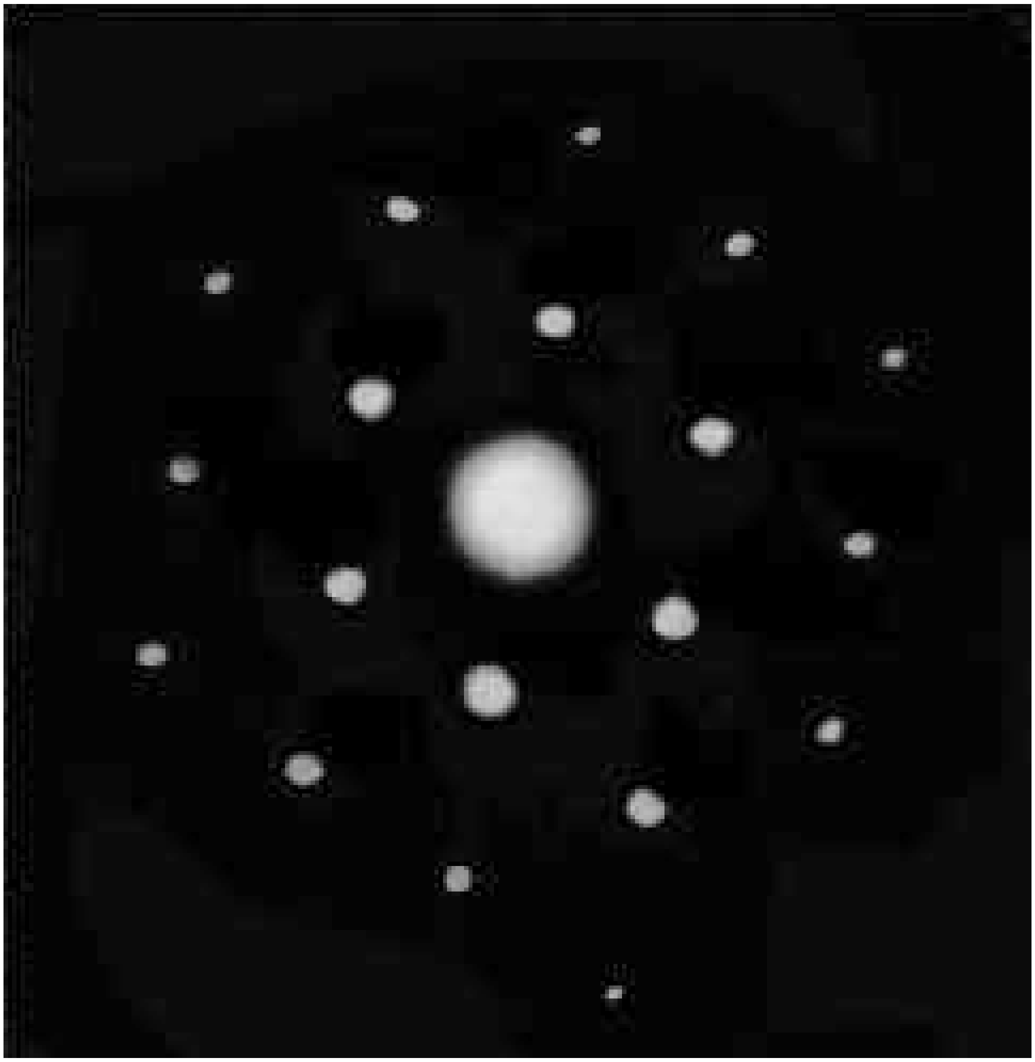

Figure 5.7. Electron diffraction of a single particle of SF-FSP α-Al_2O_3 powder obtained from LF-FSP t-Al_2O_3 precursor powder.

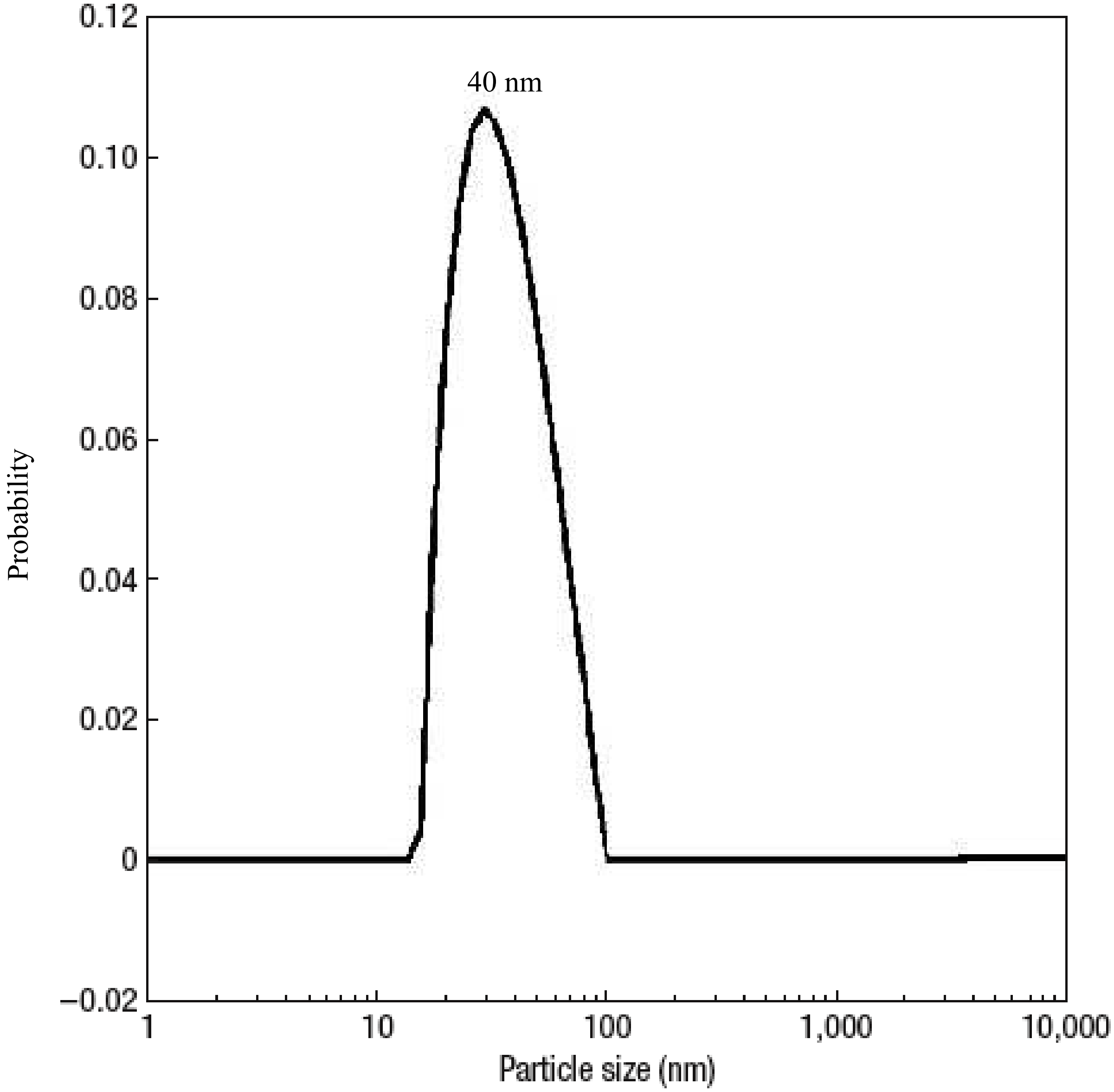

Figure 5.8 DLS of SF-FSP (86% α-Al_2O_3) powder obtained from LF-FSP t-Al_2O_3 precursor powder, indicating an average particle size of 35 nm, highest size probability of 40 nm.

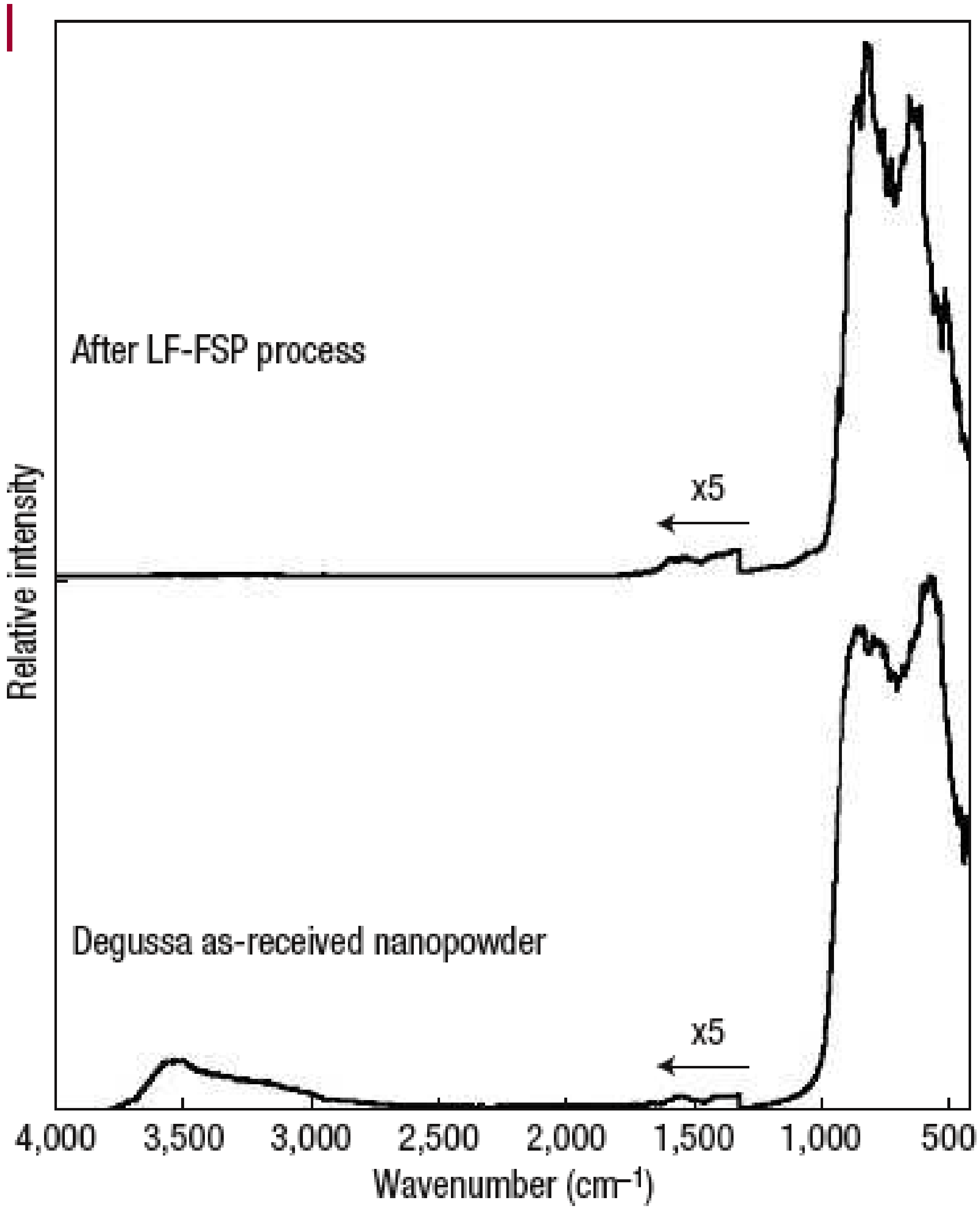

Figure 5.9 FTIR of Degussa precursor and SF-FSP powder derived from it.

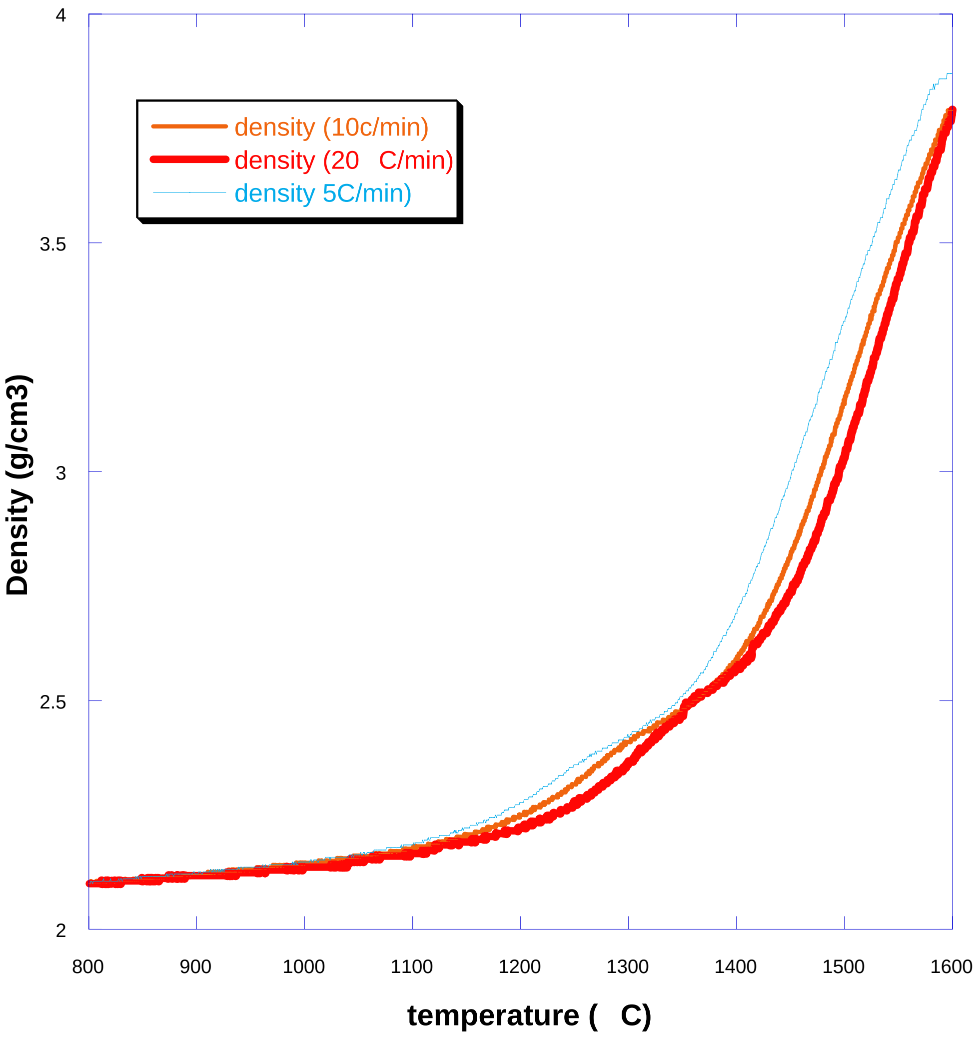

Figure 5.10 Sintering curve of α-Al_2O_3 pellets (after binder burnout at 800°C for 2 h) at constant heating rate (5, 10, 20°C/min).

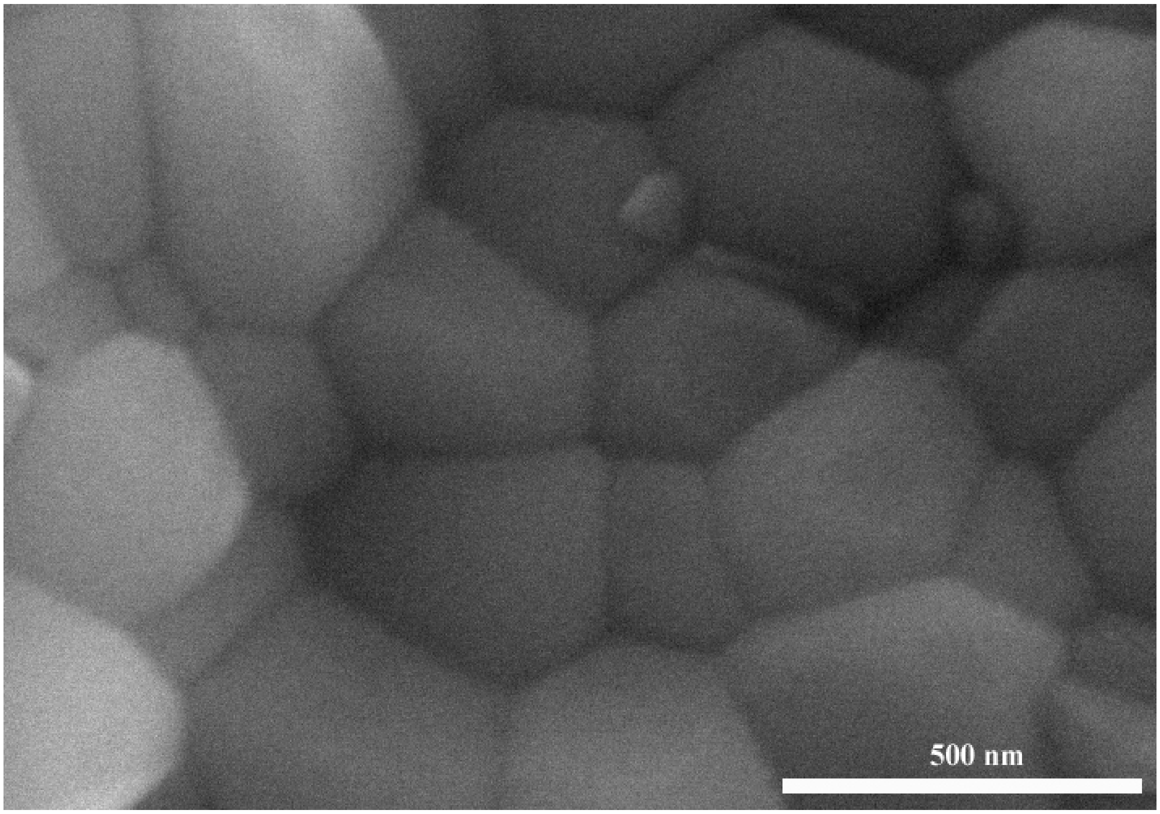

Figure 5.11 SEM of sintered pellet (sintered at 1425°C 1 h, then 1350°C, 5 h) fracture surface (after thermal etching).

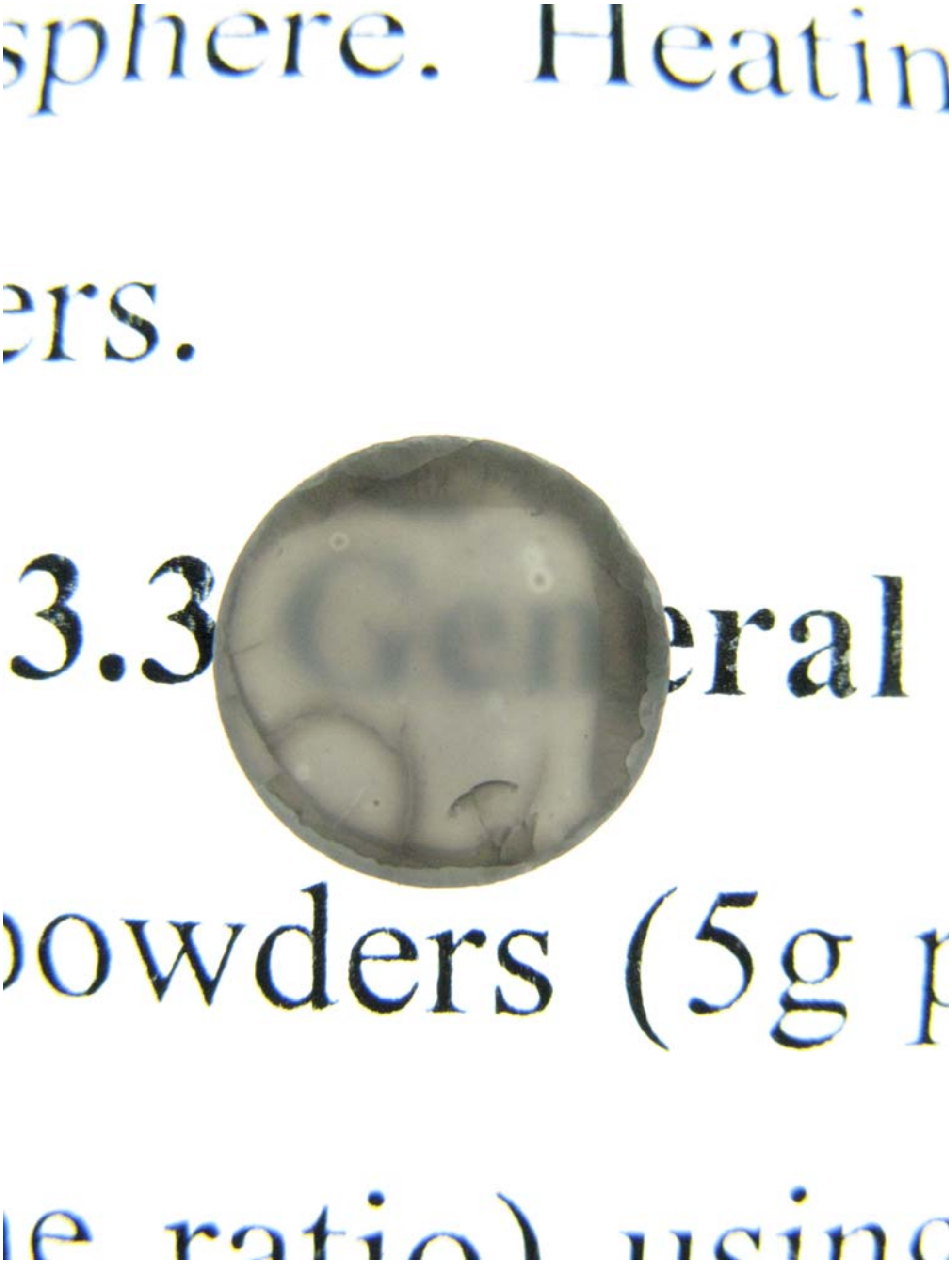

Figure 5.12 picture of α-Al_2O_3 pellet after Hipping (1400°C, 138 MPa), text under pellet is times new roman size 12, pellet is 2.8 mm thick and 9.5 mm diameter.

5.5 References

[1] W.A. Yarbrough, R. Roy, “Microstructural evolution in sintering of AlOOH gels”, *J. Mater. Res.*, **1987** 2 (4) 494.

[2] J. P. Parimal, G. Gilde, P. Dehmer, J. McCauley, “Transparent ceramics for armor and EM window applications”, *SPIE Proc.*, **2000** 4102 1.

[3] G. Fischman, “Validated Microstructural Assessment of Femoral Heads”, *J. ASTM Int.*, **2004** 1 1.

[4] V. Saikko, J. Keränen, “Wear simulation of alumina-on-alumina prosthetic hip joints using a multidirectional motion pin-on-disk device”, *J. Am. Ceram. Soc.*, **2002** 85 2785.

[5] J. D’Antonio, W. Capello, M. Manley, B. Bierbaum, “New experience with alumina-on-alumina ceramic bearings for total hip arthroplasty”, *J. Arthroplasty*, **2002** 17 390.

[6] A. Krell, P. Blank, H. Ma, T. Hutzler, M. Nebelung, “Processing of high-density submicrometer Al_2O_3 for new applications*”, J. Am. Ceram. Soc.*, **2003** 86 12.

[7] M.T. Swihart, “Vapor-phase synthesis of nanoparticles”, *Current. Opinion Col. Interface Sci.*, **2003** 8 127.

[8] A. Gutsch, M. Krämer, G. Michael, H. Mühlenweg, M. Pridöhl, G. Zimmermann, “Gas Phase Production of Nanoparticles”, *Kona,* **2002** 20 24.

[9] T. Hinklin, B. Toury, C. Gervais, F. Babonneau, J.J. Gislason, R.W. Morton, R.M. Laine “Liquid-Feed Flame Spray Pyrolytic Synthesis of Nanoalumina Powders”, *Chem. Mater.*, **2004** 16 (1) 21.

[10] G. P. Johnston, R. Muenchausen, S. Foltyn, D.M. Smith, W. Fahrenholtz, “Reactive laser ablation synthesis of nanosize alumina powder”, *J. Am. Ceram. Soc.,* **1992** 75 3293.

[11] R. Apetz, R.P. Brugen, “Transparent Alumina: A Light-Scattering Model”, *J. Am. Ceram. Soc.*, **2003** 86 (3) 480.

[12] R.B Bagwell, G.L Messing, P.R Howell, “The Formation of α-Al_2O_3 from θ-Al_2O_3: The relevance of a “critical size”, *J. Mater. Sci,.* **2001** 36 1833.

[13] H.L. Wen, F.S. Yen, “Growth characteristics of boehmite-derived ultrafine theta and alpha-alumina particles during phase transformation”, *J. Crystal Growth,* **2000** 208 696.

[14] J. Echeberria, J. Tarazona, J.Y. He, T. Butler, F Castro,”Sinter-HIP of α-alumina powders with sub-micron grain sizes”, *J. Europ. Ceram. Soc.,* **2002** 22 1801.

[15] J.M. Hale, A. Aurox, A.J. Perotta,, A. Navrotsky "Surface Energies and Thermodynamic Phase Stability in Nanocrystalline Aluminas", *Science*, **1997** 277 788.

[16] J.M. McHale, A Navrotsky, A.J. Perrotta, "Surface Energies and Thermodynamic Phase Stability in Nanocrystalline Aluminas"*J. Phys. Chem. B,* **1997** 101 603.

[17] M. Hongwei , A Krell, "Synthesis and processing of nano-alpha-Al_2O_3 powders", *Key Eng. Mater.,* **2002** 200 43.

[18] J. Azurdia, J. Marchal, R.M. Laine, "Synthesis and Characterization of Mixed-Metal Oxide Nanopowders Along the CoO_x–Al_2O_3 Tie Line Using Liquid-Feed Flame Spray Pyrolysis", *J. Am. Ceram. Soc.,* **2006** 8 (9) 2749.

[19] R.M., Laine, J., Marchal, H.P. Sun, X.P. Pan, "A new $Y_3Al_5O_{12}$ phase produced by liquid-feed flame spray pyrolysis (LF-FSP)", *Adv. Mater.*, **2005** 17 (7) 83020.

[20] R.A. Kimel, J.H. Adair, "Aqueous Synthesis at 200°C of Sub-10 Nanometer Yttria Tetragonally Stabilized Zirconia Using a Metal-Ligand Approach", *J. Am. Ceram. Soc,.* **2005** 88 (5) 1133.

[21] D. Godlinski, M. Kuntz, G. Grathwohl, "Transparent alumina with submicrometer grains by float packing and sintering ", *J Am Cer Soc* , **2002** 85 (10) 2449.

[22] I.W.P. Chen, J. Chen, "Sintering of Fine Oxide Powders: II, Sintering Mechanisms", *J. Am. Ceram. Soc*., **1997** 80 (3) 637.

Chapter 6: Future work

6.1 Discussion

In this work, liquid and suspension-feed flame spray pyrolysis (LF-FSP and SF-FSP) was used to demonstrate control of stoichiometry as well as the phases obtained in single and mixed metal oxide nanopowders. These processes allow the synthesis of YAG (garnet $Y_3Al_5O_{12}$), hexagonal $Y_3Al_5O_{12}$ and α-Al_2O_3 unagregated nanopowders. Nanograined translucent YAG and α-Al_2O_3 monoliths were obtained by pressureless sintering of these nanopowders. Investigation of hot isostatic pressing of YAG and α-Al_2O_3 to obtain ceramic monoliths with high transparency for optical applications, was limited due to technical difficulties, but early results with a custom- designed molybdenum furnace hot isostatic press showed promising results as detailed in Chapter 5.

Initial work has been done on doping YAG and α-Al_2O_3 with transition metal (Cr, Fe, Ti) as well as rare earth (Nd, Yb, Pr, Yb, Eu) or other dopants (Si). Sintering these nanopowders into transparent monoliths, using our new HIP apparatus would allow development of new polycrystalline laser hosts.[2,3] Figure 6.1 shows early work on doped YAG monoliths. Further investigation is required to determine the differences in sintering behavior in these doped materials as well the dopants solubility in these nano-materials.

The SF-FSP technique developed in this work, was used by other members of the group to form core shell nanopowders in the ceria-zirconia-alumina system.[4] Further investigation of core shell nanopowders could involve coating α-Al_2O_3 with sintering aids (MgO, Cr_2O_3) to potentially decrease sintering temperatures and therefore obtain transparent α-Al_2O_3 monoliths with even smaller grain size (and higher in-line transmission of light). Investigation of dopants surface or bulk location in the nanopowders, by comparing luminescence results between doped YAG obtained by one-step LF-FSP (homogeneous distribution of dopants in the particle) or two step SF-FSP (dopants located at surface of particle) could show the potential for tailored phosphors.

FS-FSP could also be used to react nanopowders with metalloorganic precursor to potentially change the phase obtained in multi-metallic oxide nanopowders. For example, α-Al_2O_3 nanopowders could be reacted with yttrium propionate precursors in SF-FSP to obtain YAG nanopowders.

Further work should examine the conversion of doped (Cr, Mg, Fe, Ce) transition alumina nanopowders to doped α-Al_2O_3 by SF-FSP and possible changes in sintering behavior. Studies have already been made on Cr-doped transition alumina[5] and those early results prompted the development of the SF-FSP techniques described in chapter 5. Pressureless sintering and/or HIPing of these nanopowders would provide a new route to manufacture polycrystalline lasers.

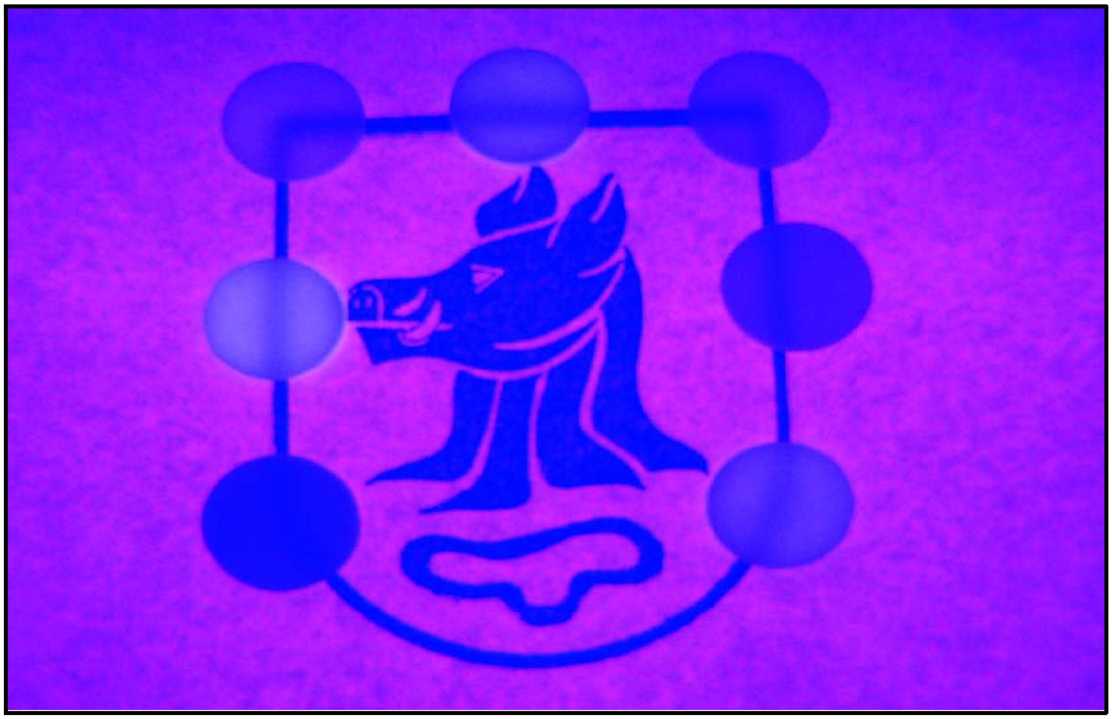

Figure 6.1 Photograph of doped and undoped YAG monoliths (each pellet is 2.5-3 mm thick and 11-13mm diameter). From Top left corner, clockwise: 1 mol% Ni:YAG, YAG, 0.1mol% Si:YAG, 0.5mol% YAG, YAG, 2 mol% Ni:YAG.

6.2 References

[1] M. Heyrman, C. Chatillon, "Thermodynamics of the Al–C–O Ternary System", *J. Electrochem. Soc.*, **2006** 153, E119.

[2] E.A. Khazanov, M. Sergeev, "Concept study of a 100-PW femtosecond laser based on laser ceramics doped with chromium ions", *Laser Phys*, **2007** 17 (12) 1398.

[3] Y. Wu, J. Li, Y. Pan, J, Guo, B. Jiang, "**Diode-Pumped Yb:YAG Ceramic Laser**", *J. Am. Cer. Soc.* **2007** 90 (10) 3334.

[4] M. Kim, R. Laine, "Combinatorial processing of mixed-metal oxide nanopowders along the ZrO2-Al2O3 tie line using LF-FSP", *J. Cer. Proc. Res.*, **2007** 8 129.

[5] R.M. Laine, J. Marchal, J. Azurdia, R, Rennensund, "LF-FSP Modification of nanoparticles", US patent application 20060087062 (**2006**).